

**DISSOLUTION AND THERMAL SPALLATION OF BARRE
GRANITE USING PURE AND CHEMICALLY ENHANCED
HYDROTHERMAL JETS**

A Thesis

Presented to the Faculty of the Graduate School
of Cornell University

In Partial Fulfillment of the Requirements for the Degree of
Master of Science

by

Ivan Beentjes

May 2018

© 2018 Ivan Beentjes

ABSTRACT

The primary aim of this study was to investigate the use of hydrothermal jets as a means of drilling rock. Specifically, an electrically heated hydrothermal jet was impinged on the surface of cylindrical Barre Granite samples (basement rock) contained in an autoclave reactor to induce thermal spallation. Comminution of the rock surfaces was achieved at supercritical water conditions, temperatures from 535-580°C and pressures of 22.5-27MPa. These conditions simulate those encountered in drilling deep, water-filled wells. Preferential removal of quartz grains from the rock matrix was observed. However, experimentally determined heat flux and surface temperature measurements indicated that hydrothermal comminution occurred below the empirically determined minimums for the onset of continuous thermal spallation for low-density flame jet drilling.

Chemically enhanced hydrothermal spallation drilling experiments introduced sodium hydroxide into the hydrothermal jet, at the same supercritical conditions. The combination of accelerated mineral dissolution due to the presence of hydroxide ions, high temperature kinetics, and thermal stress induced significant rates of rock removal. Comparison with empirical quartz dissolution data indicated this drilling success was primarily due to chemical dissolution, enabling the quantitative modeling of an effective drilling rate.

BIOGRAPHICAL SKETCH

Ivan Beentjes enrolled in Durham Continuing Education on July 5th, 2010 and completed his secondary school education on July 11th, 2011. He received his Ontario Secondary School Diploma, and the Ontario Power Generation Student Achievement Award on October 5th, 2011, graduating with a 12th grade average of 95%.

On September 12th, 2011, Ivan began his Bachelors of Applied Science at the University of Waterloo. He received his undergraduate degree in Mechanical Engineering (Co-operative Program) with a Management Science Option on June 17th, 2017, graduating With Distinction, and Dean's Honours List. During his undergraduate studies he also received Dean's Honours List for Winter 2013, Fall 2015, and Spring 2016. His scholarships include: ASHRAE's Ruben Trane Scholarship (2015, 2016), Suncor Energy Emerging Leaders Award (2011-2016), and President's Scholarship of Distinction (November 2011).

Ivan began his Master's of Science at Cornell University under the supervision of Croll Professor Jefferson W. Tester on May 31st, 2017. He graduated with an MS degree in Chemical and Biomolecular Engineering on May 27th, 2018.

To my nieces and nephews

Brian, Nicole, Jolie, Michelle, and Derek

May your excitement for learning and science grow

-and one day put this thesis to shame

ACKNOWLEDGEMENTS

“Whether I shall turn out to be the hero of my own life, or whether that station will be held by anybody else, these pages must show.” (Dickens, 1850). The following pages show that there are many heroes to whom I owe a debt of gratitude. They are the people who helped me in my journey through Cornell’s Chemical and Biomolecular Engineering program, and without whom this thesis would not have been possible.

Firstly, I would like to begin by thanking my advisor Professor Jefferson W. Tester, whose boundless curiosity, energy, determination, and generosity were the template upon which this research was shaped.

Many thanks to Professor Larry M. Cathles III for assisting me in all things geology, and for serving on my advisory committee. To Glenn Swan, Polly Marion, and Bailey Colvin for their practical assistance in the myriad of details that go into a successful project.

To my fellow graduate students in the Tester Research Group who made themselves available to discuss research problems: Sean Hillson for his knowledge and technical expertise in hydrothermal systems. Jay T. Bender for assisting in the experimental work. Adam Hawkins: project touchstone, geologist, and friend. Arna Palsdottir, David Zurmuhl, Gloria Andrea Aguirre, and Laura Sinclair who provided me assistance and support at every turn.

This thesis would not have been possible without the initial creative work of Robert Potter on spallation drilling. I am also grateful to Jared Potter for his interest in this research and for donating a high-pressure experimental apparatus. Many thanks to Chad Augustine for his initial work at MIT experimentally demonstrating that hydrothermal flames could be produced in supercritical water and used to spall rock, and to Rick M. Rauenzahn and Mark Wilkinson for their pioneering efforts in characterizing and modeling flame jet and laser induced spallation and finally to W. Gabe Worley for his excellent work on quartz dissolution kinetics in hydrothermal NaOH solutions.

To my Sisters, the Kelly family, and Elaine Stirling for their unwavering support.

You are legend.

TABLE OF CONTENTS

Abstract	i
Biographical Sketch	iii
Acknowledgements	v
List of Figures	x
List of Tables	xv
List of Abbreviations	xvi
List of Symbols	xvii
Chapter 1. Motivation and Background	1
1.1. Motivation	1
1.2. Background	2
1.2.1. Direct Use of Geothermal Heat	2
1.2.2. Geothermal Heat Pumps	3
1.2.3. Electrical Power Generation	5
1.3. Engineered Geothermal Systems	8
1.4. Conventional Rotary Drilling	12
Chapter 2. Objectives and Approach	18
2.1. Objective and Approach to Project Execution	18
2.2. Summary of Project Execution	19
Chapter 3. Review of Previous Thermal Spallation Drilling Research	21
3.1. Early Spallation Testing	24
3.2. Open Flame Thermal Spallation	24
3.3. Hydrothermal Flame Spallation	27
3.4. Hydrothermal Jet Spallation	28
Chapter 4. Experimental Apparatus and Procedures	30
4.1. Description of Experimental Apparatus	30
4.2. Measurement Uncertainty	39

Chapter 5. Pure Water Hydrothermal Spallation Results	41
5.1. Quantifying Experimental Results	41
5.1.1. Preferential Comminution of Quartz	42
5.2. Comminution Mechanisms	46
5.2.1. Erosion of Quartz	46
5.2.2. Dissolution of Quartz	48
5.2.3. Microspallation of Quartz	51
5.2.3.1. Surface Temperature Measurements	53
5.2.3.2. Heat Flux Experiments	57
5.2.3.3. Comparison of Heat Flux Data to Correlations	62
5.3. Comparison of Hydrothermal to Flame and Laser Spallation	68
Chapter 6. Chemically Enhanced Hydrothermal Spallation Literature Review	70
6.1. An Early Historical Experiment	70
6.1. Recent Work	73
Chapter 7. Chemically Enhanced Hydrothermal Spallation Experiments	76
7.1. Modifications to Experimental Apparatus and Conditions	76
7.2. Experimental Results	82
7.2.1. Initial Experiments	82
7.2.2. Time Dependence	87
7.3. Modelling Drilling Rate	89
7.4. Determining Chemical Dissolution Constant	96
Chapter 8. Conclusion and Recommendations for Future Work	104
8.1. Conclusion	104
8.2. Future Work	106
Appendix A	108
Appendix A-1 Instrument Error Analysis	108
Appendix A-2 External Jet Temperature Correlation	113

Appendix B	114
Appendix B-1 Pure Water Spallation Test Data	115
Appendix B-2 Chemical Enhanced Hydrothermal Spallation Test Data	122
References	126

LIST OF FIGURES

Figure 1. Comparison between three main methods of geothermal electric power generation (Holm, 2012). These numbers are only approximate and will vary widely depending on the dissolved CO ₂ contained in the fluid (steam and effluent) produced from a hydrothermal resource.	6
Figure 2. Comparison between oil, coal, natural gas, and geothermal for CO ₂ emissions for U.S. electrical power generation (EPA, 2017).....	7
Figure 3. Ground temperature map of the continental U.S. The majority of the U.S. has ground temperatures greater than 125°C at a depth of 5.5 km. (Blackwell, 2011)	10
Figure 4. Visual representation of EGS.....	11
Figure 5. Schematic of a conventional rotary drilling rig (Freudenrich & Strickland, 2001).....	14
Figure 6. Worn rotary well drilling bits ~834" dia.	15
Figure 7. Evolution of conventional rotary drill bits. (Superior Drilling Products, 2014).....	16
Figure 8. Geothermal well costs (in black) compared to average 2009 oil and gas well costs (in red) (Lukawski, et al., 2014)	17
Figure 9. The thermal spallation process. A) Heat applied to the rock induces thermal stress which combines with residual stress and imperfections to create small fractures. B) Stress concentrations cause these fractures combine into significant cracks. C) The increased heating results in spalls being ejected from the rock surface while new fractures are formed.....	22
Figure 10. A) A sufficiently high temperature fluid impinging on a granitic rock surface induces a large thermal gradient in the rock resulting in rock removal by spallation (drilling). B) Experimental apparatus arrangement of 2.54cm diameter Barre Granite rock sample. C) The reactor chamber containing the rock sample and cooling water can be moved vertically upwards into the hydrothermal jet to increase thermal shock of the impinging fluid. The movement of the reactor chamber is bi-directional along the centerline allowing the rock sample to retract from the hydrothermal jet, halting the experiment at a select time interval	32
Figure 11. System piping and instrumentation diagram.....	33

Figure 12. High temperature and pressure spallation apparatus. A) Main reactor and heaters. B) Hot water and chemical injection pumps. C) Cooling water pump, and back pressure system.....	34
Figure 13. A) High pressure heat exchanger for preheating super critical jet, and the profile of the internal baffles. B) Additional high temperature water heater. C) Hydraulic piston for raising the granite rock sample into position. D) Cooling water flow pattern to prevent gradual thermal expansion of the rock sample; red straws indicate the flow path for hot effluent exiting the comminution chamber.....	36
Figure 14. Three types of tests performed. Comminution Test, is the experimental arrangement of a spallation test, with and without chemical enhancement. Surface Temperature Test, records the rock temperature just below the sample's surface. Heat Flux Test measures energy flux during an experiment	38
Figure 15: Range of uncertainty for energy calculations based on the impinging jet temperature.....	40
Figure 16. Before and after a spallation experiment. The largest spalls ~3mm across and 0.3-0.5mm deep. Striations on the before sample are saw marks.....	41
Figure 17. Spallation experiments with their associated pressures, temperatures, and time durations. Data in Table 3, see Appendix B-1.....	42
Figure 18. An o-ring separates the area exposed to supercritical water (in the centre of the granite samples's top surface) from the cooling water that surrounds the sample. The SEM images can be seen overlaid on the area of interest.....	43
Figure 19. LSCM test acting as a profilometer to determine the subducted areas.....	44
Figure 20. The SEM silicon element (Si) scan of the unspalled rock sample's surface which highlights the silica rich quartz zones, compared against the LSCM scan of the same sample's post-communition test surface. The colour-corrected 'black' quartz crystals in the SEM image and the 'black' subducted areas in the LSCM comminuted image correspond to each other. Observation indicates that quartz crystals are preferentially removed.....	44
Figure 21. The range of jet nozzle velocity, and pressure difference between the jet nozzle and rock surface. The range of property values are bounded by the systems minimum and maximum experimental pressures.....	47
Figure 22. A close-up of a comminuted area, showing acute edges.	47
Figure 23. Calculated dissolution rate for four PWHS tests plotted against the empirical dissolution equation with 95% confidence intervals.....	49

Figure 24. Arrhenius plot of pure quartz dissolution data including this study's comminution experiments (Worley, 1994). Data in Table 4, see Appendix B-1.....	50
Figure 25. The distance between the two thermocouples measuring jet and surface temperature was 1.8mm. Backlighting the rock sample shows the transparency of the 0.65 mm thick granite "cap".....	55
Figure 26. Estimated temperature difference, ΔT , between the surface of the rock and the hydrothermal jet as a function of the hydrothermal jet temperature at 24 MPa. The data points represent steady state temperature measurements. The dashed trendline is a best fit regression of the data, and the two linear trendlines are regression analyses that intersect at the supercritical point. Data in Table 5, see Appendix B-1.	56
Figure 27. Experimental configuration for the heat flux tests. To mitigate edge effects the ratio of A:B was 5:1, D:A 5:1, C:D 19:1.....	59
Figure 28. ΔT correlation lowered by 20°C, increasing the rock surface temperature by 20°C. Reasons: slope change of the Nusselt number is minor, water density is high, and the Reynolds number low in the <100°C region.	60
Figure 29. Heat flux as a function of experimentally determined rock surface temperature. The ratios of supercritical jet flow to the cooling water flow rates of 1.8, 2.8 and 3.8 liters per minute, LPM, were 1:7.5, 1:11.5, 1:15.8, respectively. The volumetric specific heat of water, and thermal conductivity of granite at a pressure at 24 MPa were calculated using the experimentally determined rock surface temperature. Data in Table 6, see Appendix B-1.	62
Figure 30. Reynolds and Prandtl numbers for the range of experimental temperatures and pressures, assuming pure water properties.	64
Figure 31. Comparison of experimental heat flux results to published heat flux correlations for impinging jets.....	67
Figure 32. Experimentally determined heat flux and surface temperature for hydrothermal jet spallation compared to flame jet and laser spallation. This study's hydrothermal experiments were conducted at surface temperatures below previous experimentally determined thresholds for gas immersed spallation. Data can be found in Table 7, see Appendix B-1.	69
Figure 33. Conceptual diagram of the McCoulough chemical drill (Ledgerwood, 1960).....	71
Figure 34. Diagram of the BJ Services Company acid drilling operation. Fig 1. "Example assembly", Fig 3. "Swirl inducer... can result in conical jet", Fig 5. "Many individual nozzles can be used to cover entire borehole". (Rae, et al., 2004)	73

Figure 35. "...an enlarged schematic representation, partly cross-sectional, of a second embodiment of a hydrothermal drilling system that uses chemical reaction to produce hot drilling fluid in a borehole." (Polizzotti, 2004).....	74
Figure 36. Thermocouple moved from inside the hydrothermal jet nozzle to outside. It was replaced inside the tube by a 1.59mm (1/16") tube to deliver NaOH.....	78
Figure 37. Temperature correlation tests made at increasing temperatures to quantify the ΔT between the heater, internal jet, external jet and surface temperatures. The measured error associated with the external jet temperature measurements was $\sim\pm 2\%$ full scale.....	78
Figure 38. A) An extensively eroded O-ring that did not fail. B) A failed O-ring with a clear fluid channel. C) External jet thermocouple temperature profile from a failed O-ring CEHS experiment, showing both the high and low temperature regions.	81
Figure 39. CEHS results. Side cut Barre Granite samples show significant dissolution and spallation. These experiments used 0.29-1.38% w/w NaOH (0.0725-0.345 molality), at 24.5 ± 1 MPa, $400\pm 10^\circ\text{C}$ rock surface temperature, for 10 minutes.	83
Figure 40. The mass of granite removed and the depth drilled increases with increasing NaOH molality. Once the process initiates the ratio of granite removed to NaOH injected stabilizes with increasing solvent molality. All experiments ran for 10 minutes. Data in Table 8, see Appendix B-2.....	84
Figure 41. Predominantly pebble shaped quartz spalls ranging in size. The clear spalls are quartz, dark grey and black are micas, and red color is surface staining from the high temperature silicone O-ring. No feldspar is visible.....	85
Figure 42. Preferential weakening along crystal boundaries due to the absence of feldspar.	86
Figure 43. Reformed minerals on the side walls of the area hollowed out by CEHS. .	87
Figure 44. Increased mixing of fresh NaOH solution with the discharge fluid as the penetration depth increases with time.	88
Figure 45. Granite removed during CEHS experiments for different exposure times indicate that rock removal is linear dependant on exposure time. Data in Table 8, see Appendix B-2.	89
Figure 46. <i>A surface</i> is the hemispherical spallation front at the base of the borehole not including the cylindrical side wall.....	94
Figure 47. Increasing mass of rock removal at increasing molality, and temperature.	97

Figure 48. CEHS data plotted as <i>logkforward</i> , <i>logmOH</i> –, and includes the <i>b'</i> found by regression analysis. The yellow data points are corrected data due to failed O-ring seals during the experiment.....	98
Figure 49. <i>k(T)OH</i> – on an Arrhenius plot. The data with a surface temperature of ~385°C close to the water critical point transition of ~382°C (24.5MPa) did not agree as well to a linear regression fit as those data farther away. Data in Table 10, see Appendix B-2.	99
Figure 50. Regression analysis of this study and Worley's NaOH dissolution of quartz data. The yellow data points are corrected data due to failed O-ring seals during the experiment. Data in Table 10, see Appendix B-2.	100
Figure 51. <i>k(T)OH</i> – on an Arrhenius plot. Linearity of the trendline illustrates temperature dependence of chemical dissolution over six orders of magnitude. Data in Table 10, see Appendix B-2.	102
Figure 52. Comparison of CEHS to flame, laser, and PWHS drilling.	103
Figure 53. Combined heat flux and surface temperature experimental configuration, designed to directly compare heat flux to rock surface temperature and estimate the average heat transfer coefficient.....	107
Figure 54. Temperature difference correlation between the externally mounted thermocouple and rock surface temperature.....	113

LIST OF TABLES

Table 1: Properties of Barre Granite (Chayes, 1950) (Robertson, 1988)	45
Table 2. Uncertainty, δ , associated with the measurements and equation of state properties.....	112
Table 3. Pure water hydrothermal spallation data from Figure 17.....	114
Table 4. Chemical dissolution of quartz in pure water data from Figure 24.....	115
Table 5. Pure water hydrothermal spallation rock surface and jet temperature data from Figure 26.....	118
Table 6. Pure water heat flux data from Figure 29.....	119
Table 7. Mechanical, flame, laser, pure water hydrothermal spallation data comparison from Figure 32.....	120
Table 8. Rock removal and time dependence data from Figure 45.....	122
Table 9. CEHS rock removal, penetration depth, and pH data for 10 minute tests from Figure 40, and Figure 48.	123
Table 10. Complete chemical dissolution data table from Figure 49, and Figure 50.	124

LIST OF ABBREVIATIONS

COP	Coefficient Of Performance
CEHS	Chemically Enhanced Hydrothermal Spallation
EGS	Engineered or Enhanced Geothermal Systems
IR	Infrared
LSCM	Laser Scanning Confocal Microscope
PWHS	Pure Water Hydrothermal Spallation
SEM	Scanning Electron Microscope

LIST OF SYMBOLS

A	Area
$A_{surface}$	Active, effective surface area
D	Diameter
E	Young's modulus
h	Enthalpy
\bar{h}	Average convective heat transfer coefficient
Δh	Change in enthalpy
k	Thermal conductivity
$k_{forward}$	Chemical dissolution rate constant, forward reaction
$k_{reverse}$	Chemical dissolution rate constant, reverse reaction
l_o	Initial length
Δl	Change in length
m	Molality
\dot{m}	Mass flow rate
M_{solute}	Mass of solute
$M_{solvent}$	Mass of solvent
M_{water}	Mass of water
\overline{Nu}	Average Nusselt number
P	Pressure
Pr	Prandtl number
\dot{q}	Heat flux per m^2
Q	Flow rate

\dot{Q}	Heat flux
r	Radius
$r_{forward}$	Forward chemical reaction rate
r_{net}	Net chemical reaction rate
$r_{reverse}$	Reverse chemical reaction rate
R	Gas constant
Re	Reynolds number
t	Time
T	Temperature
ΔT	Temperature difference
V	Velocity
\bar{V}	Volume
Z	Depth
α	Linear coefficient of thermal expansion
ν	Kinematic viscosity
ρ	Density
$\sigma_{thermal}$	Thermal stress

Chapter 1. MOTIVATION AND BACKGROUND

1.1. Motivation

Fossil fuels provide the majority of society's energy needs, but they are a finite, non-renewable energy source, and one of the main producers of anthropogenic carbon emissions which contribute to climate change. To address these challenges, alternative energy sources should be developed to assist in meeting global energy demand in a sustainable manner. However, a major drawback of some renewable energy solutions (such as wind and solar) is that they produce power intermittently, thereby creating an urgent need to develop electrical power sources that can meet a variety of generation conditions with relatively rapid response time (i.e., dispatchable). Electrical power generation through the means of geothermal energy is an alternative energy method that satisfies many of these technical barriers. Additionally, rather than having to convert the thermal energy contained in a geothermal resource to electricity it can be used directly to heat buildings, provide hot water, and to meet heating needs for many commercial processes which also represent a large fraction of global primary fossil energy consumption.

The main problem with utilizing geothermal energy is access, and energy density. In most parts of the world this heat energy lies at depths greater than 5 km below the surface (Tester & al, 2006). While there is geothermal heat closer to the surface it is not at a temperature that makes its recovery of interest for electrical power generation. Geothermal heat energy density is low; this means a much larger volume of hot rock

must be exploited to extract the same amount of energy as is contained in a more energy dense source such as oil. Therefore, extensive rather than intensive energy harvesting measures must be considered to make geothermal an available, commercially viable energy source (e.g. widely distributed geothermal power plants rather than geographically/geologically constrained fossil fuel resources).

1.2. Background

Currently geothermal energy is harnessed in three main ways: direct use of the thermal energy, geothermal heating or cooling from heat pumps, and electrical power generation. It is important to note here that the main transport medium for virtually all geothermal energy uses is water.

1.2.1. Direct Use of Geothermal Heat

Direct use is when people use the geothermally heated water directly to accomplish a task such as water or space heating, cooking, or industrial processes. It is harnessed in varying amounts in 72 countries around the world (Fridleifsson, et al., 2008). The prime example is Iceland where direct use accounts for 60% of Iceland's geothermal energy consumption, with ~72% of that (43% of the total) providing residential and commercial space heating to between 89-92% of the population (Iceland's National Energy Authority, 2018). However, due to transportation and development costs, end use is generally limited to locations in close proximity ($\sim < 70\text{km}$) to surface

manifestations or high thermal gradient geothermal heat sources. The importance of close proximity between end use and the source has served to constrain the spread of direct use geothermal. Other barriers to direct use exist in the US and other countries, such as the availability of inexpensive natural gas and oil, an extensive infrastructure to deliver it to homes and commercial buildings, and a lack of incentives for developing renewable low-carbon heating.

From an environmental perspective geothermal is a benign use of energy since it is simply exploiting the natural heat stored in the earth's crust, and it precludes the need for fossil fuel based heating. From a societal perspective, it can reduce space heating costs and provides unique opportunities such as using greenhouses or pools throughout winter, in cold climates, for communities that could not afford these benefits otherwise.

1.2.2. Geothermal Heat Pumps

Geothermal, or ground-source, heat pumps do not utilize geothermal energy in the same way that direct use or electric power generation do. However, many North Americans perceive that the only method of harnessing geothermal energy is a ground-source heat pump when the term “geothermal” is used. To clarify the difference between direct use and heat pumps a concise explanation of geothermal heat pump technology has been included.

Geothermal heating from ground-source heat pumps utilizes the earth's relatively stable temperature for climate control by extracting or depositing heat at depths of greater than 2 to 6 meters, below the surface. The smaller temperature difference between the ground and the building's internal temperature as compared to the outside air allows a ground source heat pump to operate more efficiently than an air source heat pump. Additionally, during the winter months the ground source heat pump reclaims some of the heat rejected to the ground during the summer months and uses it for heating, while in summer time the house utilizes the cooler ground. This stored thermal energy improves the heat pump's coefficient of performance (COP)¹, which is typically in the range of 2-6 for a well designed system. At the seasonal switch the COP can even reach asymptotic numbers of over 100 when the heat pump reverses the refrigeration cycle in the Fall and then again when it is turned back again in the Spring.

From an environmental perspective geothermal ground source heating is an effective method of space heating, because the efficiencies of a heat pump are in the 200-600% range (COP 2-6) whereas an electric heater can only reach a theoretical max of 100% (COP 1). This translates into a decrease in the amount of CO₂ released into the atmosphere for the watts of heating/cooling generated, for regions where electric power comes from burning fossil fuels. Ontario's new Climate Change Action Plan is

¹ Coefficient of performance (COP) is the ratio of useful heat, Q, supplied or removed by the system divided by the work, W, required by that system, = $\frac{Q}{W}$.

calling for the Province to switch to geothermal heating, which if effective should have a significant impact on Ontario's energy consumption (Morrow & Keenan, 2017).

Financial returns on installing a heat pump system can be seen in 5-10 years with a 25-50 year life for the system components (DOE, 2018). Natural Resources Canada estimates that even in Canada's highest electrical power cost areas (rural Ontario) the improvement of geothermal ground source heating is 104% over oil heating and 195% over electrical heating (NRC, 2017). This makes it the most effective method of space heating currently available on the market.

1.2.3. Electrical Power Generation

Geothermal electrical power generation utilizes the heat of geothermal energy to create steam or hot water to vaporize a secondary working fluid for the Rankine cycle. The methods for harnessing this steam to create electrical power can be broken into three main categories: dry steam, flash steam and binary cycle power plants. The differences are: dry steam power plants send high quality steam from the ground directly through the turbines. Flash steam power plants use a lower quality steam created from hot rising water to the surface; typical temperatures are greater than 182°C. The method condenses out some of the water, which is re-injected to the

ground, and then the higher quality steam goes through the turbine. Binary cycle power plants use a lower temperature geothermal water 107-182°C to heat a working fluid² in the closed loop Rankine cycle to power a turbine. These differences between the main types of plants translates into varying levels of CO₂ emissions for each type of plant, see Figure 1.

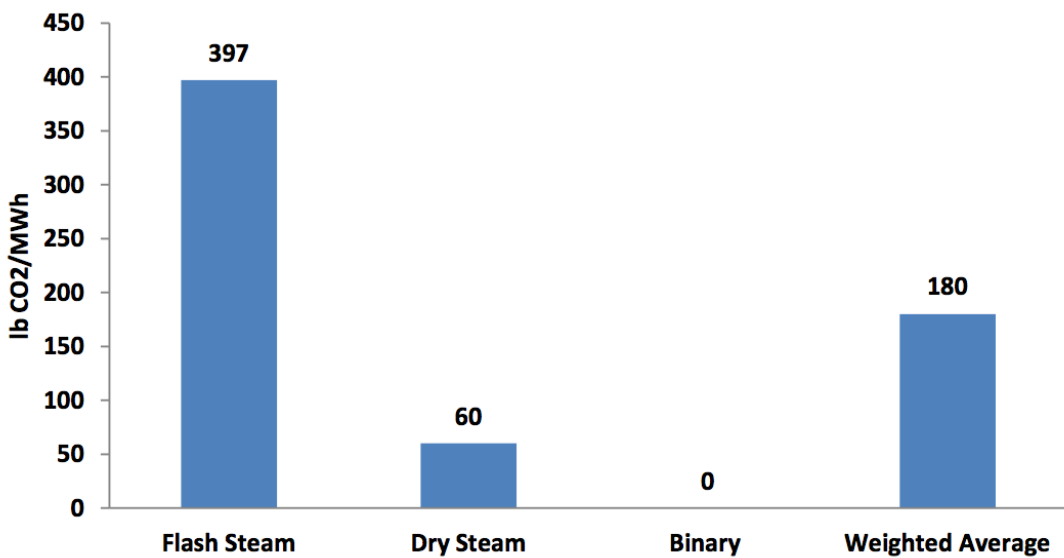


Figure 1. Comparison between three main methods of geothermal electric power generation (Holm, et al., 2012). These numbers are only approximate and will vary widely depending on the dissolved CO₂ contained in the fluid (steam and effluent) produced from a hydrothermal resource.

From an environmental standpoint geothermal energy is more sustainable than fossil fuels. However, due to the variations in CO₂ concentration in geothermal fluid there does not appear to be an academic consensus on how much additional carbon dioxide

² Working fluids are typically hydrocarbon molecules with lower boiling points as compared to water.

is released into the atmosphere due to the exploitation of a geothermal reservoir versus the formations natural emissions, due the complexity of the issue and lack of empirical data. Some reports suggest neutral or even negative CO₂ emissions while others suggest a greater than 50% increase (Holm, et al., 2012). What appears to be clear is that the emissions from a geothermal electric power plant are on average significantly less than a fossil fuels power plant, see Figure 2.

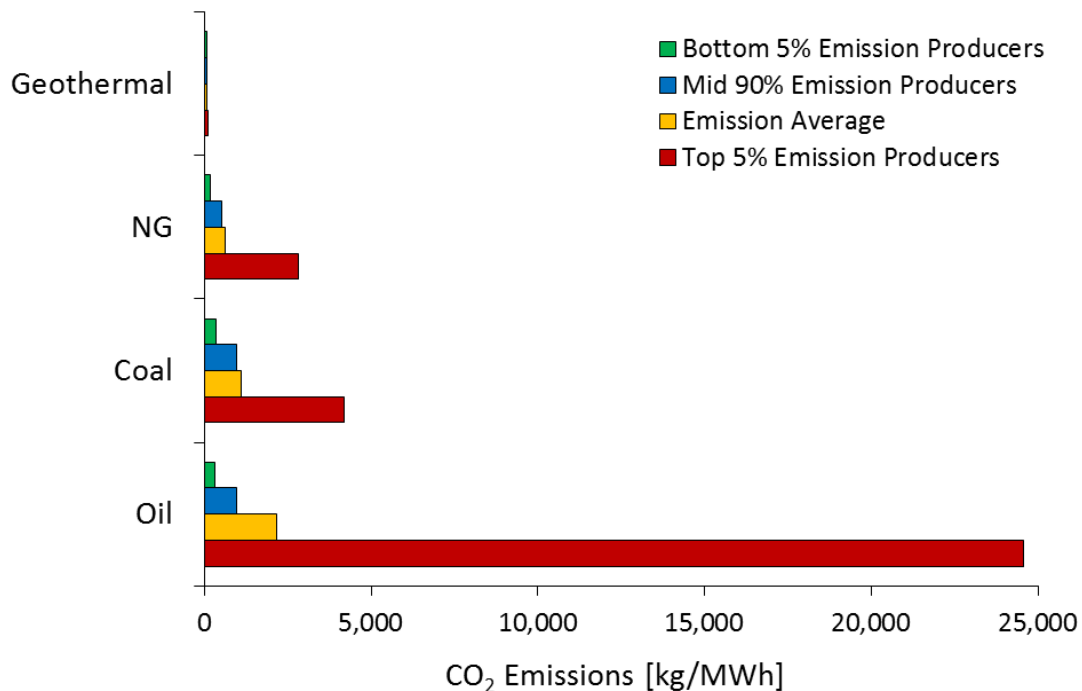


Figure 2. Comparison between oil, coal, natural gas, and geothermal for CO₂ emissions for U.S. electrical power generation (EPA, 2017).

There are a number of disadvantages to geothermal power generation that can affect society. These range from land and water use to power transmission, but these are problems faced by all methods of power generation. The main problem that is different and generates public concern, because it always makes news headlines, is

induced seismicity (i.e. small scale earthquakes). The reason for these seismic events are that some formations used for geothermal power generation are in geologically active areas. Therefore, when a formation is stimulated through water injection it can open and lubricate faults or fractures in the rock formation. This exacerbates the faults' tendency towards reliving stress through slippage, which results in earth tremors (Keranen, et al., 2014); (Harmon, 2009). These seismic risks can be mitigated through thorough geologic investigation prior to the building of a geothermal power plant, by providing essential information for site selection, well location, and informing those planning the risk mitigation strategies. In addition, effective management of subsurface pressures and fluid injection rates may provide a means to limit seismic risk.

1.3. Engineered Geothermal Systems

Geothermal energy is heat energy that comes from the earth's mantle, radioactive decay in the earth's crust, and the cooling of the crust after formation (oceanic crust) or the cooling of the intruded magma (continental crust) (Turcotte & Schubert, 2002). In the engineered geothermal context this geothermal heat energy is transported up towards the earth's surface by conduction and sometimes water movement.

Utilizing geothermal energy for direct space heating or electric power generation relies on a steady source of hydrothermal fluid to create hot water or steam. Creating this hot fluid is easier in geologically active areas since the geothermal heat is closer to the surface such as the Ring of Fire, Mid-Atlantic ridge (Iceland), etc.. Presently,

geothermal development has been primarily focused on moderate to high grade resources where surface expressions and knowledge of a region's structural geology have informed humans about the location of hydrothermal fluids at relatively shallow depths (less than 4 km). However, high temperature geothermal formations can be found anywhere on earth with a well of sufficient depth and utilizing a set of technologies collectively known as an Engineered/Enhanced Geothermal System (EGS).

EGS is a method for utilizing geothermal energy that also relies on hydrothermal fluids like standard geothermal systems. The difference is: EGS can be placed in any location that drilling to reach the deep geothermally heated rock formation can be made economically feasible, Figure 3.

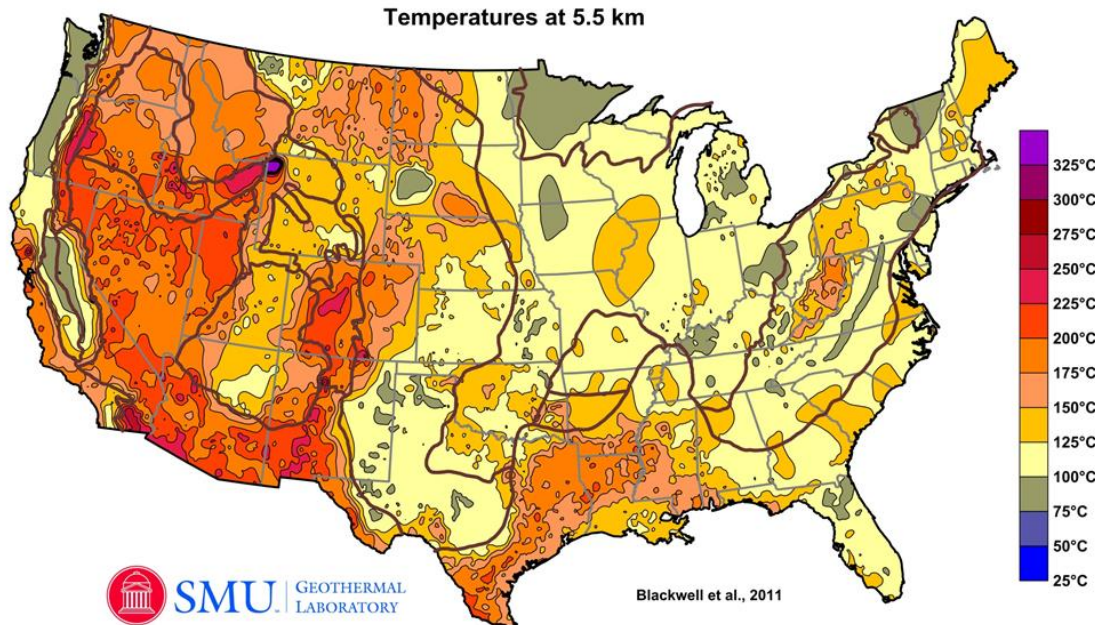


Figure 3. Ground temperature map of the continental U.S. The majority of the U.S. has ground temperatures greater than 125°C at a depth of 5.5 km. (Blackwell, et al., 2011)

In EGS deep wells are drilled around a selected site. Once the wells are completed the ground is often stimulated to create a network of fine fractures throughout the hot rocks. Cool water can then be injected into a well penetrating the hot, dry, subsurface rock formation, and hot water extracted from a nearby production well. See Figure 4. The water is heated as it percolates through the network of fine fractures between the wells, creating superheated water which can be flashed into steam. This superheated water and/or steam can then be used in Dry Steam, Flash steam and Binary cycle power plants depending on the the formation's temperature.

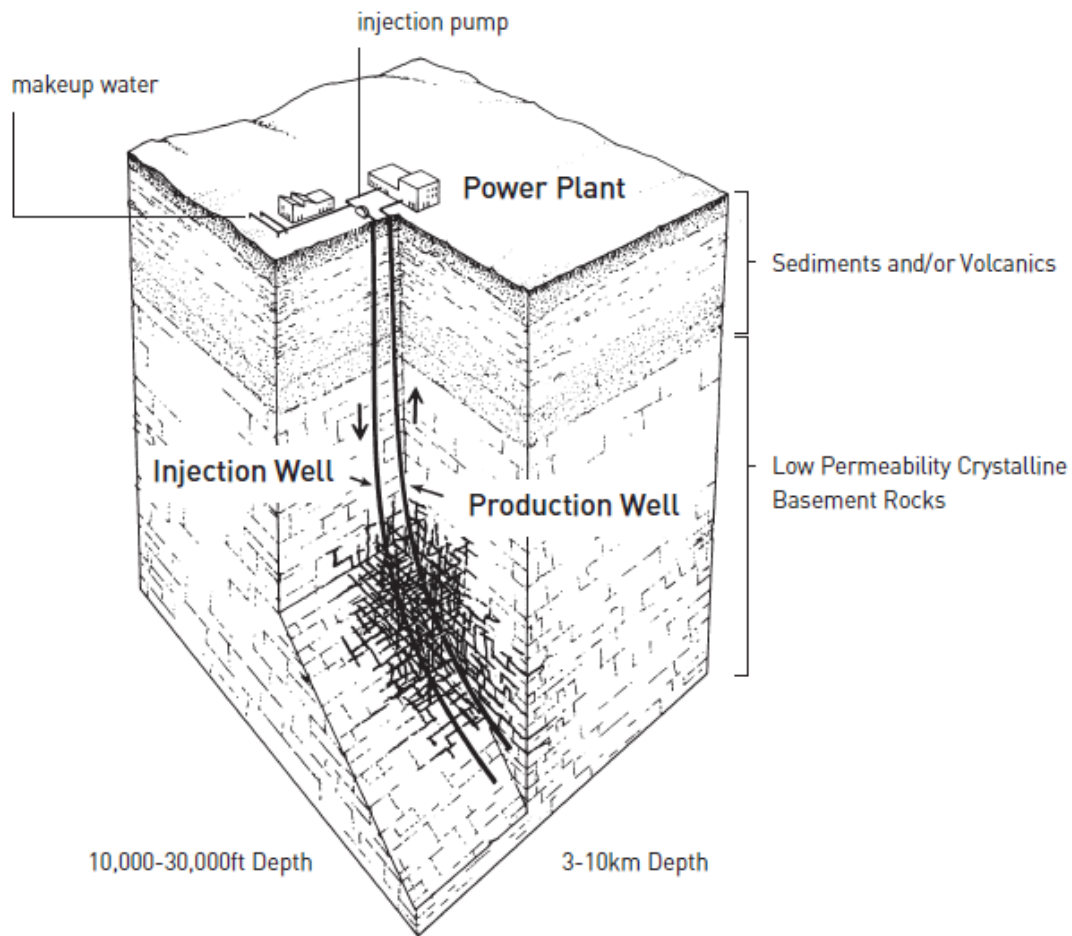


Figure 4. Visual representation of EGS.

Three main challenges to EGS are drilling costs, fluid short-circuiting within the reservoir, and social acceptance and public policy (Tester, et al., 2012). Assuming that with time alternative energy source solutions will be favoured by policy makers and the public, only technical and economic challenges remain.

Short-circuiting is when the water injected into the geothermal reservoir preferentially selects a channel in the fractured formation to flow through. This most often occurs when the permeability of a particular pathway in the rock is significantly greater than

those surrounding it. The result of short-circuiting is that the rock local to the preferred channel is rapidly cooled and therefore the returning water does not reach the required temperature for the power plant to operate. Ongoing research is developing unique polymers that may preferentially block short-circuited channels based on local conditions in the rock such as temperature. Additionally, active research is underway into using reactive and adsorbing tracers to predict the effective volume, size and surface area of geothermal reservoirs (Hawkins, et al., 2016). All of this research is informing the creation of more sophisticated rock fracture and thermal-hydraulic models which can then more accurately predict fractured reservoir performance.

Deep well drilling then remains the major challenge to economically access those resources. To understand the challenges of reaching the required depths for a geothermal reservoir conventional rotary drilling will be discussed.

1.4. Conventional Rotary Drilling

Conventional rotary well drilling is essentially the same process as any other kind of simple drilling in which a drill bit is rotated by motor and this removes material from an opposing surface by abrasion. Like ordinary drilling the diameter of a borehole is limited to the diameter of the drill bit itself; however, because the EGS drill string has to be very long the increased weight, bending, torsion, directionality, etc. rapidly increases the complexity of the drilling process.

In well drilling, a drill bit head is attached to a length of pipe, called a drill string, the pipe is then rotated around by a large motor, see Figure 5 for a schematic of a drilling rig. As the drill bit rotates, it fractures pieces of rock off the bottom of the well. As the hole gets deeper, more pieces of pipe are added to make the drill string longer. To prevent the drilled hole from collapsing in on itself, drilling mud (a high density, viscous mineral sludge) is pumped into the bottom of the hole. This mud serves to keep the bore hole stable through the positive hydrostatic pressure against the walls. Drilling mud's secondary purpose is to remove the crushed rock chips from the bottom of the well as it circulates through the system.

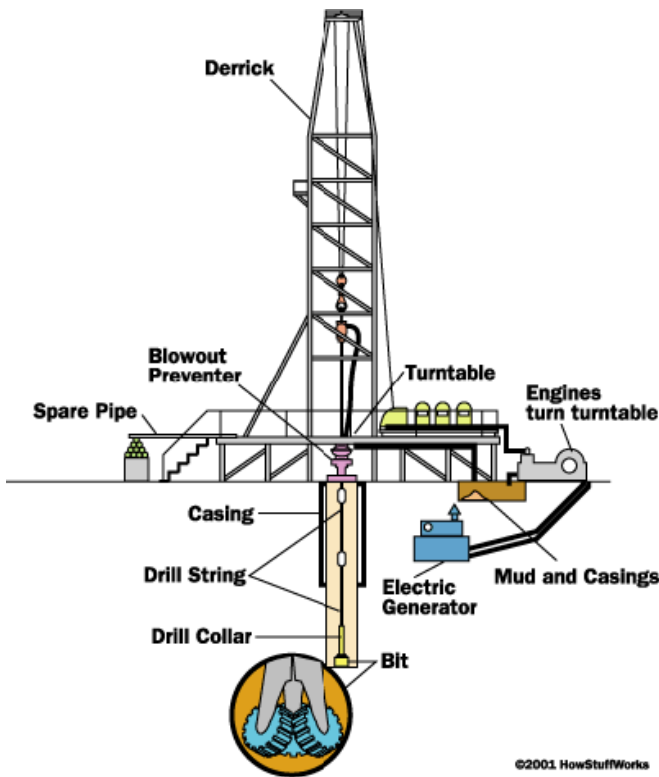


Figure 5. Schematic of a conventional rotary drilling rig (Freudenrich & Strickland, 2001).

Conventional drilling is limited by the lifespan of a drill bit. Several factors contribute to the wear of a drill bit. Firstly, the friction of the drill bit being rotated in direct contact with the rock. Also when the drill string becomes long it is impossible to maintain a straight hole and this unintended deviation can cause additional wear on the drill bit and string, Figure 6. Additionally, the weight of the drill string itself becomes problematic for the drill bit to bear and the drilling rig to control and rotate in very deep wells.



Figure 6. Worn rotary well drilling bits ($\sim 8\frac{3}{4}$ " dia).

Drill bit technology is currently limited by the advances in material sciences. Material engineers are using diamonds and the highest quality alloys to make the drill bits, but even these wear quickly in hard basement rock. The evolution of drill bits in Figure 7 shows that the technology for removing rock through friction caused by a rotating drill bit has essentially remained the same for 130 years of well drilling. By attempting to sustain product innovation through high-cost incremental improvements manufacturers are creating opportunities for a new disruptive drilling technology.

When a drill bit is too worn the entire drill string is removed from the well, this process is called tripping. Tripping is very costly in terms of time and money since hundreds to thousands of meters of heavy pipes have to be lifted, disconnected, and then reconnected and reinserted again after the new bit has been installed. In hard rock, a drill string may need to be tripped every 30 to 100 meters, this makes drilling deep wells extremely costly. Per meter drilling cost increases with increasing well

depth, hence the average onshore well cost can be described as a power function of its measured depth. Using historical data Maciej Lukawski compared drilling and well completion costs for geothermal, oil, and gas wells. He found the overall drilling costs for geothermal wells to be in the 10-20 million dollars range for 4-5 km deep wells, see Figure 8 (Lukawski, et al., 2014). These high drilling costs act as barriers to market entry for companies interested in geothermal power generation. Therefore, drilling innovation that can lower the initial capital investment would likely be embraced by both new and established companies in the industry.



Figure 7. Evolution of conventional rotary drill bits. (Superior Drilling Products, 2014).

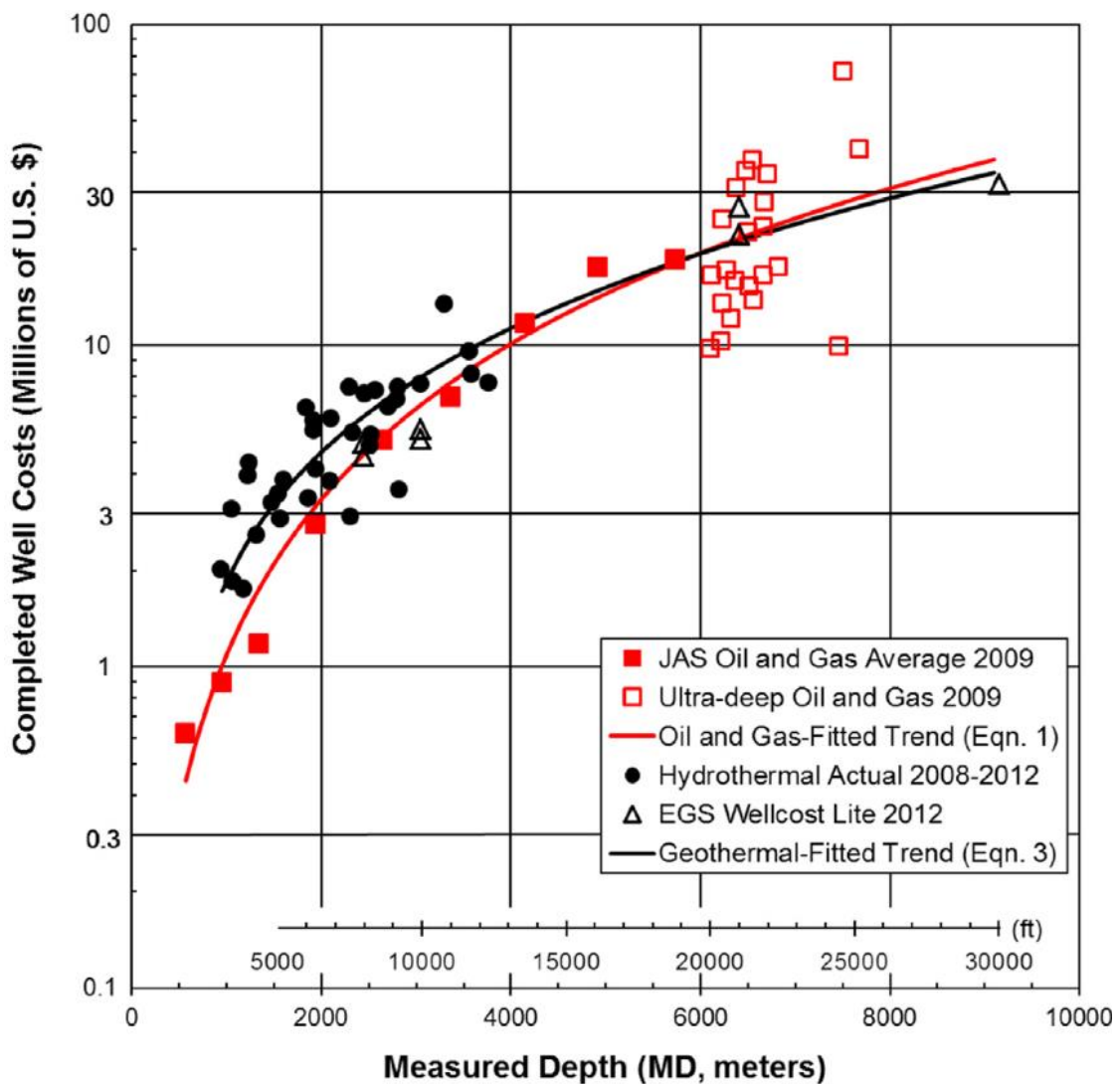


Figure 8. Geothermal well costs (in black) compared to average 2009 oil and gas well costs (in red) (Lukawski, et al., 2014).

Chapter 2. OBJECTIVES AND APPROACH

2.1. Objective and Approach to Project Execution

Low cost, reliable drilling in a hard rock environment is essential for economically viable EGS in today's energy markets. Previous research has attempted to address this drilling challenge by examining flame, laser, and hydrothermal flame spallation (discussed in Chapter 3); however, there is little published information or data on hydrothermal jet spallation. The objective of this thesis is to evaluate the feasibility of hydrothermal jet spallation for deep drilling in granite formations. The primary approach for this work is an experimental study of its effectiveness using electrically-heated water jets at supercritical temperatures and pressures (simulating deep borehole conditions) to thermally spall or comminute Barre Granite.

This goal was broken into six main steps:

- 1) Perform a literature review investigating the previous research.
- 2) Identify how this basic research could be extended using the existing experimental apparatus, and create an experimental roadmap
- 3) Refurbish and upgrade the existing hydrothermal spallation system
- 4) Perform experimentation at supercritical pressures of 22.5-28MPa (225-280bar, or ~3200-4000psi) and temperatures ranging from 535-575°C (~990-1050F)
- 5) Quantify, correlate, and understand the experimental results

2.2. Summary of Project Execution

The literature review of thermal spallation is summarized in Chapter 3. Initial analysis of the implementation of that research to the Cornell Energy Institute's hydrothermal spallation experimental apparatus indicated some significant improvements were required to demonstrate pure water hydrothermal spallation (PWHS), these improvements are discussed in Chapter 4. Successful experimentation followed, which then necessitated quantifying the data generated. Collating, understanding and describing these experimental results fell under the category of filling out the body of hydrothermal spallation knowledge while generating basic research. These initial experimental results are described in Chapter 5.1.

The first PWHS experiments generated additional questions regarding rock temperature and heat flux. To answer these, a second set of PWHS experiments were performed. Contrasting these data to previous work indicated that the primary objective of achieving continuous PWHS had not been realized, Chapters 5.2.3.1, 5.2.3.2, 5.3. However, the result of these experiments was the verification of the lower spallation limit.

The PWHS threshold had been approached but not exceeded so the project returned to an investigation the literature, and then pivoted to introduced hydroxide chemicals into the drilling process. This third set of experiments, chemically enhanced hydrothermal spallation (CEHS) replicated unpublished proprietary work as discussed in Chapter 7. The fourth set of experiments showed that CEHS drilling was directly dependant on

exposure time and solvent concentration, Chapter 7.2.2. The fifth and final set of CEHS experiments used regression analysis to model a drilling rate constant, and through comparison to previous research showed that chemical dissolution was the primary mechanism of CEHS rock removal.

Chapter 3. REVIEW OF PREVIOUS THERMAL SPALLATION DRILLING RESEARCH

A major obstacle limiting wider adoption of EGS and geothermal energy in general is that accessing formations at depths ranging from 3 to 6 kilometers pose a number of drilling challenges. These difficulties include, but are not limited to, the hardness and competency of the constituent rocks, high formation temperatures, and the presence of corrosive salts and ions (Finger & Blankenship, 2010) (Macini & Mesini, 1994), all of which significantly shorten the lifespan of conventional rotary drill bits. Compounding this problem is prohibitive costs of the increased frequency of tripping (Hillson & Tester, 2015). Therefore, alternative drilling techniques that can avoid excessive bit wear and trips would greatly improve the economic viability of geothermal energy development.

Thermal spallation drilling is such a method by which favorable rock formations (quartzitic) can be penetrated at fairly high rates without any bit wear because there is no direct contact between the bottom hole assembly and the rock (Rauenzahn & Tester, 1989); (Williams, 1986); (Rauenzahn & Tester, 1985). The spallation mechanism that has been hypothesized is as follows: a high temperature heat source imposes a very high heat flux, resulting in a steep thermal gradient and commensurate thermal stresses sufficient to induce fracture growth just below the rock surface. The induced thermal stress then combines with residual internal stresses to overcome the inherent tensile strength, Figure 9A. Dislocations and micro-fractures in the rock matrix combine into larger fractures increasing the localized thermal stresses, Figure

9B. The locally heated rock surface then expands against the cooler surrounding rock, and failure occurs when the confining stresses force the thermally expanding rock surface to buckle, violently ejecting the chip from the surface, Figure 9C. If the heat flux at the rock surface is too low, the energy transferred to the rock will not accumulate locally near the surface at a sufficient rate to reach the critical level of thermal stress to cause spallation.

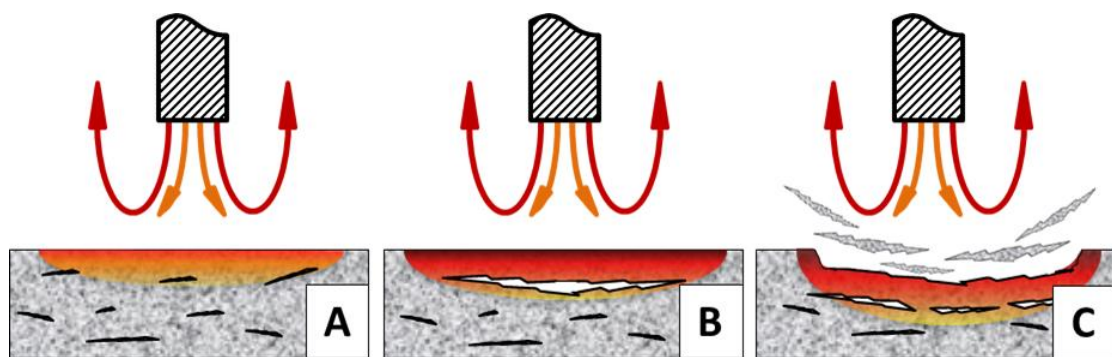


Figure 9. The thermal spallation process. A) Heat applied to the rock induces thermal stress which combines with residual stress and imperfections to create small fractures. B) Stress concentrations cause these fractures combine into significant cracks. C) The increased heating results in spalls being ejected from the rock surface while new fractures are formed.

Low-density flame spallation drilling has been observed in field trials to penetrate about three times faster than conventional rotary drills in hard quartz-bearing igneous rocks such as granite (Wilkinson & Tester, 1993); (Browning, 1981). This makes it a significant improvement over rotary drilling technology because it allows the entire deep well drilling operation to potentially proceed in a single operation, with drill-string trips only needed to install casing rather than multiple trips for bit replacement. With higher penetration rates and fewer trips, the duration of the drilling operation can

be reduced considerably, thereby reducing drilling costs via saving on the rig rental and labor expenses (though some operational costs may be higher).

A key challenge of using flame spallation drilling in very deep wellbores is the pressure of water or drilling fluid in the well to stabilize the hole and assist with lifting comminuted rock. Thermal spallation drilling operations in the field have typically relied on flame jets in open, unpressurized wells, which have a drilling depth limit of about 3km (10,000ft). In response to this problem, research into hydrothermal flames has shown that they can produce under the conditions found in a fluid-filled borehole, but there are multiple obstacles that may be difficult to overcome during real-world implementation (e.g., flame extinguishment, flame (re)ignition, flame jet penetration length into cool co-axial flow, delivery of fuels and oxidants downhole, pressure problems at depths greater than 3,000m, etc.).

However, prior research indicates that it may be possible to achieve the conditions necessary for spallation without the use of flames, and instead employ a supercritical³, or high pressure steam, water jet to attain the desired surface temperature ($\sim 450^{\circ}\text{C}$) and heat flux conditions ($\sim 0.5 \text{ MW/m}^2$) at the rock surface (Wilkinson & Tester, 1993); (Williams, et al., 1988); (Potter Drilling, 2008); (Potter, et al., 2010). Therefore, as stated earlier in Chapter 2 a key objective of the experiments described

³ Supercritical is above the critical point where the distinct gas and liquid phases no longer exist. In this thesis both the supercritical pressure (>22.064MPa, 220.64bar, 3200psia) and temperature (>647K, 374°C, 705F) for water were exceeded and maintained for all experiments.

in this thesis is to determine the low temperature limit at which hydrothermal jet spallation can occur in a supercritical water environment, replicating conditions that would be encountered in deep water-filled boreholes (530-575°C, 22.5-28 MPa) at depths greater than 3km.

3.1. Early Spallation Testing

Initial attempts to describe and quantify the theory of thermal spallation began in 1925 (Norton, 1925). While this early research misidentified some of the main components driving spallation these inaccuracies were soon rectified (Preston, 1932). Early experiments demonstrating the ability of an open flame to drill through rock were performed in Germany in 1927 (Stoces, 1927). While additional papers were written around the early 1930's it appears the technological development of spallation drilling accelerated when flame jets were better understood.

3.2. Open Flame Thermal Spallation

One method of charting the practical development of thermal spallation drilling using flame jets in open boreholes is the issuance of U.S. patents. One of the earliest patents which describes a method for thermal drilling was US2111872 “*Method of and apparatus for quarrying and shaping rock and stone*” filed on November 6th, 1933 (Rea, 1938). It describes a drilling technology that involves rapidly heating and cooling the rock face to prompt spallation. Other patents for thermal spallation drilling

that did not require periodic cooling such as US2327496, US2426688, and US2548463 followed in 1939. However, one of the earliest commercially successful thermal drilling devices used for quarrying hard rocks came from Union Carbide.

In 1954, Union Carbide received patent US2675993 “*Method and apparatus for thermally working minerals and mineral like materials*” (Smith & Mitchell, 1954), and US2675994 “*Thermal mineral piercing method and apparatus*” (Calaman, et al., 1954). This open flame thermal spallation drilling technology enabled quarries to selectively remove rock with a flame jet, thereby avoiding the loss and damage caused through the use of dynamite.

Open flame thermal spallation flame drilling experiments culminated when James Browning between 1963 and 1969 received six patents for flame spallation (Maurer, 1980), and in conjunction with Los Alamos Labs drilled a well in granite to a depth of about 330 meters in Conway, New Hampshire (Browning, 1981). Browning’s tests were estimated to reach drilling speeds of up to 30m/hr (Wilkinson & Tester, 1993). However, this field demonstration of open flame thermal spallation was in a mostly, dry borehole (not water or drilling fluid filled) which represents only a very small amount of the commercial wells being drilled.

Rick M. Rauenzahn’s PhD thesis at MIT encompassed basic research into flame spallation that ranged from process modelling to lab scale experiments and finally field testing (Rauenzhan, 1986). Rauenzahn investigated the rock failure mechanics and the influence of gas jet fluid dynamics during the thermal spallation process. He proposed the use of the Weibull distribution to model the probability of rock failure

during spallation based on rock flaws, inherent rock properties, rock surface temperature, and heat flux (Rauenzahn & Tester, 1989). His field-scale flame spallation experiments achieved drilling rates of 7.31m/hr and 6.31m/hr in Barre and Westery Granite respectively.

The doctoral research by Mark A.Wilkinson, also at MIT, expanded on the work done by Rauenzahn. In his thesis Wilkinson investigated spallation using a lab scale flame jet and an industrial 25kW laser (Wilkinson, 1989). He focused on experimental measuring and modelling the rock surface temperature and heat flux from the impinging jet or laser using a computational fluid mechanics approach (the primary purpose of the laser tests were to independently measure the initial spallation surface temperatures and heat fluxes with IR thermal imaging). Wilkinson's experimental and computational modeling studies generated the data that correlated thermal spallation (flame and laser) rates to surface temperature and impinging heat flux using a Weibull distribution.

Both the in-laboratory and field-scale research into open flame spallation, and to a lesser degree laser spallation, was successful at demonstrating the effectiveness of thermal spallation. It also proved that competitive drilling rates were achievable. However, the wider adoption of thermal spallation drilling necessitates a technology that employs a drilling fluid/mud to provide positive pressure for well stability. Therefore, while open flame thermal spallation may become a viable option in fluid filled boreholes in the future the current technology appears inadequate to meet a wide range of practical challenges.

3.3. Hydrothermal Flame Spallation

Hydrothermal flames are defined as the combustion of a fuel with an oxidant in an aqueous solution that can reach a temperature sufficient to generate a visibly luminescent flame. These flames were initially investigated by Schilling in 1988; however, these experiments were largely a semi-batch process in which an oxidant was injected into a fuel water mixture. The hydrothermal flame would burn in the sealed chamber until the fuel mixture was depleted extinguishing the flame (Schilling & Franck, 1988). Continuous hydrothermal flames have been achieved by the combustion of a stream of heated aqueous fuel and an oxidant injected into a high pressure aqueous environment. These hydrothermal flame jets have been examined extensively by ETH Zurich for over 20 years (Roche, 1996), and at MIT by Chad R. Augustine (Augustine, 2009). These studies highlighted the complexity of stimulating and maintaining a hydrothermal flame at supercritical pressures based on the complex interactions between the reactants and oxidants in a confined aqueous environment at high pressure. Augustine describes the sensitive intricacies of hydrothermal flames as sufficient in magnitude to disrupt the repeatability of experiments even when maintaining identical conditions (Augustine, 2009).

The application of hydrothermal flame jets in spallation drilling was viewed as a solution to the problems faced by open flame thermal spallation in deep boreholes where high density fluids at depths greater than 3 kilometers are encountered (Potter & Tester, 1998); (Potter Drilling, 2008). By impinging a hydrothermal flame on an immersed rock face, spallation can be achieved in a pressurized aqueous environment.

One of the main problems faced by hydrothermal flame spallation technology is the increased rate of convective heat loss to the surrounding higher density aqueous solution as compared to an open air flame jet at lower densities. This means the hydrothermal flame jet must be very close (<5mm) to the perpendicular rock face to prompt significant spallation, even then the surface area spalled by the hydrothermal jet is small relative to the applied heat when compared to open flame spallation. Another significant challenge is the reliable ignition and re-ignition of the hydrothermal flame in an aqueous environment. Therefore, although rock spallation has been achieved using hydrothermal flame jets it is a complex, difficult to regulate process that has produced mixed results (Augustine, 2009).

3.4. Hydrothermal Jet Spallation

The most recent/successful hydrothermal jet spallation experiments occurred in 2007. Bob and Jared Potter of Potter Drilling initially examined electrically heated hydrothermal jets; however, they were unable to heat the water jet past the temperature of 420°C so they switched to chemically induced water heating using a catalyst (Potter Drilling, 2008) (Potter, et al., 2010). *In situ* chemical heating from the exothermic reaction enabled the steam jet to reach temperatures of over 850°C. This high pressure steam jet induced rock spallation in Sierra White Granite, and Berea Sandstone at fluid temperatures greater than 700°C. Successful field scale drilling experiments were conducted using the chemically heated steam jet to a depth of 30 meters. In their experiments Potter Drilling filled the wellbore with water but kept the

steam jet separated from the cooler circulating water. This separation of cool drilling fluid from the hot steam jet avoided the problem of high convective heat losses which limits the effectiveness of hydrothermal flame jets. However, in their tests Potter Drilling was unable to spall in a perfectly vertical path due to the natural inhomogeneity of the rock matrix guiding the spallation drilling head, nor were they able to maintain a steady borehole diameter when drilling. Variable borehole diameters resulted when the hydrothermal spallation jet head slowed in any section of the well during the course of drilling. Since the steam jet could not be turned off the excess heat prompted spallation of the surrounding well walls, increasing the overall diameter of the wellbore. The increased diameter of the wellbore caused the steel spiral brushes, or flower pedal expanding type holding back the drilling mud to collapse thereby flooding the lower steam jet chamber, and effectively halting spallation. This problem of inconsistent well bore diameter was considered by Jared Potter to be the main challenge to hydrothermal steam jet drilling for deep wellbores, and served as the primary reason he concluded that a conventional rotary drilling/lower temperature hydrothermal spallation hybrid system was preferable to either of these well drilling solutions on their own. This study attempted to address the problem of inconsistent wellbore diameter due to excess steam heat by examining lower temperature, higher density supercritical fluid jets as a way of controlling corybantic radial expansion.

Chapter 4. EXPERIMENTAL APPARATUS AND PROCEDURES

4.1. Description of Experimental Apparatus

A high temperature and pressure spallation reactor system capable of delivering a hydrothermal jet of supercritical deionized water up to 600°C and 31 MPa (310 bar, 4,500 psi) was used in this study. The design was based on an original 2007 design of Jared Potter and co-workers at Potter Drilling which was later modified at the Cornell Energy Institute over a 5-year period (Hillson & Tester, 2015). Pure deionized water was used for the hydrothermal jet and heated by a series of electrical heaters totaling 14.8 kW (Augustine, 2009), with over 90 percent of this available energy delivered to the exiting fluid jet before it impinges upon the rock face. The main reactor accommodates a 2.54 cm diameter, 8 cm long cylindrical Barre Granite rock sample, and has a cap fitted with sealing O-rings that allow the jet to impinge directly on the rock surface in an isolated environment; see Figure 10B. The reactor is contained within a larger pressure vessel that is limited to a maximum temperature of 80°C to ensure safe operation. See Figure 11 for a complete piping diagram of the experimental system, and Figure 12 for a photograph of the actual system.

While pressurized water is being heated to the desired supercritical temperature, the reactor is positioned in the lower (cooler) part of the pressure vessel, so that the rock sample remains in fluid at a temperature less than 80°C. Holding the sample at this

lower temperature avoids thermal expansion due to gradual heating which would occur if the sample were located closer to the hydrothermal jet.

To perform a comminution experiment at a desired jet temperature, the granite sample is raised under pressure from the lower part of the containment vessel to the top where the hydrothermal jet impinges on its top surface. A cooling water jacket envelops the remaining sides of the rock sample, see Figure 10C, to keep the bulk rock sample cooler. The external cooling water jacket counteracts the intense heating by the hydrothermal jet, thereby limiting the tendency of the small rock sample to relieve stress through thermal expansion and providing some level of confining stress. These two features: raising the sample, and the cooling water jacket, increase the thermal gradient and thermal shock at the top surface of the rock sample. The reported time of a comminution experiment begins once the rock sample of Barre Granite has been fully raised into the impinging supercritical water jet.

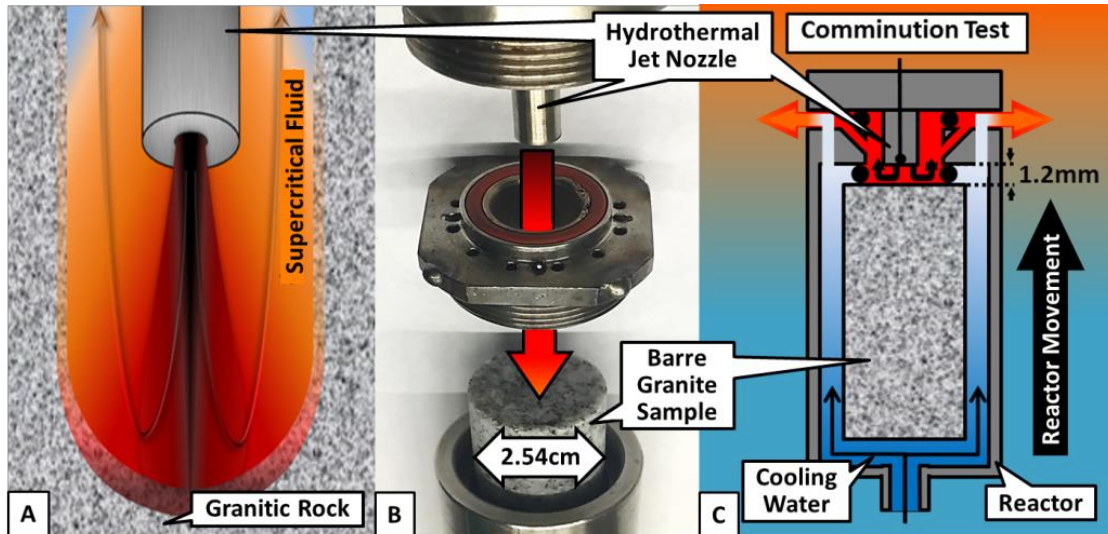


Figure 10. A) A sufficiently high temperature fluid impinging on a granitic rock surface induces a large thermal gradient in the rock resulting in rock removal by spallation (drilling). B) Experimental apparatus arrangement of 2.54cm diameter Barre Granite rock sample. C) The reactor chamber containing the rock sample and cooling water can be moved vertically upwards into the hydrothermal jet to increase thermal shock of the impinging fluid. The movement of the reactor chamber is bi-directional along the centerline allowing the rock sample to retract from the hydrothermal jet, halting the experiment at a selected time interval.

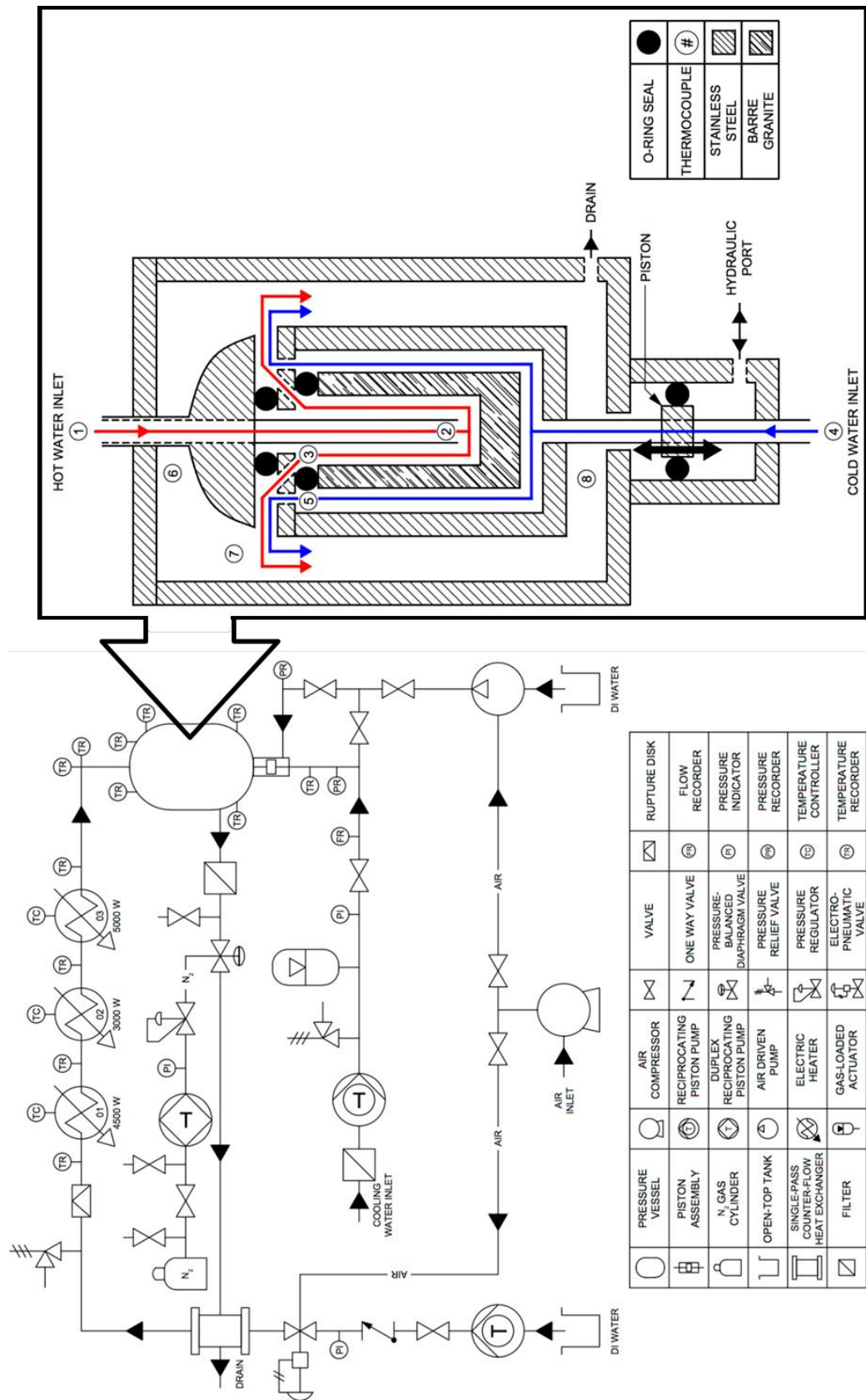


Figure 11. System piping and instrumentation diagram.

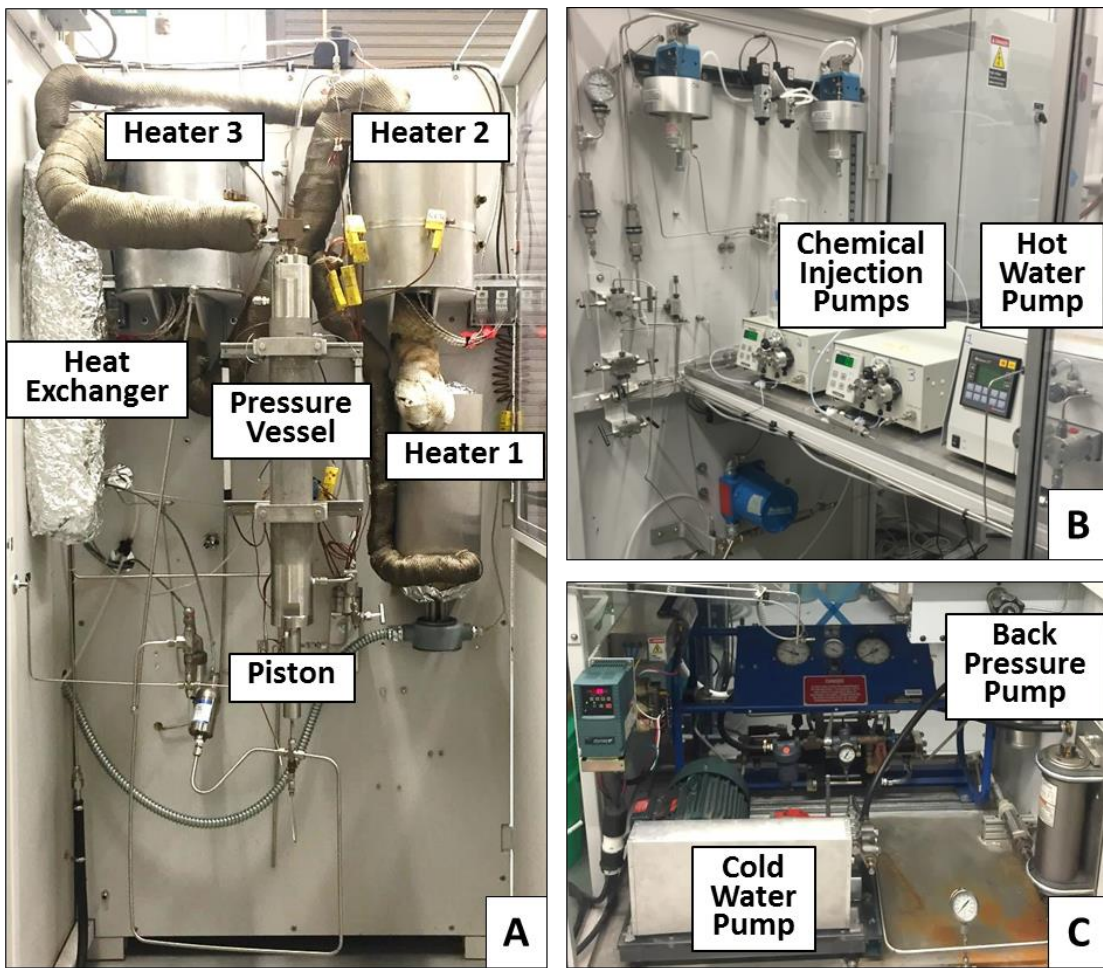


Figure 12. High temperature and pressure spallation apparatus. A) Main reactor and heaters. B) Hot water and chemical injection pumps. C) Cooling water pump, and back pressure system.

A significant difference between these hydrothermal spallation tests and flame spallation (using combustion) is the high pressure and high fluid density environment surrounding the sample. The initial hypothesis was that the supercritical water jet could deliver a higher heat flux to the rock sample's surface at a lower jet and rock surface temperature because of the higher density and thermal conductivity of the

supercritical water as compared to combustion exhaust gases previously used in thermal spallation experiments.

The hydrothermal spallation experimental apparatus required modifications to reach the minimum fluid temperatures needed for initiating spallation. These system changes were separated into two parts: increasing the jet temperature into the 500-600°C range, and preventing the gradual thermal expansion of the rock sample when heated. The first problem was addressed by manufacturing a high pressure heat exchanger for preheating the deionized feed water using the system's hot waste water, and by adding a third electric water heater (4500W) to increase the overall temperature, Figure 13A,B. This allowed the water inside the heaters to reach temperatures of 615°C. Higher temperatures were not investigated due to safety concerns of mechanical failure, creep, and the corrosion of the Inconel Alloy 625 tubing used in the heaters manufacture.

The second problem of providing confining stress was partially achieved by employing a hydraulic piston to raise the granite rock sample into the hydrothermal jet only once the three electric heaters had reached steady state, Figure 13C. Additionally, incoming cooling water was routed around the outside surface of the granite rock sample to provide external cooling; thereby, inducing a strong thermal gradient (up to 400°C/mm axially and 130°C/mm radially) in the rock sample while maintaining circumferential thermal stress at the top surface, Figure 13D. The better approach would be to use mechanically applied axial and horizontal/circumferential stress, but this technique was not used in this study due to time and cost constraints.

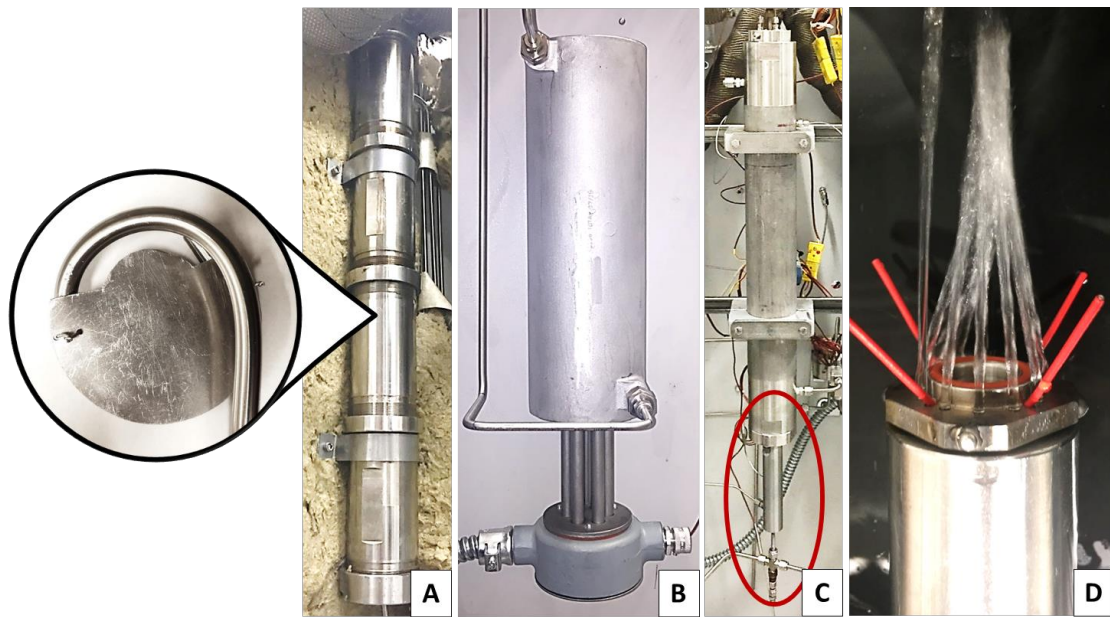


Figure 13. A) High pressure heat exchanger for preheating super critical jet, and the profile of the internal baffles. B) Additional high temperature water heater. C) Hydraulic piston for raising the granite rock sample into position. D) Cooling water flow pattern to prevent gradual thermal expansion of the rock sample; red straws indicate the flow path for hot effluent exiting the comminution chamber.

Gradual heating of a rock allows it to expand with time reducing the internal stresses created by thermal expansion. This change in the dimensions of a material, Δl , is approximated using a constant linear coefficient of thermal expansion α

$$\alpha = \frac{l_f - l_o}{l_o(T_f - T_o)} = \frac{\Delta l}{l_o \Delta T} \quad (4.1)$$

Where l_o , ΔT , and E are: initial length, temperature difference and Young's Modulus.

The thermal stress, $\sigma_{thermal}$ is related to α by:

$$\sigma_{thermal} = \alpha E \Delta T \quad (4.2)$$

This equation shows that the changes to the hydrothermal spallation reactor by isolating the hot water jet, adding a cooling water jacket, and the hydraulic piston significantly increased the thermal stress to the rock by increasing the ΔT . The temperature difference between the center of the rock sample's top surface and its circumference increased by an order of magnitude from $40 \pm 20^\circ\text{C}$ to $400 \pm 20^\circ\text{C}$, improving the quality of the experimental results.

Three types of hydrothermal spallation tests were performed using pure water jets to stimulate spallation. Figure 14 schematically shows these tests. The first was a direct impinging of the supercritical jet onto the rock samples' top surface to prompt spallation (Chapter 5.1). The second set of tests examined the surface temperature of a sample undergoing spallation (Chapter 5.2.3.1), and the third measured heat flux during a spallation test (Chapter 5.2.3.2). Each of these three tests will be discussed in more detail.

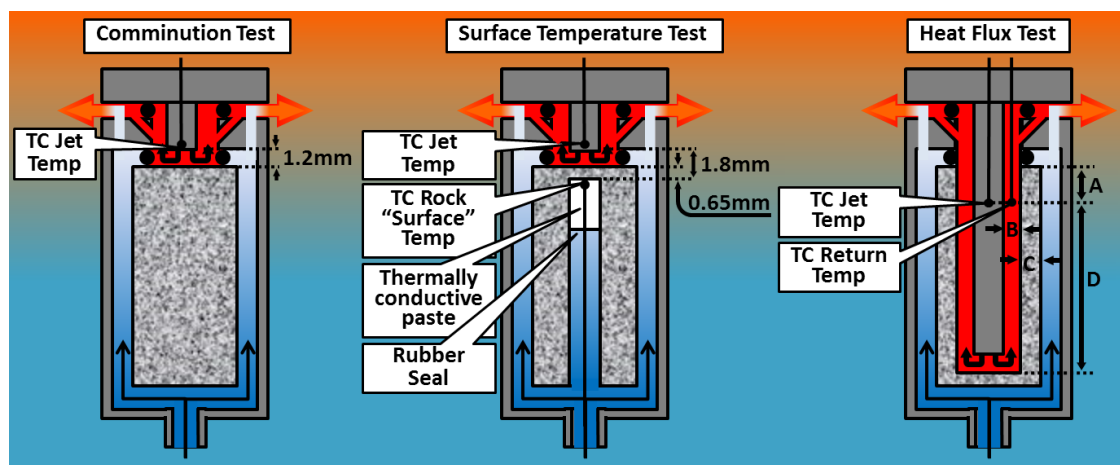


Figure 14. Three types of tests performed. **Comminution Test**, is the experimental arrangement of a spallation test, with and without chemical enhancement. **Surface Temperature Test**, records the rock temperature just below the sample's surface. **Heat Flux Test** measures energy flux during an experiment.

4.2. Measurement Uncertainty

The sources of uncertainty in the experimental measurements were identified as functions of system instrumentation, and fluid state properties. Using the Moffat method (Moffat, 1985) the error was estimated to be:

$$Error = \sqrt{\frac{[(Qh\delta\rho)^2 + (\rho h\delta Q)^2 + (\rho Q\delta h)^2]_{hot\ in}}{+[(Qh\delta\rho)^2 + (\rho h\delta Q)^2 + (\rho Q\delta h)^2]_{cold\ in}} + \left[([Q\delta\rho]_{cold\ in}h)^2 + ([\rho\delta Q]_{cold\ in}h)^2 + ([\rho Q]_{cold\ in}\delta h)^2 + ([Q\delta\rho]_{hot\ in}h)^2 + ([\rho\delta Q]_{hot\ in}h)^2 + ([\rho Q]_{hot\ in}\delta h)^2\right]_{out} + (\delta P)^2 + (\delta T)^2} \quad (4.3)$$

The full derivation for Equation (4.3) along with the uncertainty analysis is found in Appendix A-1. The delta terms refer to individual fractional uncertainties in the specific variables (Q , h , ρ , P , & T) which are flow rate, enthalpy, density, pressure, and temperature, respectively. The combined error associated with the temperature, pressure, and flow rate sensors, including the fluid state properties were calculated to be less than 1.75% in the 400-600. Estimated measurement errors are shown in Figure 15 as a function of fluid temperature within the temperature range studied.

Experimental design was central to the accuracy of the data measurements. Each experimental configuration was checked by three independent parties to identify flaws; however, it should be noted that the uncertainty calculations are associated with the precision of the data measurements combined with water's state properties. They do not consider that a sensor may have been mounted in a less than optimal location to measure the phenomena. The overall accuracy of the apparatus was impossible to

estimate (problem common to many experimental systems), but this was accounted for by doubling the uncertainty associated with crucial predictions.

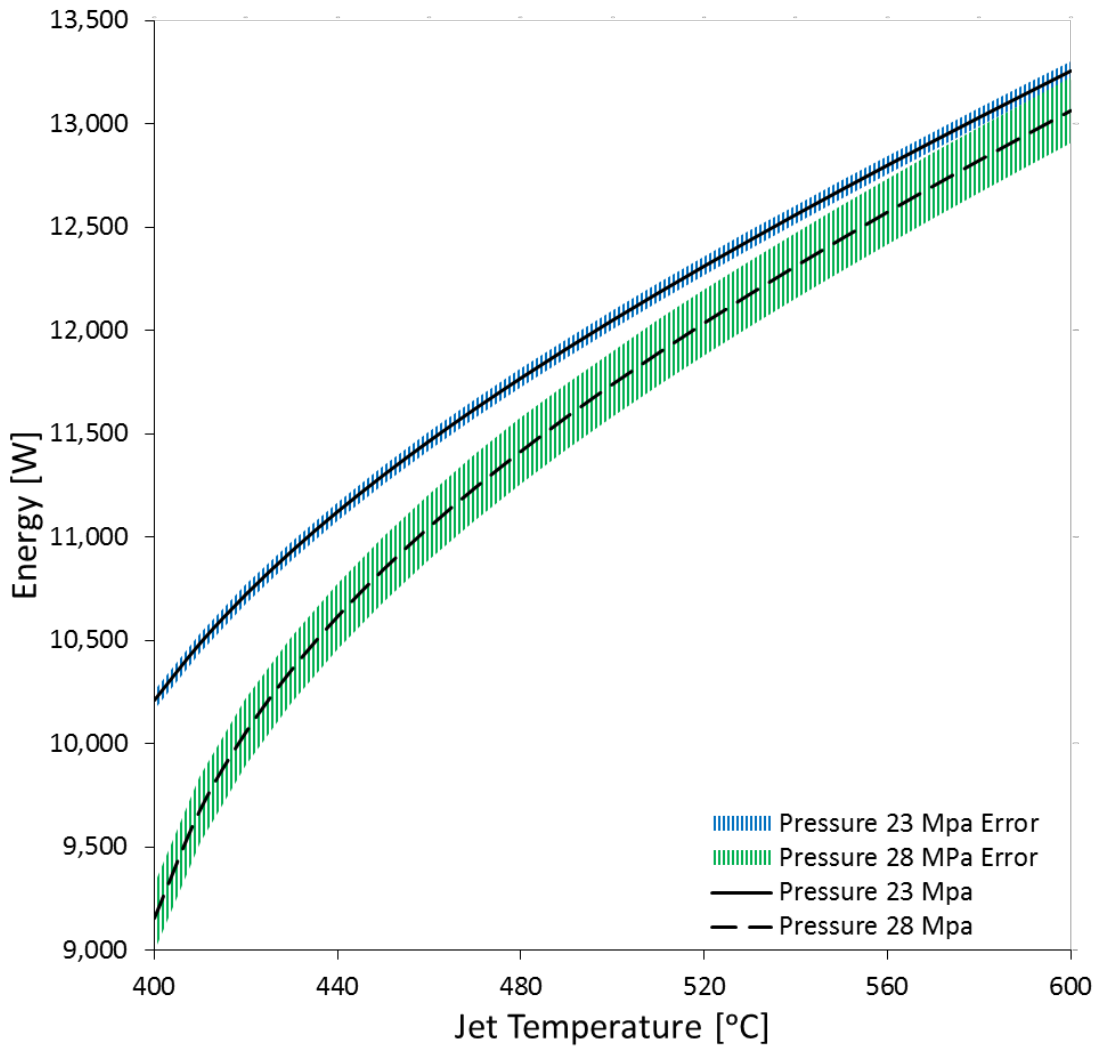


Figure 15: Range of uncertainty for energy calculations based on the impinging jet temperature.

Chapter 5. PURE WATER HYDROTHERMAL SPALLATION RESULTS

5.1. Quantifying Experimental Results

A series of spallation tests were run at jet temperatures between 535 and 575°C. Hydrothermal comminution was achieved in all samples. Figure 16 shows the results for Barre Granite before and after exposing the surface to the supercritical water jet. Quantifying the type and amount of mineral comminution that occurred required further experimentation.

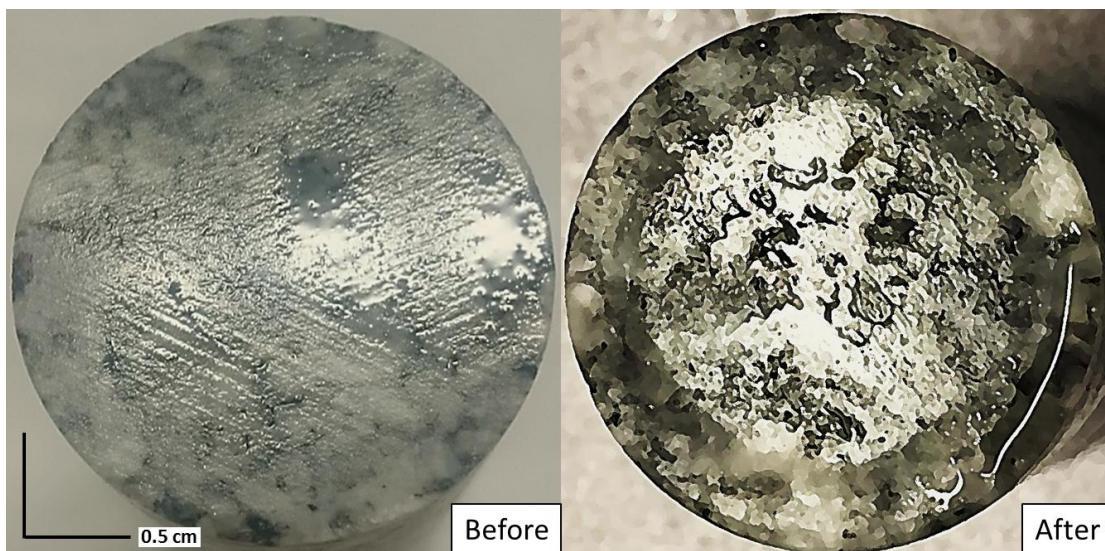


Figure 16. Before and after a spallation experiment. The largest spalls ~3mm across and 0.3-0.5mm deep. Striations on the before sample are saw marks.

Fifteen comminution tests at differing temperatures and pressures were performed, see Figure 17. The amount of damage to the samples' impinged surface corresponded in a non-linear fashion to the residence time in the reactor. The experimental pressures ranged from 22.5 to 27.6 MPa, temperatures 535-575 °C, and exposure times from 10 seconds to 30 minutes.

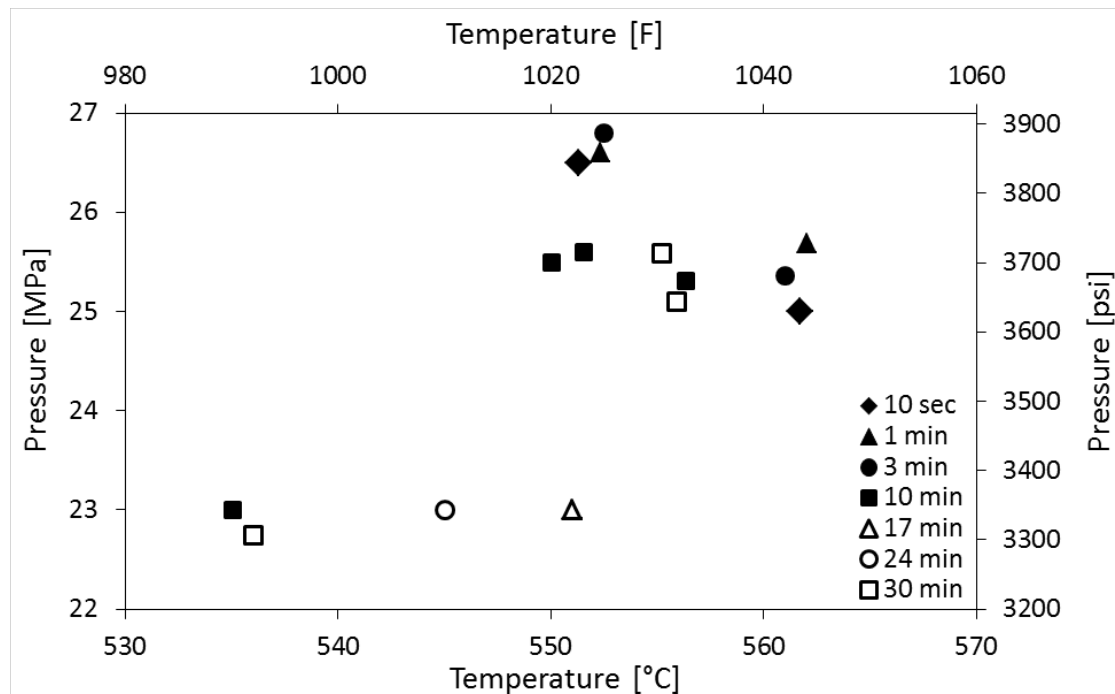


Figure 17. Spallation experiments with their associated pressures, temperatures, and time durations. Data in Table 3, see Appendix B-1.

5.1.1. Preferential Comminution of Quartz

The experimental results of the comminution tests were quantified by scanning a sample's top surface prior to the experiments with the Scanning Electron Microscope (SEM) to determine crystal/mineral composition (see Figure 18). After the

experiments they were examined with a Laser-scanning Confocal Microscope (LSCM) which acted as a profilometer measuring the amount of mineral removed (see Figure 19). The comminution tests consistently resulted in heterogeneous removal of surface material. Comparing the diminished areas to the SEM mineral map it was determined that exposing Barre Granite to a supercritical water jet preferentially removes quartz crystals, see Figure 20. Additionally, the boundaries of the subducted quartz grains are very distinct which further strengthens the argument for preferential removal of silica; however, no rock spalls were recovered from these experiments.

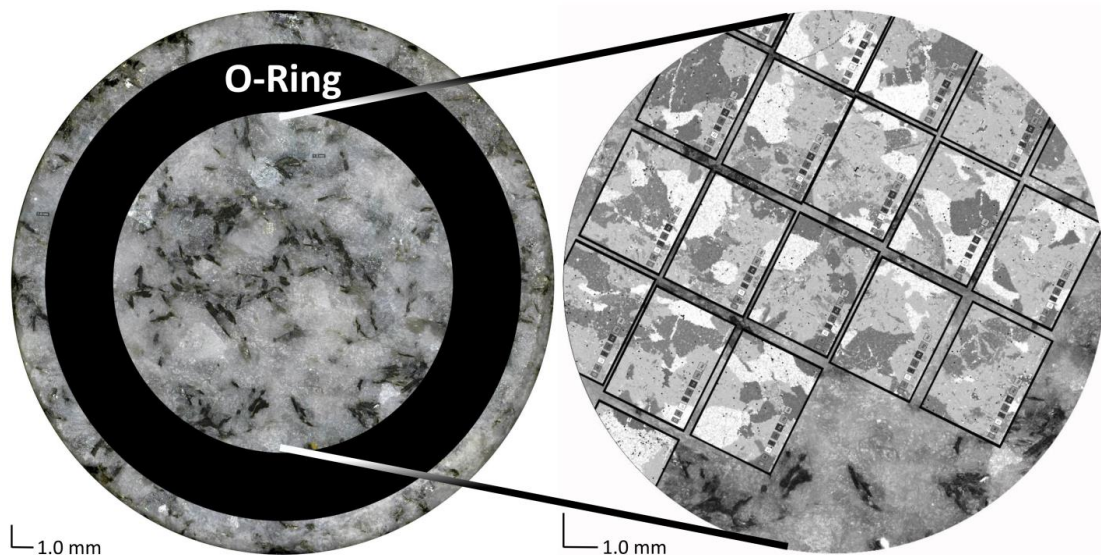


Figure 18. An o-ring separates the area exposed to supercritical water (in the centre of the granite samples's top surface) from the cooling water that surrounds the sample. The SEM images can be seen overlaid on the area of interest.

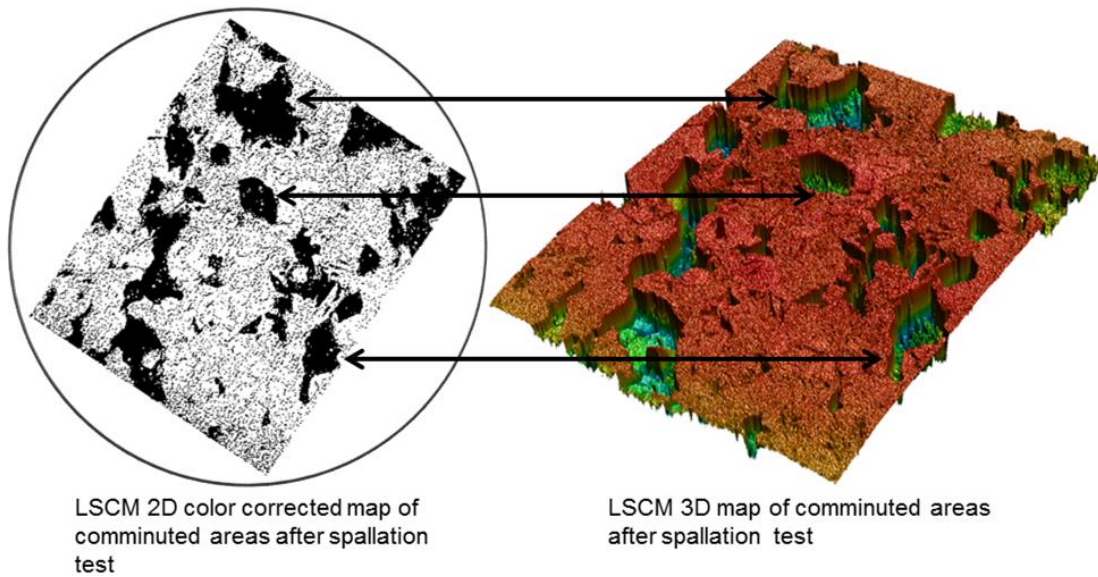


Figure 19. LSCM test acting as a profilometer to determine the subducted areas.

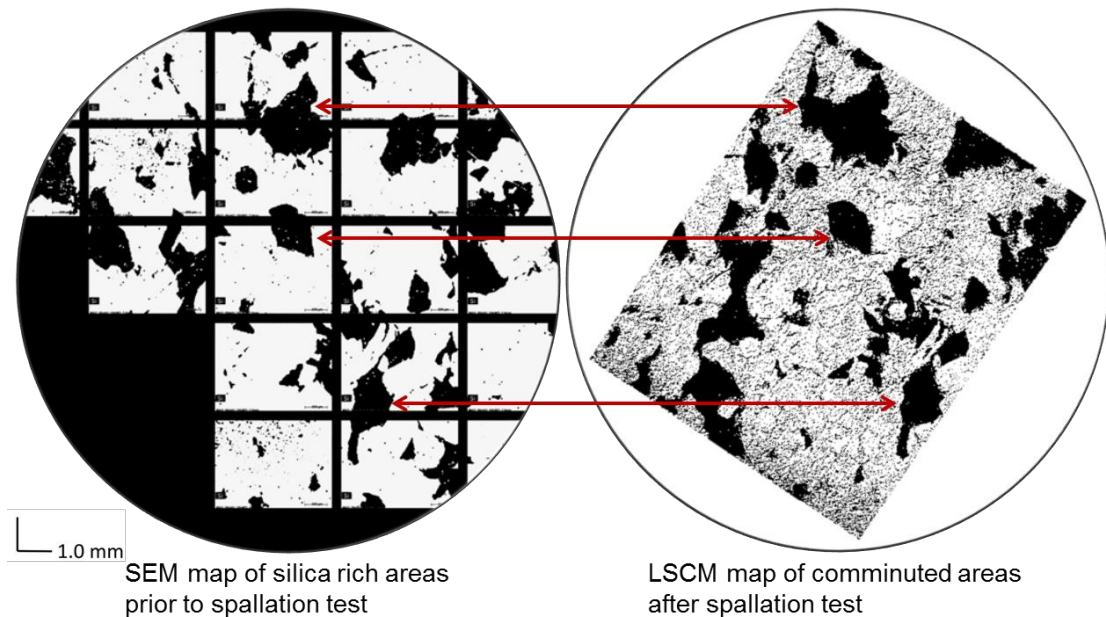


Figure 20. The SEM silicon element (Si) scan of the unspalled rock sample's surface which highlights the silica rich quartz zones, compared against the LSCM scan of the same sample's post-communition test surface. The colour-corrected 'black' quartz crystals in the SEM image and the 'black' subducted areas in the LSCM comminuted image correspond to each other. Observation indicates that quartz crystals are preferentially removed.

The average composition of the Barre Granite sample testing was 27.2% quartz, 19.4% potassium feldspar, 35.2% sodium feldspar, and 15.4% mica, with other minerals comprising the balance (Chayes, 1950); see Table 1. Preferential removal of quartz can be partially attributed to the difference in the coefficient of volumetric thermal expansion of quartz ($4.98 [10^{-5}/^{\circ}\text{C}]$) and feldspar ($\sim 2 [10^{-5}/^{\circ}\text{C}]$). A greater than 2:1 ratio between these principal components (Robertson, 1988) is sufficient to cause increased thermal stress. However, the quartz removal mechanisms of erosion and dissolution must be considered before inferring that spallation has occurred. Note that since the impinging jet temperature was below 573°C , the α - β quartz phase transition should not play a role in its preferential removal.

Table 1: Properties of Barre Granite (Chayes, 1950) (Robertson, 1988)

Mineral	Formula	Composition Range	Composition Mean	Volumetric Thermal Expansion*	Thermal Conductivity **
		%	%	$10^{-5}/^{\circ}\text{C}$	W/mK
Quartz	SiO_2	24.3 - 32.7	27.2	4.98	4 - 6.3
Microcline (K-feldspar)	KAISi_3O_8	12.5 - 24.8	19.4	1.79	1.6 - 2.4
Plagioclase, (Albite)	$\text{NaAlSi}_3\text{O}_8$	30.3 - 40.4	35.2	2.24	1.7 - 2.3
Biotite	$\text{K}(\text{Mg},\text{Fe})_{2-3}\text{Al}_{1-2}\text{Si}_{2-3}\text{O}_{10}(\text{OH},\text{F})_2$	0.2 - 16.0	8.1	-	-
Muscovite	$\text{KAl}_2(\text{Si}_3\text{AlO}_{10})(\text{OH})_2$	4.5 - 11.2	7.3	-	-
Other	CO_3^{2-} etc.	0.5 - 4.2	1.8	-	-

* averaged over the 20-400°C range, ** at 500°C

5.2. Comminution Mechanisms

The preferential removal of quartz during PWHS can be narrowed to three primary mechanisms: erosion, dissolution and spallation. Each of these three mechanisms were investigated to determine their significance in quartz comminution.

5.2.1. Erosion of Quartz

Flow stress or erosion, by the impact of the supercritical water on the sample's surface, were not found to be contributing factors to comminution. At the experimental conditions, the maximum velocity associated with the supercritical jet was only 9 m/s, with a fluid density of about 70 kg/m^3 , and a dynamic pressure difference between the jet nozzle and the rock surface less than 2 kPa, see Figure 21. The impinging pressure difference is about 5 orders of magnitude less than the pressure used to cut (erode) Barre Granite with a high velocity water jet (Summers, 1972). Additionally, as seen in Figure 22, the acute edges along quartz boundary lines show no signs of erosion.

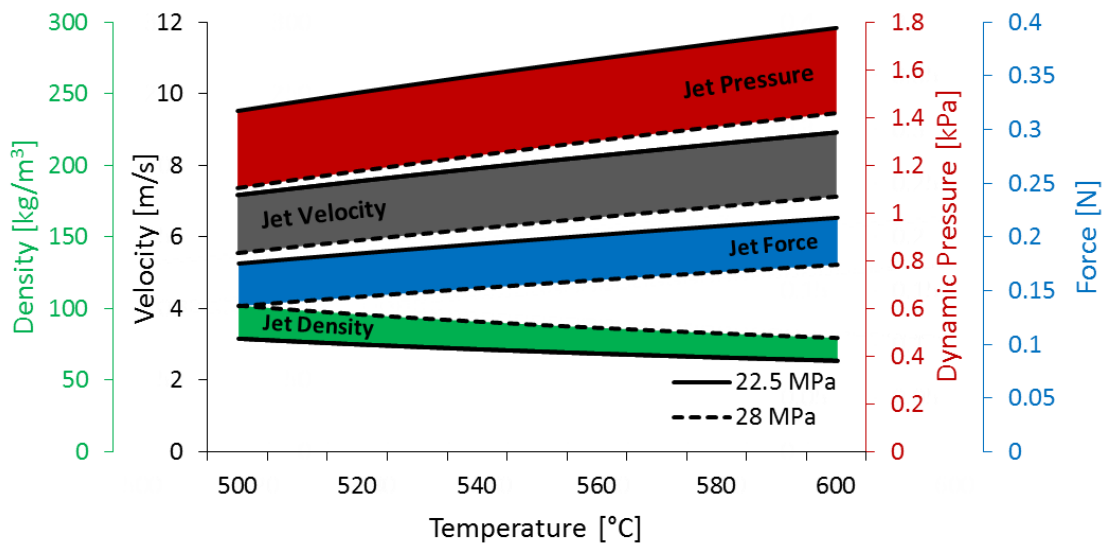


Figure 21. The range of jet nozzle velocity, and pressure difference between the jet nozzle and rock surface. The range of property values are bounded by the systems minimum and maximum experimental pressures.

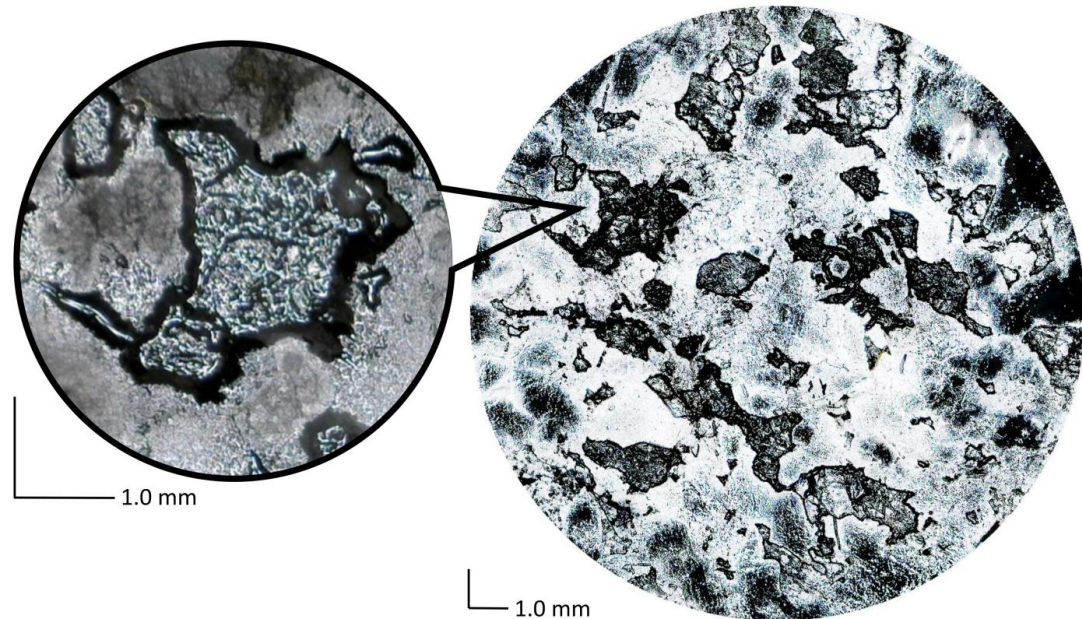
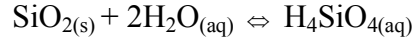


Figure 22. A close-up of a comminuted area, showing acute edges.

5.2.2. Dissolution of Quartz

Another mechanism which may remove quartz from the rock surface is dissolution.

The reversible chemical reaction for the dissolution of quartz in pure water is:



Where the forward dissolution reaction rate (Rimstidt & Barnes, 1980) (Worley, 1994):

$$r_{forward} = k_{forward} \frac{A_{surface}}{M_{water}} \left[\frac{\text{mol}}{\text{kg} * \text{s}} \right] \quad (5.1)$$

incorporates an active effective surface area, $A_{surface}$, the mass of water in the system, M_{water} , and the dissolution rate constant, $k_{forward}$. The empirical equation (regression fit) for $k_{forward}$ of quartz in pure water, based on the nominal geometric surface area is given by: (Worley, 1994)

$$k_{forward} = (276 \pm 193) \exp \left(\frac{[90.1 \pm 2.5]}{RT} \right) \left[\frac{\text{mol}}{\text{m}^2 * \text{s}} \right] \quad (5.2)$$

T is in Kelvins and R is $8.314 \times 10^{-3} \left[\frac{\text{kJ}}{\text{mol} * \text{K}} \right]$. The error limits for this equation are the 95% confidence intervals, with an estimated log $k_{forward}$ error of ± 0.63 .

First level comparison of the PWHS experimental data to Equation (5.2) indicated that the data was significantly higher than the predicted dissolution rate, see Figure 23.

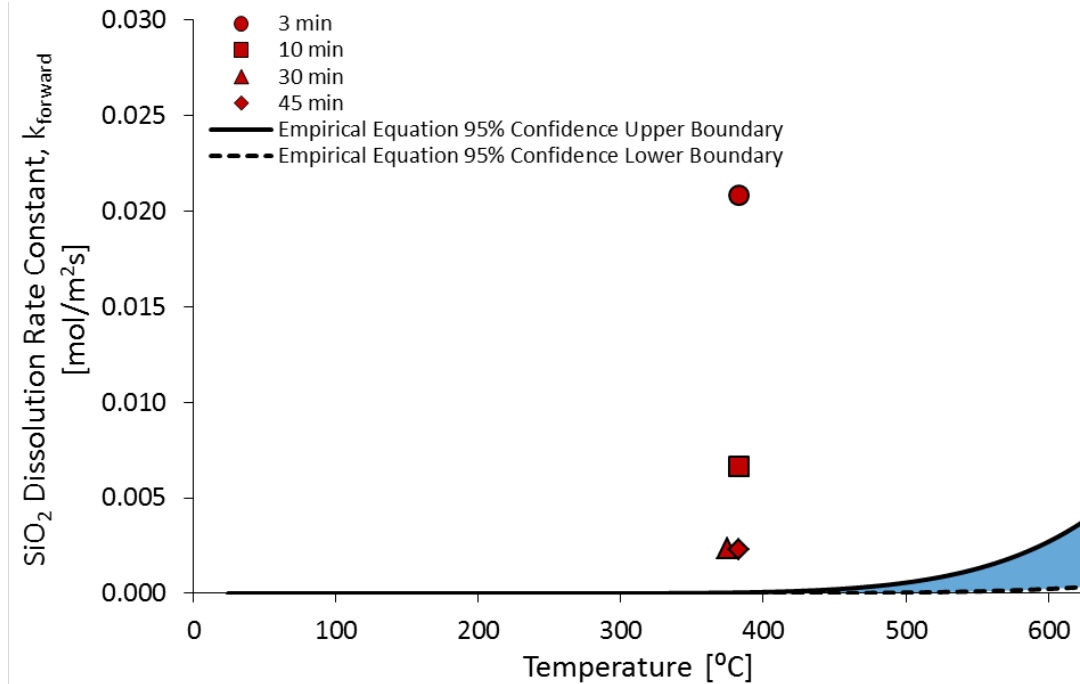


Figure 23. Calculated dissolution rate for four PWHS tests plotted against the empirical dissolution equation with 95% confidence intervals.

However, the parameters with 95% confidence levels in Equation (5.2) were fitted by linear regression to the data shown in Figure 24. This is the origin of the dissolution rate constant used to compare the removal of quartz from the comminution experiments and estimate how much quartz would be removed by dissolution alone. Calculating the dissolution rate constant for these hydrothermal comminution experiments was achieved by dividing silica's density, ρ_{solute} , by its molar mass, M_{solute} , then multiplying by the depth of the subducted area, z , and finally dividing by the duration of the experiment, t

$$k_{forward} = \frac{\rho_{solute} z}{M_{solute} t} \left[\frac{mol}{m^2 * s} \right] \quad (5.3)$$

For all tests conducted in this study $k_{forward}$ values were 1 to 2 orders of magnitude greater than indicated by Equation (5.2). It is possible that the dissolution of quartz with fresh deionized water flowing over it is faster than the quartz dissolution rate found by previous researchers who agitated the sample in deionized water, but this effect will be less than the measured $k_{forward}$. Therefore, the difference in the observed comminution rate from the quartz dissolution rate implies that a secondary mechanism preferentially removing quartz exists.

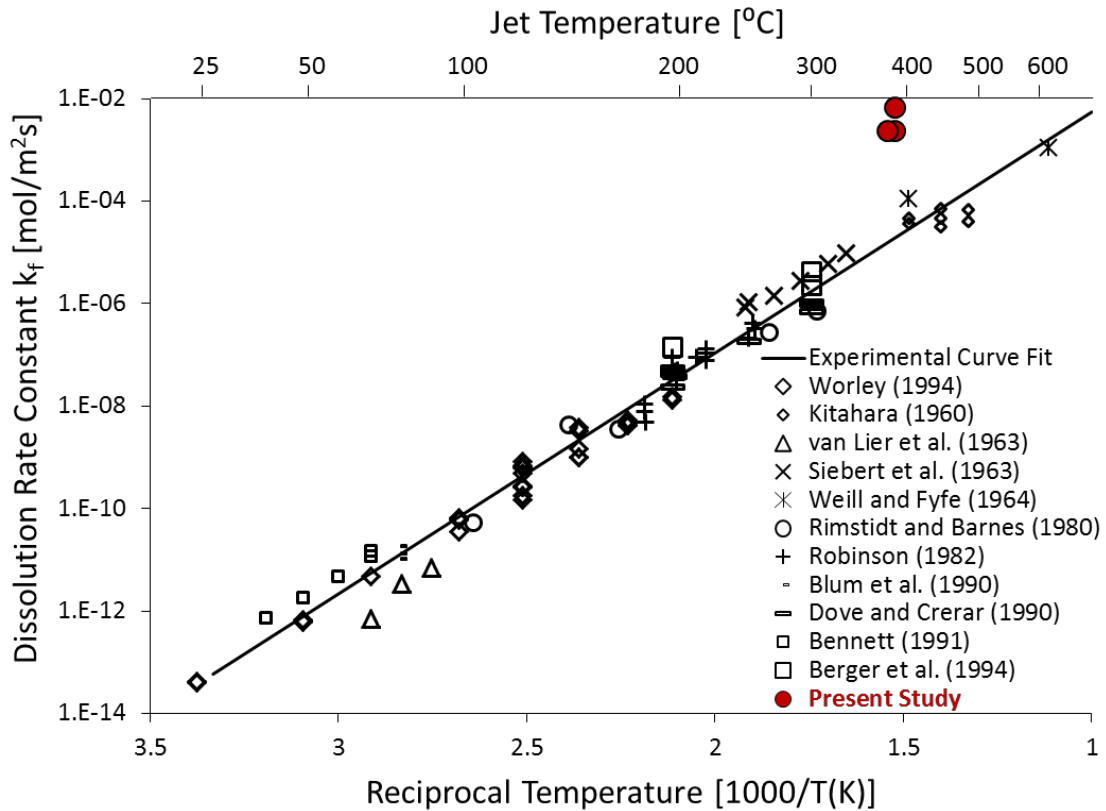


Figure 24. Arrhenius plot of pure quartz dissolution data including this study's comminution experiments (Worley, 1994). Data in Table 4, see Appendix B-1.

Further support of a secondary rate mechanism comes via visual analysis of the experiment samples, which indicates that the comminution rate was higher during the first 10 to 17 minutes of the experiment (once the rock sample has been raised into the jet) then tapers off in the latter period of the experiment as more of the exposed quartz is removed, Figure 23. This may be the result of surface damage from sample preparation increasing the rates of rock removal due to higher residual stresses near the rock surface. However, quantification of this phenomenon poses experimental challenges due to the heterogeneity of the mineral composition and grain structure of Barre Granite.

5.2.3. Microspallation of Quartz

Clearly, another mechanism other than rapid erosion and dissolution is controlling the removal of quartz. One hypothesis is that micro spallation is in fact occurring strictly within the quartz grains, but in a much more localized fashion than observed in previous open air flame jet experiments. There are several possible reasons why more localized micro spallation could be occurring under hydrothermal conditions:

- 1) The conditions achieved at the rock surface may truly be approaching the lower limit temperature and/or heat flux limit for which spallation can occur, and thus it is only in the quartz grains (with a higher coefficient of thermal expansion and higher thermal conductivity) where the induced thermal stresses are sufficient to prompt new intra-grain fracture growth. Differential thermal stresses between the grains are due to the lower thermal conductivity of the non-quartzite minerals limiting the heat transfer

along quartz grain boundaries, preferentially increasing the thermal stresses in the quartz grains.

- 2) Engineering analysis of conventional rotary drilling suggests that higher hydrostatic pressures hinder drilling rates because the comminuted material cannot be removed from the rock surface as easily. This effect may be present to some degree in PWHS as well, where, to form a spall, cracks must propagate in the plane parallel to the impinged surface, but the high hydrostatic pressure is acting to prevent crack growth along that plane.
- 3) The hydrostatic pressure generates a local tensile stress parallel to the cylindrical rock sample's top (axial) surface due to Poisson effect (Hibbler, 2016), thereby counteracting the compressive stress in this plane caused by thermal expansion which promotes spallation. The cylindrical rock sample used in these experiments has a hydrostatic pressure applied on all sides, but the compressive stress in the radial direction may diminish towards the center of the impinged top surface such that the local tensile stress component caused by the hydrostatic pressure in the axial direction is dominant.
- 4) Insufficient confining radial and axial stresses may be inhibiting continuous spallation. Successful hydrothermal spallation was achieved by Potter Drilling when they applied radial and axial stresses two and three times higher respectively than the confining hydrostatic pressure. Additionally, their rock samples had diameters four times larger than the cores used in this study (Potter Drilling, 2008) (Potter, et al., 2010).

5.2.3.1. Surface Temperature Measurements

Previous flame and laser thermal spallation research relied on surface temperature data and heat flux measurements to plot their experimental results. Therefore, PWHS surface temperature measurements were essential in producing a definitive comparison between high density hydrothermal spallation and low density flame jet spallation methods.

The temperature of the top surface of the rock sample directly under the hot water jet is different than the temperature of the hot water jet exiting the nozzle (1.2mm displacement between jet nozzle and rock surface). This temperature difference, ΔT , can be attributed to the axial and radial thermal gradient in the rock. Where the side circumferential area of the cylindrical experimental rock sample is assumed to be close to the temperature of the cooling water jacket, in which it is immersed, while the top surface is much hotter since it is directly exposed to the high temperature hydrothermal jet.

Quantifying the surface temperature of the rock sample is essential to predict spallation (Wilkinson & Tester, 1993). Previous flame and laser spallation research by Rauenzhan, Wilkinson, Augustine, and Rothenfluh relied on surface temperature data to plot and compare their experimental results (Rauenzhan, 1986) (Wilkinson & Tester, 1993) (Wilkinson, 1989) (Augustine, 2009) (Rothenfluh, 2013). However, the design of this study's pressure vessel could not accommodate any external devices to

measure rock surface temperature; therefore, an alternative method of surface temperature measurement was designed and implemented.

To measure the surface temperature a rock sample was cored from the underside until only a very thin layer of rock, 0.65mm, remained at the top surface, see Figure 25. The ratio of diameter of the cored out section to top cap thickness was 10:1 allowing the assumption of horizontal isotherms, and vertical heat flow at the centerpoint. A 1/16" (1.6 mm) thermocouple stripped of its shielding (mitigating conduction losses) was placed in contact with the underside of the thin top cap, the remaining chamber volume was filled with thermal conductive paste and sealed with a rubber diaphragm. The actual surface temperature will be slightly higher than the measured surface temperature due to the contact resistance of the thermocouple and thermal resistivity of the granite. However, these factors were not included in the surface temperature analysis because of the minimal thickness of the top cap, and the short 1.8 mm distance between the jet and surface temperature thermocouples. Each of the surface temperature measurements were averaged over a greater than 30 second "steady state" period during which the temperature did not fluctuate by more than one degree.

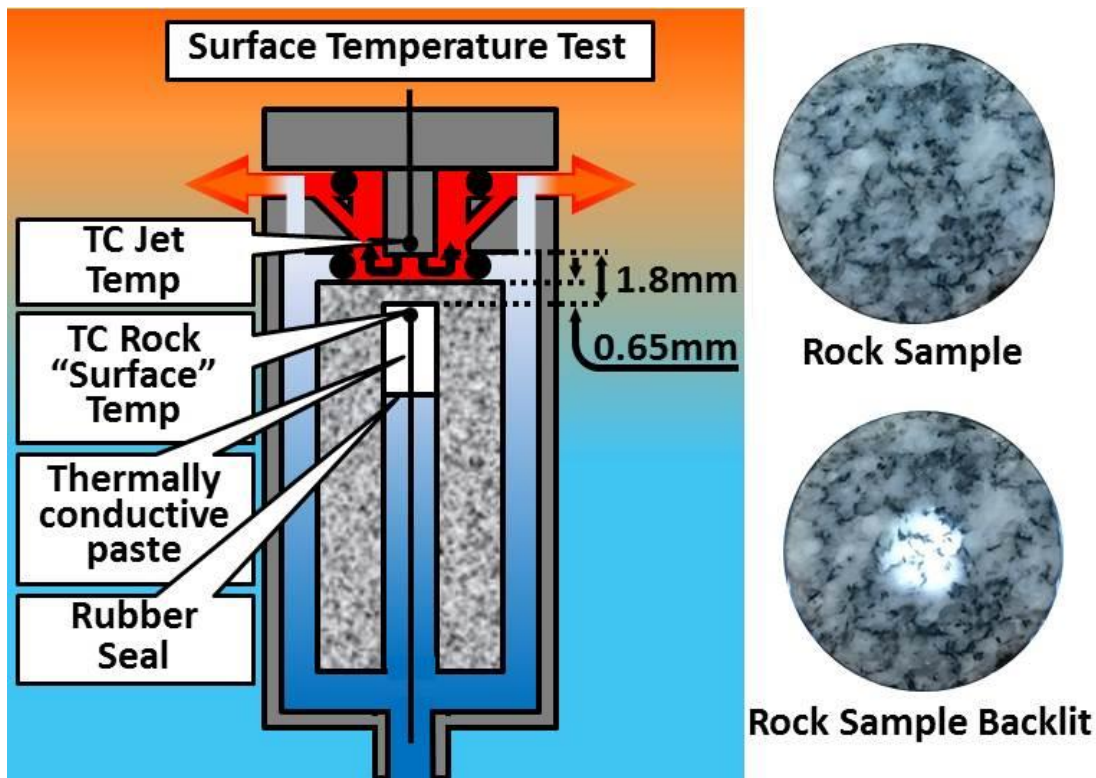


Figure 25. The distance between the two thermocouples measuring jet and surface temperature was 1.8mm. Backlighting the rock sample shows the transparency of the 0.65 mm thick granite “cap”.

The measurements indicated that the temperature in the rock layer near the surface of the granite rock sample that was undergoing comminution was lower than the impinging supercritical water jet. And the ΔT between the surface of the rock and hot water jet increased as the temperature of the jet increased, as shown in Figure 26. Regression analysis of rock surface temperature was plotted as a power curve, and two linear lines that intersect roughly near the critical temperature of 374°C . The segmented linear trendlines in Figure 26 illustrate the impact of the distinct change in fluid properties due to the transition from subcritical to supercritical conditions.

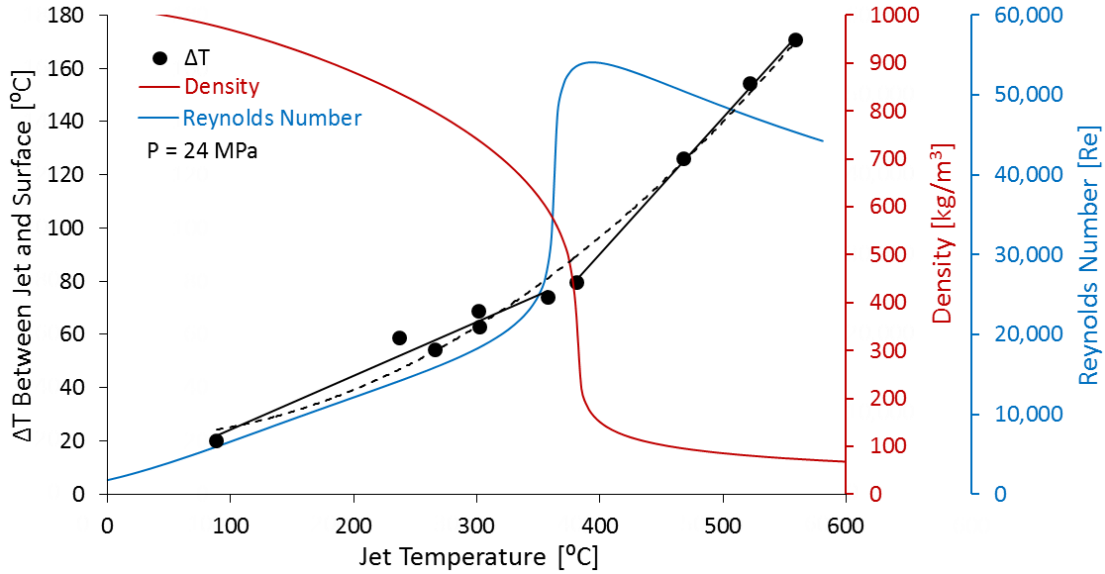


Figure 26. Estimated temperature difference, ΔT , between the surface of the rock and the hydrothermal jet as a function of the hydrothermal jet temperature at 24 MPa. The data points represent steady state temperature measurements. The dashed trendline is a best fit regression of the data, and the two linear trendlines are regression analyses that intersect at the supercritical point. Data in Table 5, see Appendix B-1.

The increasing rate of increase in ΔT as the jet temperature increases is due to significant changes in fluid properties which affect the heat transfer to the rock surface. The water jet is transforming from a high density liquid (982 kg/m^3) to a low density supercritical fluid (72 kg/m^3). This decreasing density changes the fluid velocity, V , from a slower 0.5 m/s up to 7 m/s , which in turn increases the Reynolds number ($Re = \frac{VD}{\nu}$) from 4000 (close to the onset of turbulence in a closed tube) to over $50,000$ (note that the kinematic viscosity, ν , only changes by 21.8% in this region) implying that the effectiveness of the fluid to transfer its heat to the rock is decreasing as the convective fluid velocity increases. This reduction in heat transfer can be observed in the slope of the segmented linear trendlines. The sub-critical slope

is 0.2 while the supercritical slope is 0.52, indicating that the sub-critical fluid is 2.6 times more effective at communicating heat to the rock face than the supercritical.

Other researchers have identified large ΔT 's. For example, Kant using a high sampling rate pyrometer (1000 Hz) to quantify spallation temperatures cites ΔT 's of 858-939°C, between an impinging gas flame jet (1100-1450°C) and a spalling rock surface in the temperature range of 500-511°C for Bethel and Gothard Granite (Kant & Rudolf von Rohr, 2016). Potter Drilling identified a minimum hydrothermal jet temperature of 700°C to prompt spallation (Potter Drilling, 2008). Extrapolating a surface temperature for Potter Drilling using this study's surface temperature data implies a surface temperature of ~460°C, which corresponds to a ΔT of 240°C. Potter Drilling's ΔT for the onset PWHS was only 25-28% of the ΔT found for continuous gas flame jet spallation. Implying that the hydrothermal jets used in PWHS are significantly more effective at transferring heat to the rock surface than lower density flame jets at much higher temperature. We conclude that only quartz was thermally spalled and the other grains were not, because the critical ΔT for spallation was just reached for quartz but not reached for the other minerals with lower thermal expansion coefficients.

5.2.3.2. Heat Flux Experiments

Heat flux measurements for PWHS were essential in the comparison of this hydrothermal spallation research to previous flame jet and laser spallation data. The heat flux experiments performed were based on the energy balance

$$\dot{q}_{heat\ flux} = \dot{q}_{in} - \dot{q}_{exit\ H_2O} = \frac{\dot{m}\Delta h}{A} \quad (5.4)$$

where \dot{q} has units of $\frac{W}{m^2}$. \dot{m} , Δh , and A are: mass flow rate, change in enthalpy between the incoming and effluent water, and surface area respectively. As such a standard rock sample was cored from the top to create a cylindrical chamber with side walls and base of equal thickness ($5.5 \pm 0.3\text{mm}$). The area hollowed out is the downward projection of the top area exposed to the hydrothermal jet in comminution tests, providing an approximation of the PWHS experimental configuration. Two thermocouples were placed at equal height, one within the incoming jet the other in the exit water. The height positioning of both thermocouples was determined by a 1:5 ratio of the annular width (between the incoming jet stem and sample's side wall) to the top edge of the rock sample, mitigating the edge effects of increased heat loss from the top metal portion of the reactor, Figure 27. The confining pressure and temperature difference between the two thermocouples was used to calculate the Δh of pure water using thermodynamic properties for pure water from NIST (NIST REFPROP, 2013). System cooling water flow rates were varied from the experimental standard of 2.8 LPM to see the impact they had on heat flux; the lower flow rate experiments of 1.8 LPM were cut short due to the pressure vessel exceeding the maximum temperature of 80°C .

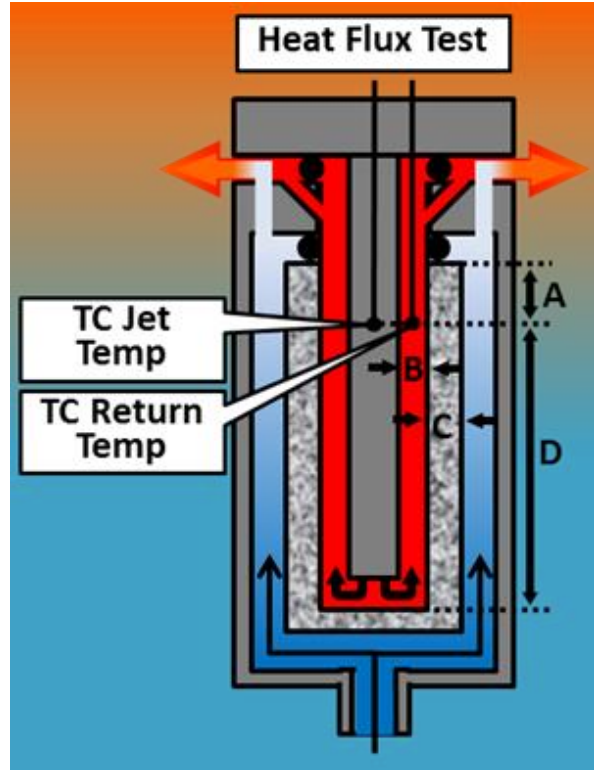


Figure 27. Experimental configuration for the heat flux tests. To mitigate edge effects the ratio of A:B was 5:1, D:A 5:1, C:D 19:1.

The rock surface temperature used to plot the heat flux results was directly based on the surface temperature experiments from Chapter 5.2.3.1 with +20°C added. This increase in surface temperature was due to 20°C being subtracted from the ΔT correlation to align the jet and surface temperatures, see Figure 28. This ΔT correction was accepted for three reasons:

- 1) Both the jet and surface temperatures have to be equal in the ~20°C feed-water temperature range, and this point of intersection could not be extrapolated from the regression analysis of the measured ΔT .

- 2) The tangent of the Nusselt number, Nu, curve (ratio of convection to pure conduction) was virtually horizontal in the compressed water region (Figure 28), implying that the heat transfer coefficient was almost constant. The density of the water was high and the Reynolds number low implying that the surface temperature of the rock in the $<100^{\circ}\text{C}$ temperature range should be close to the temperature of the impinging jet.
- 3) When the experimental heat flux data were plotted against the corrected surface temperature its maximum corresponded very well to the critical temperature of water at 24MPa where the specific heat is a maximum.

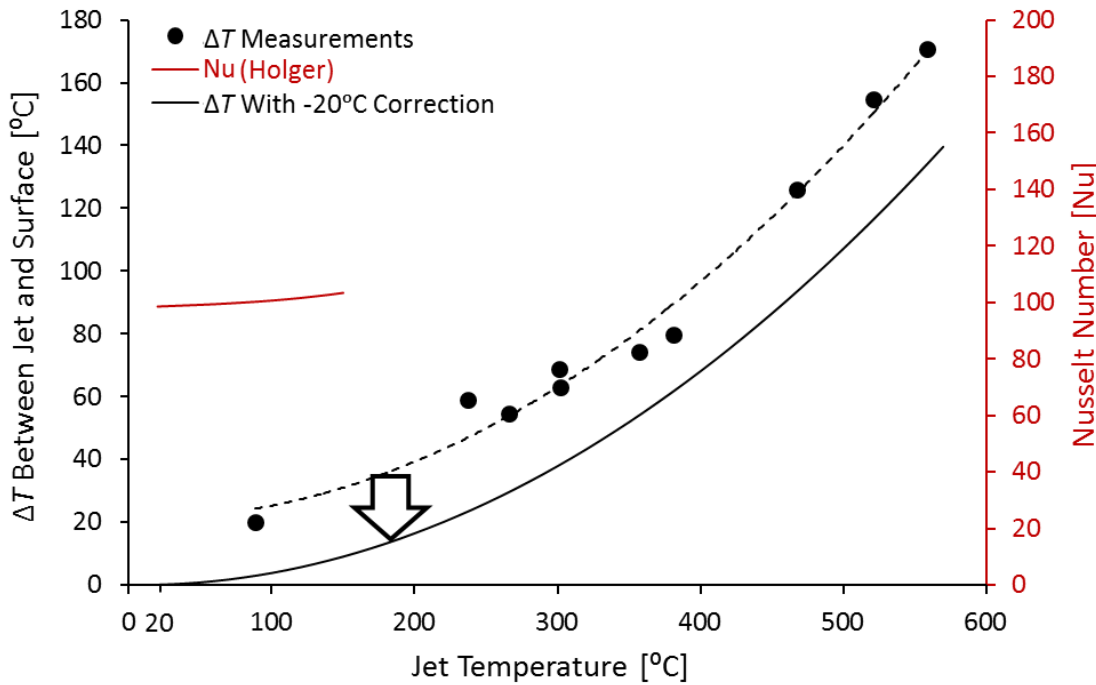


Figure 28. ΔT correlation lowered by 20°C , increasing the rock surface temperature by 20°C . Reasons: slope change of the Nusselt number is minor, water density is high, and the Reynolds number low in the $<100^{\circ}\text{C}$ region.

Correlating the experimental heat flux data to the rock surface temperature indicates that heat flux through the rock increases up to around the critical point and then drops off rapidly, Figure 29. This experimental result is consistent with water's combined thermodynamic properties of density and specific heat, volumetric specific heat [W/m³K], as seen in Figure 29. Because the change in specific heat varies the energy available for transfer in the fluid while the drop in water density limits the transfer of that heat to the rock. It should be noted that while the thermal diffusivity $\left(\frac{k}{\rho C_p}\right)$ of water dips at the critical point the ratio of the diffusivity and volumetric specific heat, which is the Prandtl number also peaks at the critical point, see Figure 30. The differences in the slope of the experimental heat flux lines in Figure 29 correspond to different cooling water flow rates that surround the exterior of the rock sample. As the cooling water flow rate increases it extracts more energy, increasing the heat flux from the hydrothermal jet to the rock. Additionally heat conduction through the rock, $\dot{Q} = -kA \frac{dT}{dx}$, is limited by the rock thermal conductivity, k . As shown in Figure 29, k for Barre Granite is inversely related to temperature (Hueze, 1983). The decreasing thermal conductivity increases the axial temperature gradient linearly as the temperature increases for the same imposed heat flux.

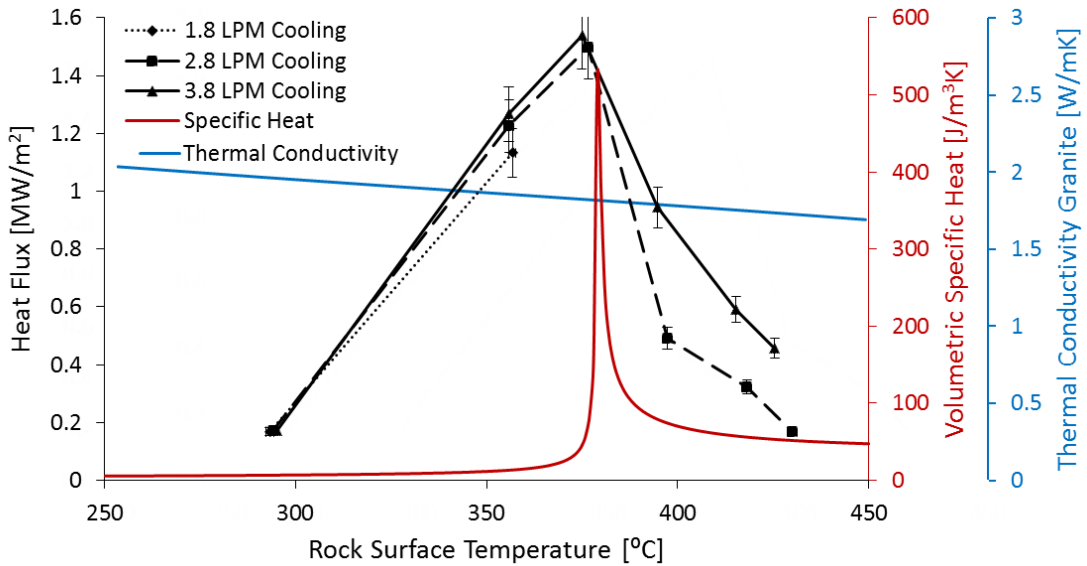


Figure 29. Heat flux as a function of experimentally determined rock surface temperature. The ratios of supercritical jet flow to the cooling water flow rates of 1.8, 2.8 and 3.8 liters per minute, LPM, were 1:7.5, 1:11.5, 1:15.8, respectively. The volumetric specific heat of water, and thermal conductivity of granite at a pressure at 24 MPa were calculated using the experimentally determined rock surface temperature. Data in Table 6, see Appendix B-1.

5.2.3.3. Comparison of Heat Flux Data to Correlations

Previous heat flux research for impinging gas and liquid jets in open and closed environments were compared to this study's measurements to serve as an independent reference check. However, in this study's experimental configuration only the bottom 5% of the internal surface area was directly exposed to an impinging jet. The internal side walls accounting for 95% of surface area had two different temperature interfaces: the inner wall acting as a counter-flow heat exchanger, the external wall a parallel flow heat exchanger. Since an impinging jet has a significantly higher heat transfer coefficient than convecting flow in a concentric tube annulus, for the same

conditions, it was assumed that the PWHS experimental heat flux values would be lower than the correlations for impinging jets. Additional differences in experimental results were anticipated because most of the experimental configurations in published research on gas and liquid impinging jets are inverse to Cornell's PWHS set up, their impinging jets served to cool the flat heated surface (Chang, et al., 1995); (Garimella & Rice, 1995); (Martin, 1977).

Some of the available research was not plotted due to significant differences in temperature, impinging jet to rock surface standoff distances and Reynolds number. The plate temperature in Mohanty and Tawfek's work was 9.8°C above ambient with a stand off distance 27 times greater than this research, and was based on experimental Reynolds numbers 30% less than this study's minimum (Mohanty & Tawfek, 1993). Lytle and Webb had a good stand off distance, but their jet temperature coming off the heating plate was only 9-12°C higher than ambient air (Lytle & Webb, 1994). Hydrothermal flame jet heat flux research by Tobias Rothenfluh, Martin J. Schuler, and Philipp Rudolf von Rohr from ETH Zurich was considered but not used (Rothenfluh, et al., 2013). This was because their experimental correlations required this research to make a significant number of assumptions regarding the data, which resulted in a curve fitting operation rather than an experimental comparison.

Heat flux was calculated using $\dot{q} = \bar{h}\Delta T$ where \dot{q} is heat flux in units of $\frac{MW}{m^2}$, \bar{h} is the average convective heat transfer coefficient $\left[\frac{MW}{m^2 K}\right]$, and ΔT is the temperature difference between the impinging jet and the experimental surface temperature

measurements. $\bar{h} = \frac{\bar{Nu}k}{D}$ where \bar{Nu} is the average dimensionless Nusselt number over the rock surface describing the ratio of conduction to convection, k is the thermal conductivity of the fluid $\left[\frac{MW}{mK}\right]$, and D is the internal diameter of the jet nozzle in meters. Since the Reynolds and Prandtl numbers are used to estimate Nusselt numbers, for the heat flux correlations they have been plotted over the experimental range of jet temperatures in Figure 30 to provide a reference for understanding the correlations.

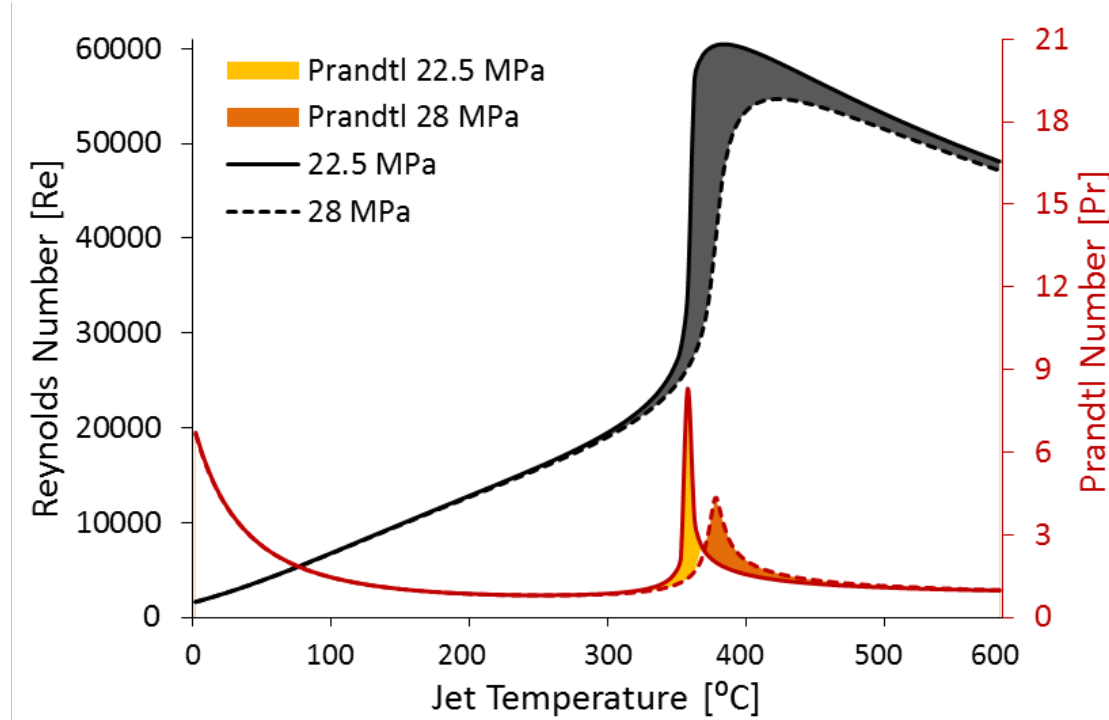


Figure 30. Reynolds and Prandtl numbers for the range of experimental temperatures and pressures, assuming pure water properties.

\bar{Nu} and \bar{h} were calculated using research by Schlünder and Gnielinski for gas jets impinging on a solid surface, their results were summarized by H. Martin (Martin, 1977), The Martin correlation used was:

$$\overline{Nu} = 1.3482 Re^{0.4744} Pr^{0.42} \quad (5.5)$$

Re is Reynolds number, the dimensionless ratio of inertial to viscous forces. Pr the Prandtl number, a dimensionless ratio of momentum to thermal diffusivities. Equation (5.5) includes a correction factor, k' , for adjusting the ratio of jet stand off distance, Z , to the diameter of the impinging jet, D . In this case $k' = 0.99$ for this system's $\frac{Z}{D} = 0.37$. The heat flux correlation can be seen compared to the experimental data in Figure 31.

Garimella and Rice published research for confined and submerged impinging liquid jets, however their impinging jet temperature was only 20°C with stand off distances four times greater than in this study, and a Reynolds number 52% less than this studies' minimum (Garimella & Rice, 1995) (Rice & Garimella, 1994). However, their correlations were included because Rothenfluh's hydrothermal jet experimental results (ETH Zurich) compared closely to Garimella's correlation

$$\overline{Nu} = 0.492 Re^{0.585} Pr^{0.4} \left(\frac{Z}{D}\right)^{0.024} \left(\frac{l}{D}\right)^{-0.09} \quad (5.6)$$

Where $\frac{Z}{D} = 0.37$, and $\frac{l}{D}$ is the jet nozzle aspect ratio, which was set to one for this correlation based on Garimella's statement "*the heat transfer coefficients were shown ... to be only weak functions of nozzle aspect ratio in this $\frac{l}{D} \geq 1$ range*" (Garimella & Rice, 1995). Garimella's correlations compared closely to Martin's, see Figure 31.

Chang's impinging fluid jet research was limited to heated plate surface temperatures of less than 79°C with jet stand off distances four times greater than Cornell's system; however, the Reynolds number associated with the experimental results was in an applicable range so it was included (Chang, et al., 1995).

$$\overline{Nu} = 0.660 Re^{0.574} Pr^{0.4} \left(\frac{Z}{D} \right)^{-0.106} \left(1 + 0.1147 \left(\frac{r}{D} \right)^{1.81} \right)^{-1} \quad (5.7)$$

The ratio, $\frac{r}{D}$, of radius, r , from the axial center of the jet to the jet diameter, D , is zero since the thermocouple in the surface temperature experiments was located at $r = 0$. Chang's results were 33 and 27 percent higher than Martin and Garimella respectively. It should be noted that neither Martin, Garimella, or Chang discussed impinging jet behavior in near critical and supercritical region, therefore their correlations may not be applicable at temperatures above ~370°C.

Augustine's research into heat flux for hydrothermal flame jets is also included in Figure 31 (Augustine, 2009). His data was plotted as two data points because Augustine varied the flow rate of the impinging jet in his experiments so there were only two points when the momentum flux $\left[\frac{kg \cdot m}{s^2} \right]$ of his research intersected with this work.

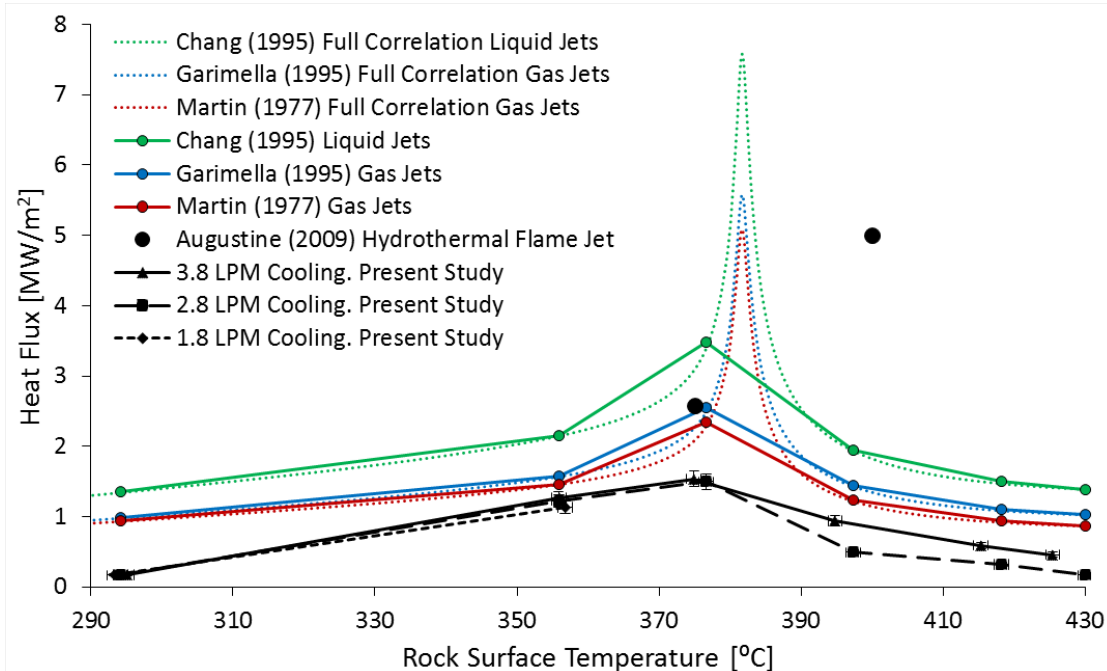


Figure 31. Comparison of experimental heat flux results to published heat flux correlations for impinging jets.

The comparison of the experimental PWHS heat flux data to impinging jet correlations indicated that the general trends of the heat flux lines corresponded well to the results of this study (black). However, the correlations' heat flux values were – at the minimum 19, 28, and 75 percent higher and at the maximum 440, 510, and 730 percent higher than the 2.8 LPM experimental data for the correlations from Martin, Garimella, and Chang respectively. Augustine's heat flux values were 72 and ~1000 percent higher than observed in this study, but there are difficulties in making a definitive comparison between Augustine's hydrothermal flame experiments and this research. Differences in the experimental results and published heat flux correlations were expected due to dissimilar experimental configurations, and did not appear to

impact the relevance of the heat flux data gathered for this study's PWHS experiments.

5.3. Comparison of Hydrothermal to Flame and Laser Spallation

The experimentally determined surface temperature and heat flux data were used to compare the PWHS results to previous experimental work in flame jet and laser spallation at low pressures and densities on Barre Granite (Rauenzahn, 1986) (Wilkinson, 1989). See Figure 32.

All of the experimental data from this study were below the temperature of previous thermal spallation experiments. The heat fluxes were also near or below the lowest values measured for flame or laser induced spallation. Therefore, while the relationship between surface temperature and heat flux is not fully understood there appears to be a threshold temperature/heat flux that must be reached to induce true thermal spallation (Kant & Rudolf von Rohr, 2016). Potter Drilling identified the onset of PWHS at a water jet temperature of 700°C (Potter Drilling, 2008). This is ~100°C higher than the maximum jet temperature possible for the PWHS drilling apparatus at Cornell. Therefore, continuous PWHS could not be achieved at the higher temperatures and heat fluxes needed using the existing equipment. However, since the PWHS experiments were close to the spallation threshold chemical additives were introduced into the system to see if they could induce sufficient weakening of the rock matrix to prompt spallation.

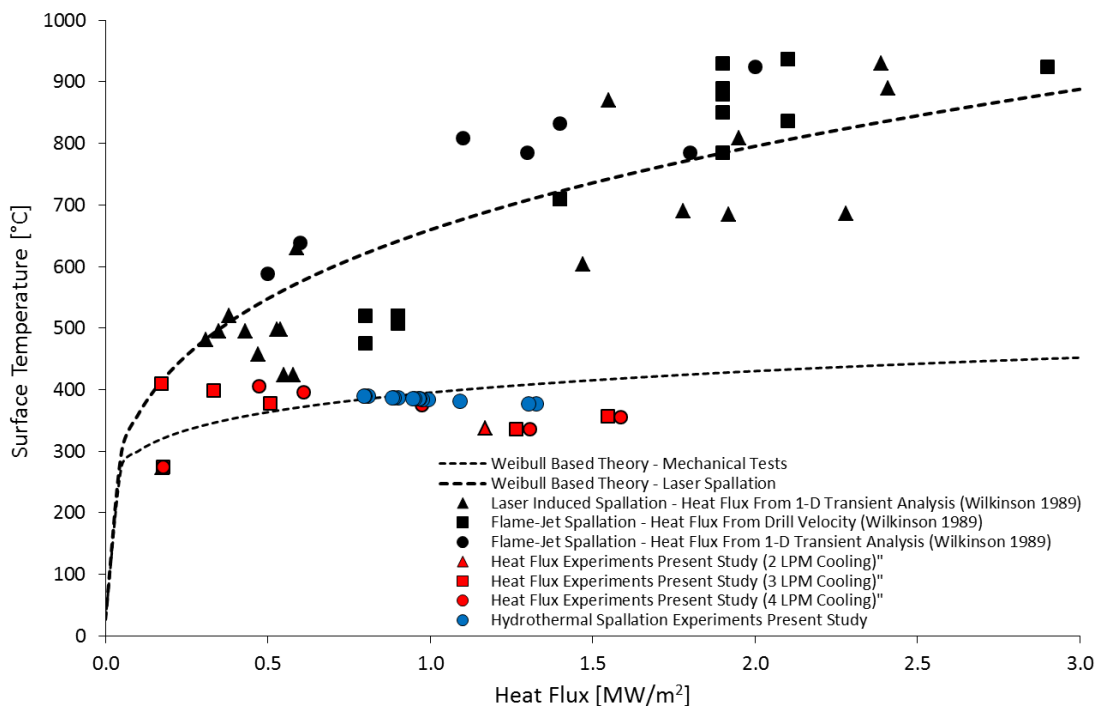


Figure 32. Experimentally determined heat flux and surface temperature for hydrothermal jet spallation compared to flame jet and laser spallation. This study's hydrothermal experiments were conducted at surface temperatures below previous experimentally determined thresholds for gas immersed spallation. Data can be found in Table 7, see Appendix B-1.

Chapter 6. CHEMICALLY ENHANCED HYDROTHERMAL SPALLATION LITERATURE REVIEW

Chemically enhanced hydrothermal spallation (CEHS) involves the addition of aggressive chemicals into the impinging supercritical water jet stream to promote thermal spallation by weakening the rock's surface. This enables higher rates of rock removal at lower jet temperatures. Some of the previous research into chemically enhanced drilling is discussed below.

6.1. An Early Historical Experiment

In 218 BC Hannibal Barca crossed the Alps in the Second Punic War to attack Rome (Lazenby, 1978). To accomplish this feat he apparently relied on chemical enhanced thermal dissolution/spallation. While descending the Alps into Northern Italy Hannibal's path was blocked by large boulders. He solved this problem by setting large fires around the boulders and then quenching them with sour wine when they were very hot. Using this combination of heat and chemistry the Carthaginians broke through the rocks so the elephants could pass, enabling the invasion of Italy (Livy, ~27 BC). Presumably, it was the acetic acid content in the sour wine that attacked the carbonate minerals in the boulders making the rock more susceptible to fracture when heated.

6.1. Recent Work

Lab scale research into chemical drilling by McCoulough bored through sandstone and granite using an undisclosed concentration of a halogen fluoride passed over catalyst to generate a high velocity, highly reactive chemical stream. A conceptual diagram of this system can be seen in Figure 33 (Ledgerwood, 1960). The actual implementation of this method requires frequent drill string tripping, and explosive charges. W. C. Maurer in a review of this particular technology commented that “*The chemical drill appears to have little application for large-scale rock drilling because of the high chemical costs and because of the difficulty in handling large volumes of highly reactive chemicals.*” (Maurer, 1968).

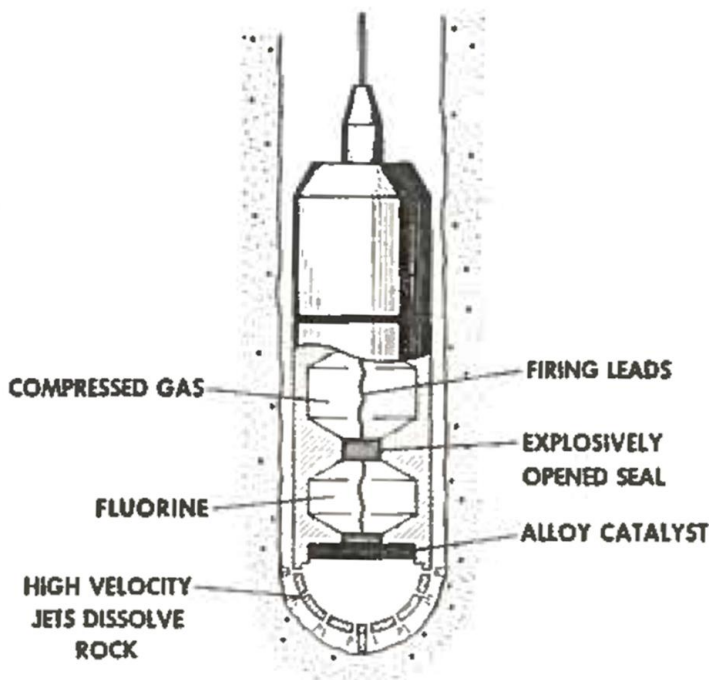


Figure 33. Conceptual diagram of the McCoulough chemical drill (Ledgerwood, 1960).

Some techniques for chemical drilling use acids. A white paper on a drill head called Hydratherm claims to alternately pulse a high temperature gas flame jet with ultra high pressure rotary ethanoic acid jets (North, et al., 2001). The inventors state that this combination of spallation and quenching followed by dissolution and erosion can drill at speeds greater than 51m/hr. However, this drilling concept does not appear to have become commercially successful, as there are no reports of its use, or even the existence of the company other than this white paper.

Another acid drilling method was proposed in 2004 by Philip Rae and colleagues, on the behalf of BJ Services Company, who received a U.S. patent for drilling using hydrochloric, formic, nitric, and acetic acid (Rae, et al., 2004). However, the purpose of this patent appears to be acquiring the largest amount of intellectual space rather than specifically protecting a new drilling apparatus because of broad terms like: “*The chemicals can be any chemical that dissolves rock at a rate sufficient for production of the wellbore... preferably in a controlled manner.*”, “*The wellbore...might form a long small diameter hole, or multiple short, lateral drainage channels originating in a main borehole ... at one or several depths.*”, or, “*The pressure at the nozzle can generally be any pressure effective to provide an acceptable rate of progression*”, and “*The nozzle can generally be any type of nozzle...any shape...nozzle hole diameter can generally be any size.*”. The patent diagrams in Figure 34 are also equally ambiguous leaving virtually all details undisclosed.

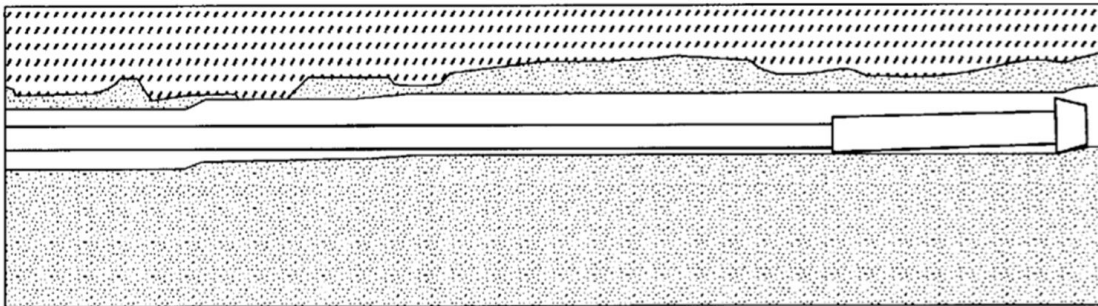


FIG. 1

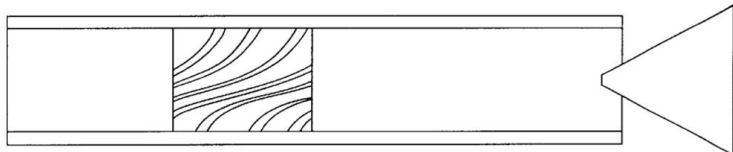


FIG. 3

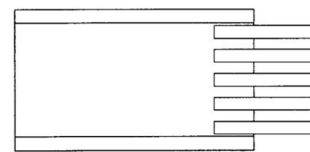


FIG. 5

Figure 34. Diagram of the BJ Services Company acid drilling operation. Fig 1.
“Example assembly”, Fig 3. “Swirl inducer... can result in conical jet”, Fig 5.
“Many individual nozzles can be used to cover entire borehole”. (Rae, et al., 2004)

In 2004, the late Richard S. Polizzotti from ExxonMobil claimed sodium hydroxide, NaOH, enhanced hydrothermal spallation rates of 3.78m/hr at a temperature of 800°C in U.S. Patent 6,742,603 (Polizzotti, 2004). Patent claims b, c, and d describe the chemical process of interest, and Figure 35 is a system diagram.

“b) Introducing into the top end of the fluid conduit an aqueous fluid comprising water and hydroxides of Group I elements of The Periodic Table of Elements and mixtures thereof.”

“c) Heating said aqueous fluid to temperatures in the range of 500° C. to 1400° C. to provide a heated aqueous fluid.”

"d) Discharging from the lower end of the fluid conduit the heated aqueous fluid to contact the rock of the subsurface formation and effect dissolution of the rock therefrom."

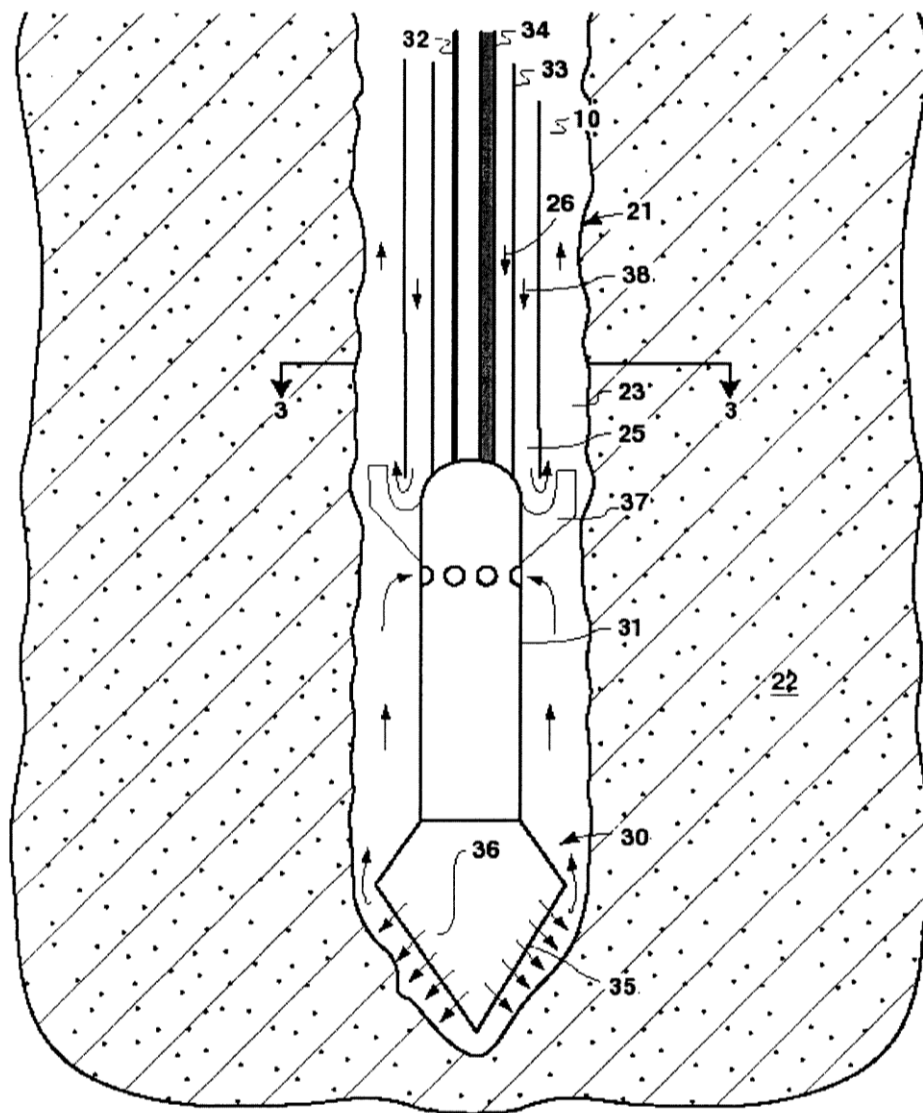


Figure 35. "...an enlarged schematic representation, partly cross-sectional, of a second embodiment of a hydrothermal drilling system that uses chemical reaction to produce hot drilling fluid in a borehole." (Polizzotti, 2004).

The patent builds on b, c, and d claiming that concentrations of 0.025mol NaOH per kg of water at temperatures greater than 500°C can “*achieve commercially viable formation penetration rates*”. These claims and spallation rate are of particular interest because the spallation rate itself is quite high and yet neither the methods nor the approach were explicitly published for proprietary reasons. However, Polizzotti’s claims are consistent with earlier reports that higher pH in caustic solution has been shown to increase quartz dissolution rates (Worley, et al., 1996).

Chapter 7. CHEMICALLY ENHANCED HYDROTHERMAL SPALLATION EXPERIMENTS

This part of the hydrothermal spallation investigation focuses on evaluating CEHS under defined conditions to quantitatively measure and model the effect of jet temperature and NaOH concentration on rock removal rates. This study replicated the lower temperature limits claimed in the Pollizzotti patent to ascertain if they would lead to enhanced rates of rock penetration over the pure water hydrothermal jet spallation rates.

7.1. Modifications to Experimental Apparatus and Conditions

The same experimental apparatus used for the PWHS tests was used for the CEHS tests. The primary difference to the experimental configuration was the coaxial injection of pre-heated NaOH into the supercritical water jet stream. The mixing distance for the two fluid streams was limited by space and corrosion constraints to the 25 mm long, 3.25 mm internal diameter, Inconel Alloy 625 jet nozzle. This distance was deemed sufficient because the supercritical water in the jet was very turbulent ($Re \sim 50,000$) and the $\sim 8:1$ ratio of tube length to internal diameter was deemed sufficiently close to the 10:1 ratio for fully developed flow in an enclosed tube (White, 2011).

Coaxially injecting NaOH into the jet required replacing the internal jet thermocouple, which measured jet temperature, with a 1.59mm (1/16") tube to deliver the NaOH solution. This necessitated relocating the internal jet thermocouple to the outside of the jet as seen in Figure 36. Because of this change the thermocouple was exposed to the cooler fluid returning from the rock face; therefore, the thermocouple no longer measured the actual jet temperature. This temperature difference became more pronounced as the rock face eroded decreasing the stability and precision of the measurements. Since no other viable locations improved the measurement accuracy a series of calibration tests were performed to generate correlations between the heater temperature, actual jet temperature, external jet temperature, and rock surface temperature, see Figure 37. However, these correlations were made using pure water injected through the 1.59mm tube and not the NaOH solution. Furthermore, this represented an ideal condition when the rock face was not eroding; therefore, using these temperature correlations to make inferences about unmeasured temperatures increases the uncertainty of the temperature values by ~2% full scale as seen in Figure 37.

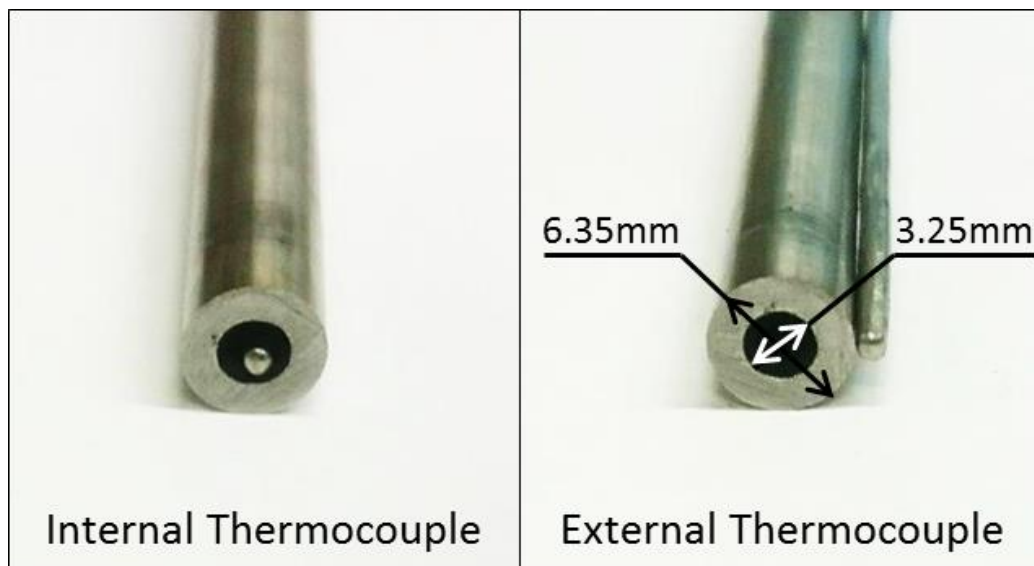


Figure 36. Thermocouple moved from inside the hydrothermal jet nozzle to outside. It was replaced inside the tube by a 1.59mm (1/16") tube to deliver NaOH.

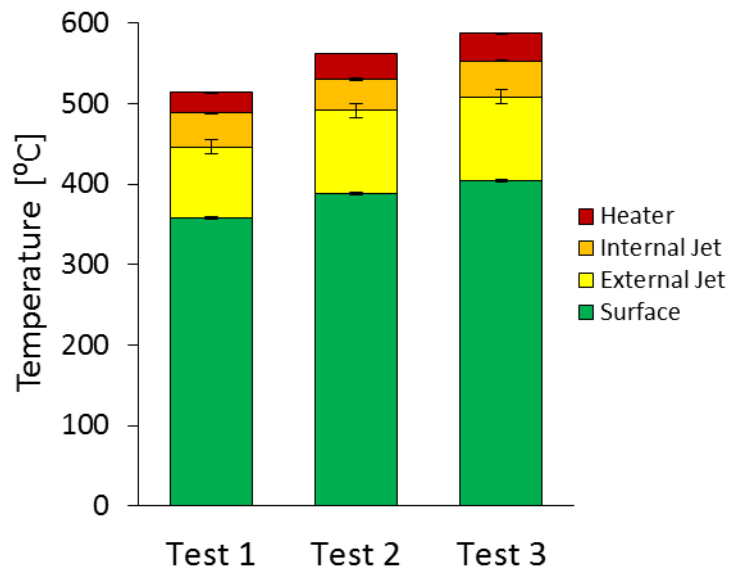


Figure 37. Temperature correlation tests made at increasing temperatures to quantify the ΔT between the heater, internal jet, external jet and surface temperatures. The measured error associated with the external jet temperature measurements was $\sim \pm 2\%$ full scale.

The mass flow rate of the injected 50% w/w NaOH solution (25 molal) NaOH was measured in two different ways for the 21 CEHS experiments. The most accurate method was used on the final twelve CEHS experiments, where the NaOH container was weighed before and after the experiment and then the loss in mass was divided by the duration of the injection time. It is assumed that the first nine experiments had the same mass flow rate even though the measurement process was different, and could have resulted in small measurement differences. In the first nine experiments, the mass of NaOH injected over one minute was measured for each of the five experimental flow rates; however, these measurements were only taken when the system was not heated or pressurized. After completing the first nine tests the configuration of NaOH injection delivery system was changed to correct for frequent system failure. To compensate for the change the new system configuration was recalibrated to output the same mass flow rate (as the first nine experiments) over one minute of operation, at ambient temperature and pressure. This *calibrated* flow rate was used in the final twelve tests. Despite the experimental continuity, some possible sources of error are: the length of the injection tubing used in the initial configuration was 20 ft (6.096m) longer, and heated during testing so the mass flow rate may have increased when the tube was heated due to a drop in NaOH viscosity. However, the difference in pressure drop between the two piping configurations (higher loss for first configuration) was only about 0.34 MPa (50 psi, or ~1.4% full scale), and the final system temperature and pressure was the same for both sets of experiments.

The high pressure chemical pump requires 15-25 seconds to come to full system pressure during which time no solution is injected, and the system control software did

not allow a user to view certain combinations of pressure readings during operation. Therefore, due to the software bug the exact start of the injection time could not be precisely determined for each test. The system workaround was allowing the chemical injection pump to run for 10 minutes and 30 seconds each test to ensure a full 10 minutes of NaOH injection.

The O-ring separating the top face of the rock (exposed to the supercritical jet) from the cooling water jacket eroded in most CEHS experiments; however, the degree of erosion was crucial to determining a successful experiment, see Figure 38. In three experiments the O-ring partially failed, dropping the temperature of the solvent impinging on the rock surface. For these three experiments the dissolution data was *corrected* to more closely represent the *actual* dissolution rate. The method of correction was time weighting the mass of granite removed during the experiment, $M_{measured}$, with a known mass of granite removed during a successful experiment at the lower temperature, $M_{T_{lower}}$. The ten minute experimental run time, t_{total} , was divided into two sections of time, one associated with the higher temperature region $t_{T_{higher}}$, and the other with the lower temperature region, $t_{T_{lower}}$. This allows for an interpolation of a *corrected* mass removed, $M_{corrected}$. The higher and lower temperature/dissolution regions can be seen in Figure 38.

$$M_{corrected} = \frac{t_{total}}{t_{higher}} \left(M_{measured} - \left(\frac{t_{lower}}{t_{total}} \right) M_{T_{lower}} \right) \quad (7.1)$$

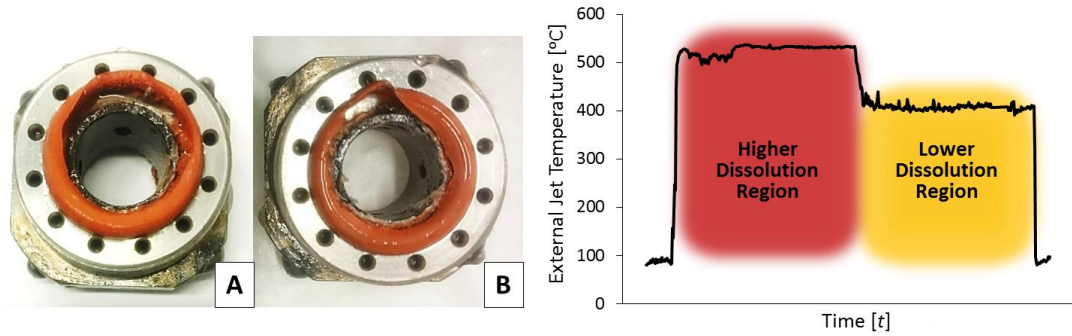


Figure 38. A) An extensively eroded O-ring that did not fail. **B)** A failed O-ring with a clear fluid channel. **C)** External jet thermocouple temperature profile from a failed O-ring CEHS experiment, showing both the high and low temperature regions.

The initial CEHS tests used the same experimental conditions as PWHS tests (24.5 ± 1 MPa, $400 \pm 15^\circ\text{C}$) except that all the initial CEHS tests were run for 10 minutes, the latter tests maintained the same pressure and time but dropped the jet temperature. Since the testing conditions for both sets of experiments were identical the assumption found in Chapter 5.2.1 for PWHS that erosion was not a significant factor in rock removal was also assumed for CEHS.

Experimental research by Urusova on the behavior of NaOH at high temperatures (350 - 550°C) and pressures (15-90 MPa) indicates that NaOH will separate into liquid and vapor phases at these extreme conditions (Urusova, 1974). This means that as the percentage of vaporized NaOH increases –the concentration of NaOH remaining in the liquid phase will also increase to a maximum (~77%). This increased concentration of liquid NaOH in a hydrothermal jet will induce more damage to the impinged rock face. This CEHS research is in the high temperature range of Urusova's work, but significantly below the pressures where this phenomena begins to occur. Additionally,

the low NaOH molality in the CEHS experiments reduces the chance of this phenomena occurring. Therefore, accelerated surface damage due to very high NaOH concentrations was not deemed crucial to predicting rock removal rates.

In his PhD research at MIT Worley examined the effect of pH and ionic strength on the quartz dissolution rate (Worley, 1994) (Worley, et al., 1996). The similarities between Worley's study of pure quartz and this study of Barre Granite (~27% quartz), combined with the use of NaOH solution at increasing temperatures in both sets of experiments, made direct experimental comparison possible. However, Worley's experiments covered a wide range of conditions so only the data that did not have additional, or different, acids, bases, or salts added, to modify or buffer the ionic strength or hydroxide concentration of the solution, were used in the comparison.

7.2. Experimental Results

7.2.1. Initial Experiments

For jet temperatures from 550°C to 575°C and NaOH concentrations from 0.074 to 1.38% w/w (0.0725-0.345 molality) mineral mass in the Barre Granite core sample was removed at appreciable rates as seen in Figure 39. Circular holes were produced into the rock of approximately equal diameter to the circular surface area exposed to the NaOH hydrothermal jet.

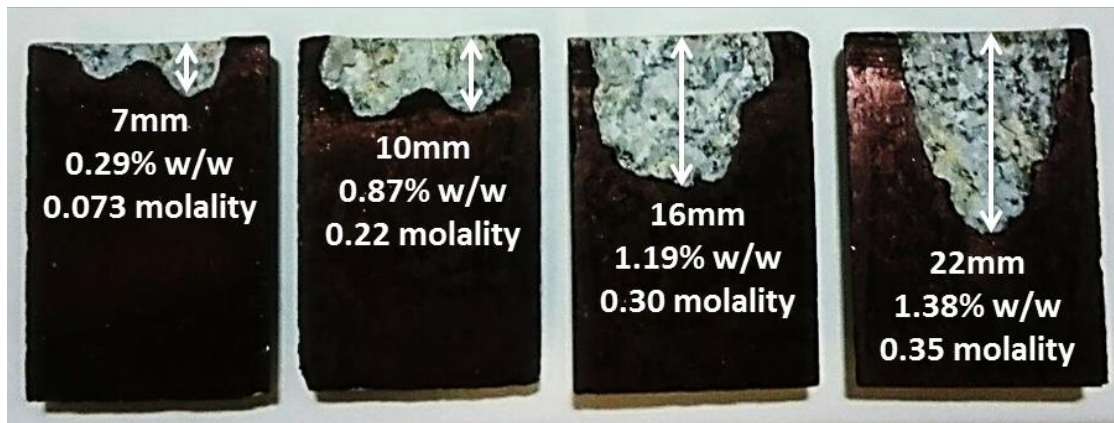


Figure 39. CEHS results. Side cut Barre Granite samples show significant dissolution and spallation. These experiments used 0.29-1.38% w/w NaOH (0.0725-0.345 molality), at 24.5 ± 1 MPa, $400 \pm 10^\circ\text{C}$ rock surface temperature, for 10 minutes.

The depth penetrated was dependant on the molality of NaOH, Figure 40. However, because both the water jet drilling nozzle and rock sample were stationary during the test only a portion of the rock sample was penetrated. The depth of the cavity and total mass of granite removed for a specific exposure time is approximately linearly proportional to increased solvent molality as can be seen in Figure 40.

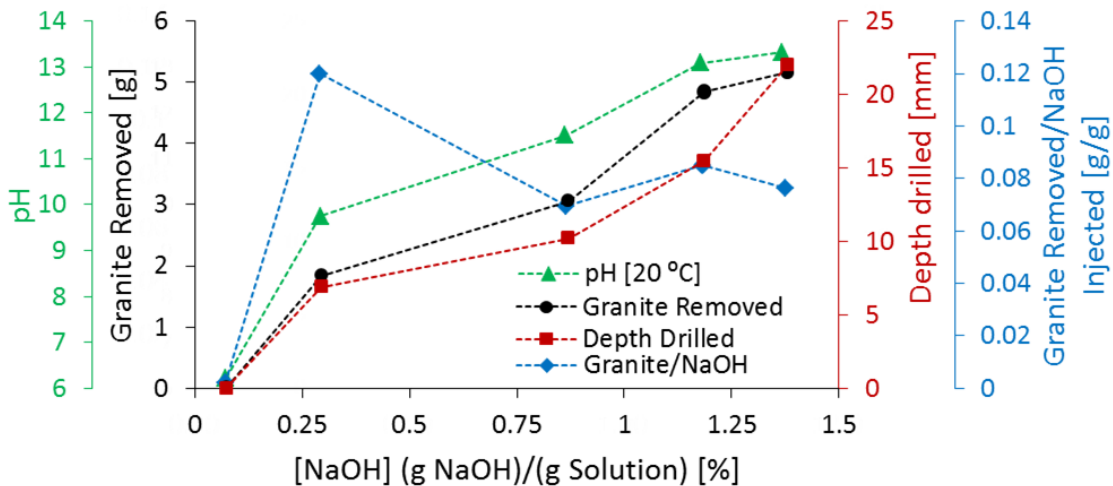


Figure 40. The mass of granite removed and the depth drilled increases with increasing NaOH molality. Once the process initiates the ratio of granite removed to NaOH injected stabilizes with increasing solvent molality. All experiments ran for 10 minutes. Data in Table 8, see Appendix B-2.

Chemical attack and/or dissolution was apparently a significant factor in granite removal because the fragments or spalls recovered were not the similarly sized disk shaped flakes (~3mm diameter) that are traditionally produced from thermal flame/hydrothermal spallation (Potter Drilling, 2008) (Potter, et al., 2010), but rather fragments ranging in size from ~1mm to 75µm (screen size) and rounded like small pebbles, Figure 41. Also the mass of spalls collected were only a fraction (<5%) of the total mass removed. In addition, a significant amount of very fine calcite powder precipitate was recovered from the filter and back-pressure valve. It is possible that some of the calcite recovered during CEHS precipitated from the cooling water due to secondary chemical reactions; however, no calcite deposition was observed during the PWHS tests. Clearly, increased solubility of silica at high pH is occurring but quantification was not possible as no measurements were made of SiO₂ concentration

in the diluted effluent water; however, future research will examine this to close the mass balance. The captured spalls were primarily quartz and mica, implying a more rapid removal of the feldspar mineral due to weakening of the rock matrix by a combination of dissolution and geochemical alteration. This was consistent with the post spallation images in Figure 42 that indicated preferential boundary weakening around quartz crystals due to the absence of feldspar.

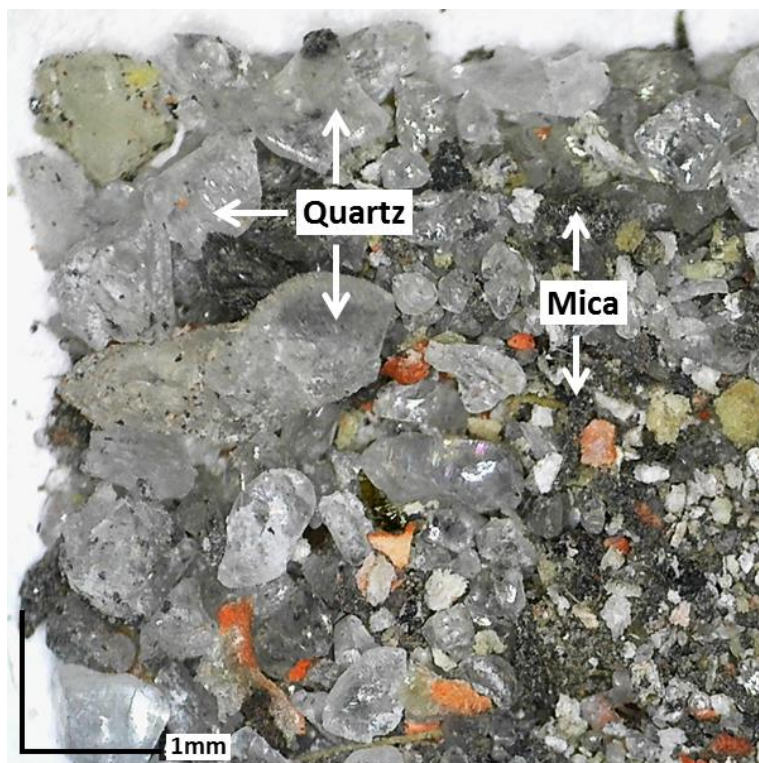


Figure 41. Predominantly pebble shaped quartz spalls ranging in size. The clear spalls are quartz, dark grey and black are micas, and red color is surface staining from the high temperature silicone O-ring. No feldspar is visible.

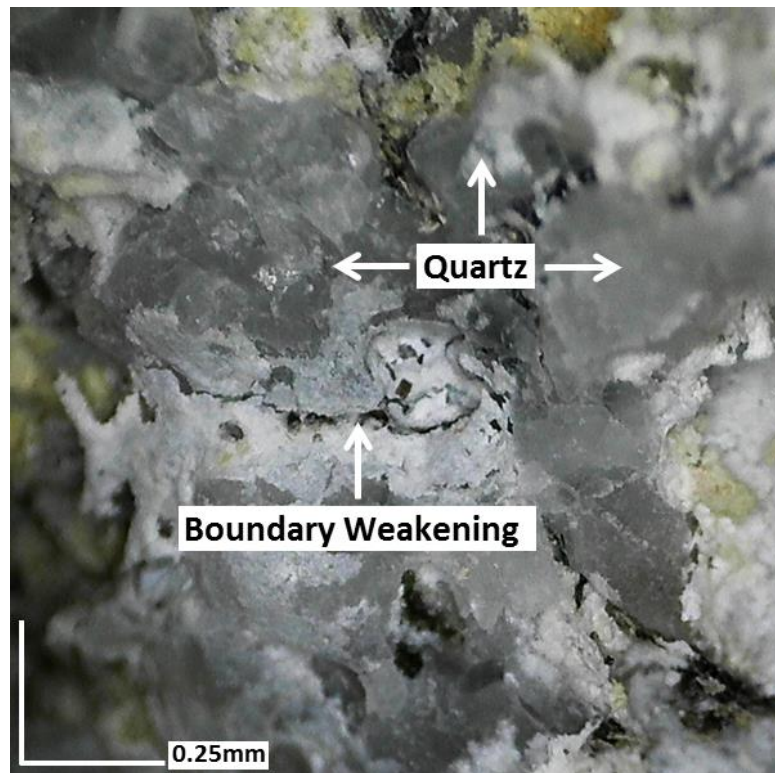


Figure 42. Preferential weakening along crystal boundaries due to the absence of feldspar.

There was also a small amount of redeposition of a white and yellowish mineral as can be seen in Figure 43; however, this mineral redeposition was heterogeneous and concentrated in particular locations. One possible explanation is the production of zeolites since the temperature of the hydrothermal jet was in the range of the paragenesis temperature for zeolites. SEM testing of mineral scrapings by x-ray revealed all the elemental components of zeolite which appears to validate this hypothesis, but further experimentation, beyond the scope of this thesis, is required to determine the precise crystal structure.

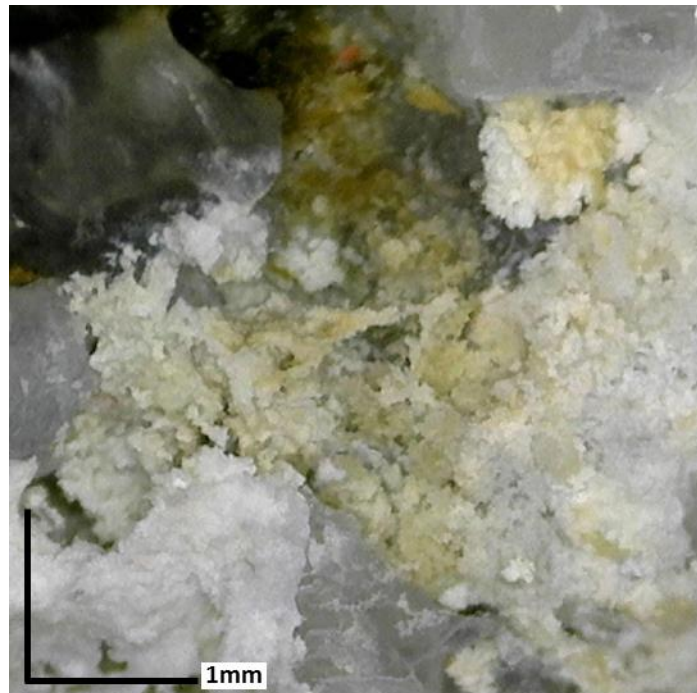


Figure 43. Reformed minerals on the side walls of the area hollowed out by CEHS.

7.2.2. Time Dependance

The relative mass of granite removed by a given amount of NaOH, for 10 min of exposure in the CEHS test, appears to stabilize and become linear after the onset of spallation despite the increased distance between the dissolving rock face and the jet nozzle, see Figure 40. This was a surprising result because as Figure 44 shows: increasing the stand off distance implies increased mixing of the fresh solution with the discharge, thereby reducing the amount of unsaturated fluid reaching the active surface (spallation front), and reducing the impinging solvent temperature.

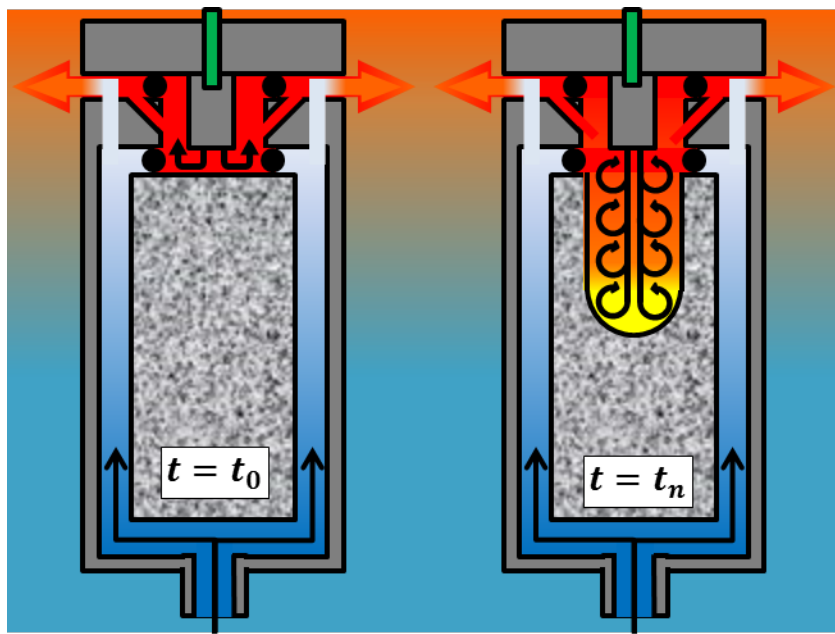


Figure 44. Increased mixing of fresh NaOH solution with the discharge fluid as the penetration depth increases with time.

CEHS experiments were run for shorter time lengths of 2 and 5 minutes to determine if the rock removal rate was initially faster due to the close proximity of the impinging jet to the rock surface. These shorter experiments were run at the same surface temperature and pressure ($400\pm15^\circ\text{C}$, 24.5 ± 1 MPa) as the full 10 minute tests.

The experimental results indicated that the mass of rock removed was linearly correlated to the time the Barre Granite sample was exposed to the CEHS jet. This suggests that the rate of mass transport is sufficient to result in a linear dissolution rate. Both to deliver NaOH and remove the dissolution products (SiO_2 and rock particles) where this linear rock removal rate is determined by the molality of the solvent, see Figure 45. In principle, there should be a maximum stand-off distance between the CEHS jet nozzle and rock face at which the linear drilling rate no longer

applies (due to decreased solvent temperature and chemical kinetics) but this limiting distance was not observed in our testing. Such insensitivity to stand-off distance could be particularly useful in actual drilling practice because it would provide a driller with a practical margin of error when setting a CEHS drilling head down hole.

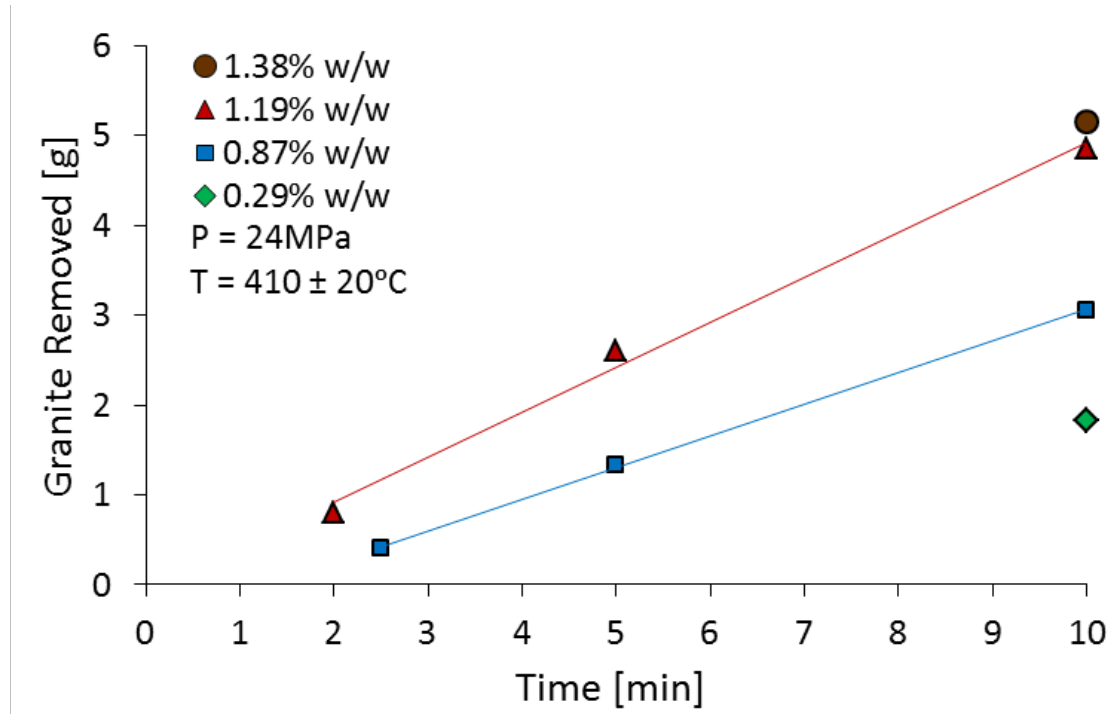


Figure 45. Granite removed during CEHS experiments for different exposure times indicate that rock removal is linear dependant on exposure time. Data in Table 8, see Appendix B-2.

7.3. Modelling Drilling Rate

Creating a predictive theoretical model for the exceedingly complex chemical kinetics that are involved in the enhanced hydroxide-ion dissolution of granite is beyond the scope of this thesis. The empirical model described below relies on correlating

measured dissolution rates to a global reaction rate expression using regression analysis.

The modelling of granite dissolution/erosion/spallation is a similar process to that of quartz dissolution. Because quartz is a significant component of Barre Granite, and feldspar contains silicates as well. Applying the analysis in Chapter 5.2.1 with regards to the mechanisms of rock removal using pure water allows us eliminate some of the basic factors of erosion from CEHS and primarily focus on the chemical processes that are driving dissolution/spallation. Therefore, regression analysis of the experimental data that accounts for the influence of temperature and NaOH concentrations is sufficient to quantify a *drilling rate*, $\left(\frac{dz}{dt}\right)$, that can act as a surrogate for the much more complex chemical and mechanical interactions occurring in CEHS.

The forward reaction rate of silica dissolution as described by Worley can be seen in Equation (5.1) (Worley, 1994). The reverse reaction rate, $r_{reverse}$ is

$$r_{reverse} = k_{reverse} \frac{A_{surface}}{M_{water}} m_{H_4SiO_4} \left[\frac{\text{mol}}{\text{kg} * \text{s}} \right] \quad (7.2)$$

Where M_{water} is the mass of water [kg], $A_{surface}$ active surface area [m^2], $k_{reverse}$ is the reverse reaction dissolution rate constant [$\text{mol}/(\text{m}^2\text{s})$], $m_{H_4SiO_4}$ is moles H_4SiO_4 / kg H_2O . H_4SiO_4 is the silicic acid formed by the dissolution of quartz. The net reaction rate is

$$\begin{aligned}
 r_{net} &= \frac{dm_{H_4SiO_4}}{dt} = r_{forward} - r_{reverse} \\
 &= \frac{A_{surface}}{M_{water}} (k_{forward} - k_{reverse} m_{H_4SiO_4}^{saturated}) \left[\frac{\text{mol}}{\text{kg} * \text{s}} \right]
 \end{aligned} \tag{7.3}$$

At equilibrium the forward and reverse rates are equal so Equation (7.3) can be rearranged using the principle of microscopic equilibrium that gives

$$\begin{aligned}
 r_{net}^{equilibrium} &= r_{forward} - r_{reverse} = 0 \\
 &= (k_{forward} - k_{reverse} m_{H_4SiO_4}^{saturated}) \left[\frac{\text{mol}}{\text{kg} * \text{s}} \right]
 \end{aligned} \tag{7.4}$$

and

$$k_{reverse} = \frac{k_{forward}}{m_{H_4SiO_4}^{saturated}} \tag{7.5}$$

Now substituting Equation (7.5) into Equation (7.3)

$$r_{net} = \frac{dm_{H_4SiO_4}}{dt} = k_{forward} \frac{A_{surface}}{M_{water}} \left(1 - \frac{m_{H_4SiO_4}}{m_{H_4SiO_4}^{saturated}} \right) \left[\frac{\text{mol}}{\text{kg} * \text{s}} \right] \tag{7.6}$$

The impinging convective fluid is a constantly-refreshed solvent containing no H₄SiO₄ therefore this concentration at the rock surface ($m_{H_4SiO_4}$) can be assumed to be negligible allowing us to ignore the reverse reaction rate, with this assumption Equation (7.6) can be rewritten as

$$r_{net} = r_{forward} = k_{forward} \frac{A_{surface}}{M_{water}} \left[\frac{mol}{kg * s} \right] \quad (7.7)$$

The analysis up to this point has been for the dissolution of quartz with pure water; however, this model is for NaOH enhanced dissolution of Barre Granite. Correcting for the difference in solute minerals –the left hand side of Equation (7.6) becomes

$r_{net} = \frac{dm_{rock}}{dt}$. Multiplying the molality term $\left(\frac{mol_{solute(rock)}}{M_{water}} \right)$ through by the molar mass of granite rock, and substituting M_{water} with $M_{solvent}$

$$r'_{net} = r'_{forward} = \frac{dm_{rock} \left(\frac{M_{rock}}{mol_{rock}} \right)}{dt} = \frac{d \left(\frac{M_{rock}}{M_{solvent}} \right)}{dt} \left[\frac{kg_{rock}}{kg_{solvent} * s} \right] \quad (7.8)$$

M_{rock} is the mass of granite rock [kg], $M_{solvent}$ is the mass of injected solvent, which is predominantly water with a NaOH concentration [kg]. Next, Equation (7.7) is multiplied by the molar mass of granite which means the units adjust to

$$r'_{net} = r'_{forward} = k_{forward} \frac{A_{surface}}{M_{solvent}} \left[\frac{kg_{rock}}{kg_{solvent} * s} \right] \quad (7.9)$$

$M_{solvent}$ is the mass of injected solvent which is water with a NaOH concentration [kg], $A_{surface}$ active surface area being dissolved [m^2], $k_{forward}$ is the dissolution rate constant [$kg_{solute}/(m^2 s)$].

Once the chemical reaction is progressing the operation can be considered to be in a quasi steady state. In the PWHS experiments we assumed $A_{surface}$ was constant, it is recognized that the dissolution area was increasing as the rock face that was being eroded became somewhat roughened and non-planar. None the less, most of the rock

removal was in the z-direction with a constant x,y area allowing us to use Equation (5.3). However, in CEHS we are removing a lot more rock so the area term, $A_{surface}$, is no longer approximately constant. Assuming CEHS drilling results in a cylindrical hole of constant diameter with a hemispherically shaped base –the change in exposed surface area depends on what is a function of time and depth, continuously increasing due to rock removal. For this case, the area can be rewritten as

$$A_{surface} = \frac{\pi D^2}{2} + \pi Dz(t) [m^2] \quad (7.10)$$

Where D (assumed to be a constant) is the diameter of the borehole, and $z(t)$ the increasing depth over time. The $z(t)$ term increases the complexity of the problem without adding information. However, $A_{surface}$ is the area of experimental interest, so once the solvent has interacted with the hemispherical dissolution front (base of the cylinder) the remaining chemical reactions with the borehole sidewall are of less consequence and of lower magnitude since the solvent has decreased in temperature and contains dissolved granite. Therefore, it is assumed that only the hemispherical spallation front advanced as drilling proceeded, see Figure 46. This $A_{surface} = \frac{\pi D^2}{2}$ assumption allows us to cancel out the portions of the area term that account for the side walls and rewrite the RHS of Equation (7.9) as

$$r'_{forward} = k_{forward} \frac{\frac{\pi D^2}{4}}{M_{solvent}} \left[\frac{kg_{rock}}{kg_{solvent} * s} \right] \quad (7.11)$$

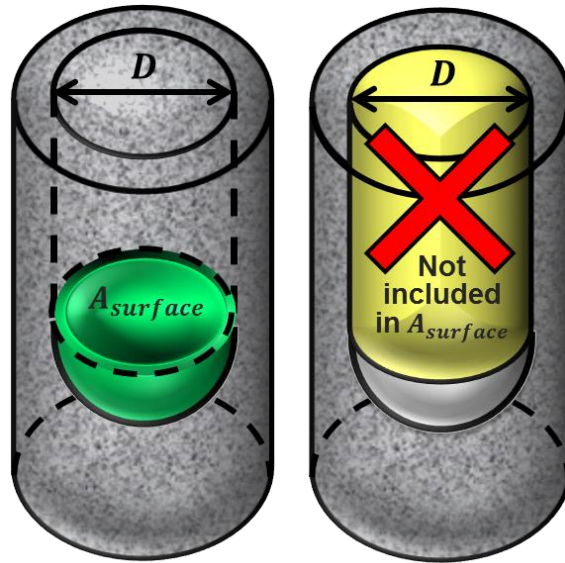


Figure 46. $A_{surface}$ is the hemispherical spallation front at the base of the borehole not including the cylindrical side wall.

Extending the cylindrical borehole assumption to the rock face it can be assumed that the implicit area of the granite rock face in Equation (7.8) is also a hemispherically shaped spallation front.

$$\begin{aligned}
 r'_{forward} &= \frac{d\left(\frac{M_{rock}}{M_{solvent}}\right)}{dt} = \left(\frac{1}{M_{solvent}}\right) \frac{dM_{rock}}{dt} \\
 &= \left(\frac{1}{M_{solvent}}\right) \frac{d\bar{V}_{rock} \rho_{rock}}{dt} = \left(\frac{A_{rock} \rho_{rock}}{M_{solvent}}\right) \frac{dz}{dt} \quad (7.12) \\
 &= \left(\frac{\pi D^2}{4 M_{solvent}} \rho_{rock}\right) \frac{dz}{dt} \left[\frac{kg_{rock}}{kg_{solvent} * s}\right]
 \end{aligned}$$

where ρ_{rock} is the density of Barre Granite ($\sim 2655 \text{ kg/m}^3$ (Sydney, 1966)). Combining Equations (7.11) and (7.12)

$$r'_{forward} = \left(\frac{\pi D^2}{\frac{4}{M_{solvent}} \rho_{rock}} \right) \frac{dz}{dt} = k_{forward} \frac{\pi D^2}{M_{solvent}} \left[\frac{k g_{rock}}{k g_{solvent} * s} \right] \quad (7.13)$$

simplification provides us with a “drilling rate” of

$$\frac{dz}{dt} = \frac{k_{forward}}{\rho_{rock}} \quad (7.14)$$

$k_{forward}$ can be written as

$$k_{forward} = \frac{M_{rock}}{\left(\frac{\pi D^2}{4}\right) t} \left[\frac{k g}{m^2 * s} \right] \quad (7.15)$$

based on experimental data for a specific mass of granite dissolved over a known exposure time and for a specific borehole diameter, D . Alternatively, the removal rate constant in basic solution can be represented with a simple global rate law of the form:

$$k_{forward} = k(T)_{OH^-, Na^+} m_{OH^-}^b m_{Na^+}^c \left[\frac{k g}{m^2 * s} \right] \quad (7.16)$$

Where $k(T)_{OH^-, Na^+}$ is an empirical rate constant that is a function of temperature, in Arrhenius form, $m_{OH^-}^b$ is the molality of OH^- , $m_{Na^+}^c$ the molality of Na^+ , and b and c are the reaction orders of OH^- and Na^+ respectively. However, since the experiments are injecting a known quantity of NaOH the OH^- and Na^+ concentrations do not vary relative to each other so the reaction orders can be combined and written as

$$b + c = b' \quad (7.17)$$

Since b , c and by result b' will be regression fitted parameters they can be real numbers and are not limited to integers representing the stoichiometries of the reactants. Combining Equations (7.16) and (7.17)

$$k_{forward} = k(T)_{OH^-} m_{OH^-}^{b'} \left[\frac{kg}{m^2 * s} \right] \quad (7.18)$$

Where $k(T)_{OH^-} = A \exp \left[\frac{-B}{RT} \right]$ and A, B are fitted constants based on the rate data as $f(T)$. The experimental data can then be plotted on $\log k_{forward}$ vs. $\log m_{OH^-}$ from which $k(T)_{OH^-}$ and b' can be extracted enabling the prediction of a drilling rate based on solvent temperature and concentration.

7.4. Determining Chemical Dissolution Constant

Twelve tests at three different rock surface temperatures ($\sim 370^\circ\text{C}$, $\sim 385^\circ\text{C}$, and 400°C) were combined with the original five CEHS tests (410°C) to determine $k_{forward}$. These twelve latter experiments were at temperatures in the near critical region to investigate any potential impacts on rock dissolution rates due to fluid phase or density change at different solvent molalities.

Examination of the experimental data indicated that the mass of granite removed at a particular solvent concentration increased with increasing temperature clearly indicating a strong temperature dependence consistent with Arrhenius behavior, see

Figure 47. To confirm this observation the CEHS data was plotted in Figure 48 as $\log k_{forward}$, $\log m_{OH^-}$ where b' is the slope of the trendline. The linear fit of the log CEHS data indicates a first order reaction, and the spacing between the lines a clear temperature dependance.

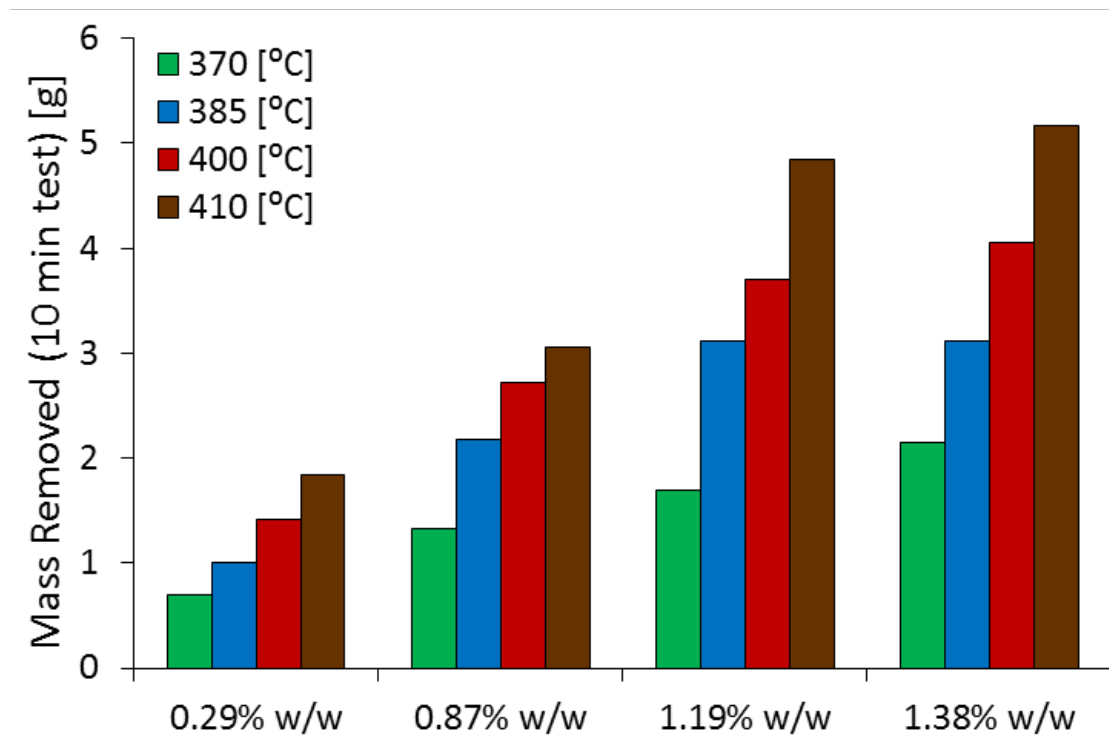


Figure 47. Increasing mass of rock removal at increasing molality, and temperature.

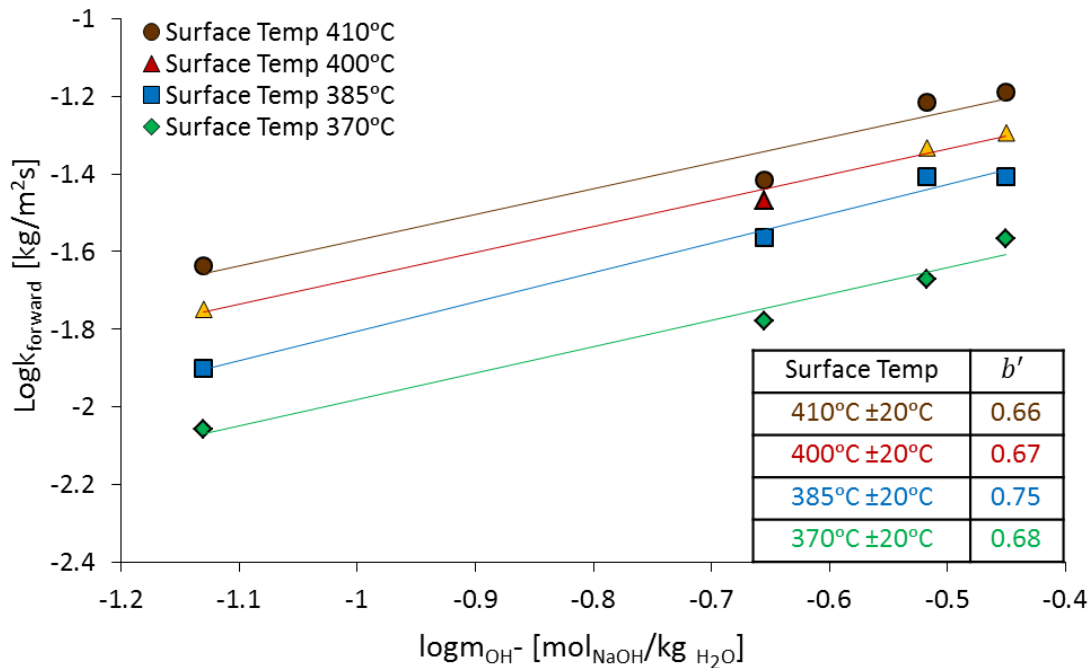


Figure 48. CEHS data plotted as $\log k_{forward}$, $\log m_{OH^-}$, and includes the b' found by regression analysis. The yellow data points are corrected data due to failed O-ring seals during the experiment.

The definitive confirmation of temperature dependence of the chemical dissolution data was embedded in $k(T)_{OH^-}$ term. By rearranging Equation (7.18) into $\log k(T)_{OH^-} = \log \frac{k_{forward}}{m_{OH^-}^{b'}}$ and graphing the results on an Arrhenius plot the linearity of the data shows the direct relationship between $k(T)_{OH^-}$ and temperature. Plotting $k(T)_{OH^-}$ in Figure 49 resulted in a reasonably close to linear fit, clearly demonstrating the temperature dependence of the CEHS process. The set of data (surface temperature ~385°C) with a b' slope and $k(T)_{OH^-}$ that were inconsistent with the rest of the data, were very close to the supercritical transition point of water (~382°C, 24.5 MPa), which may have affected the experimental results. Identifying the b' and $k(T)_{OH^-}$

terms in Figure 48 and Figure 49 enabled the quantification of $k_{forward}$ and thereby the overall drilling rate (Equation (7.14)) for this process.

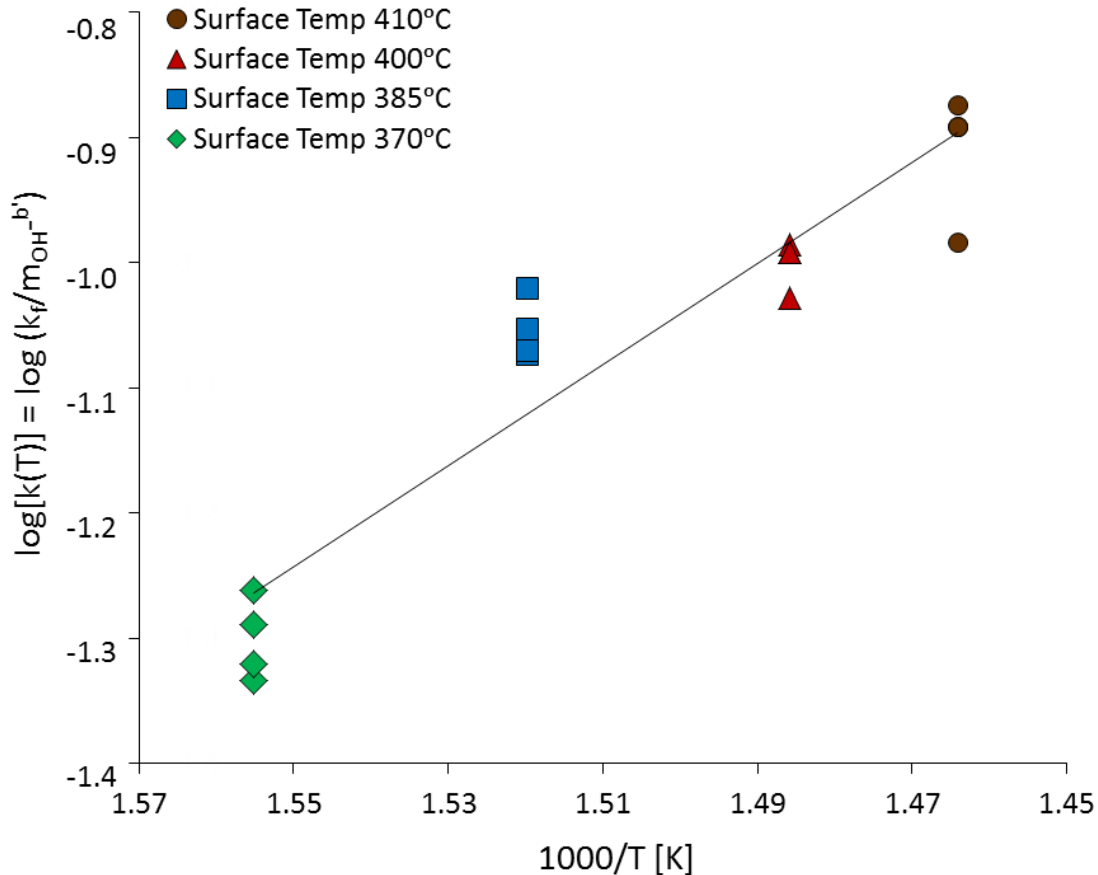


Figure 49. $k(T)_{OH^-}$ on an Arrhenius plot. The data with a surface temperature of $\sim 385^{\circ}\text{C}$ close to the water critical point transition of $\sim 382^{\circ}\text{C}$ (24.5 MPa) did not agree as well to a linear regression fit as those data farther away. Data in Table 10, see Appendix B-2.

Worley's quartz dissolution data in which he used NaOH solution as the solvent was compared to this research and there was good correlation, as can be seen in the slope, b' , of the regression trendlines in Figure 50 (Worley, et al., 1996). Worley's geometric surface area basis rather than BET surface area basis was used in the correlation

because the data translated well to this research and Worley stated “*geometric surface area basis was as good as (or better) than the BET surface area basis.*” It should be noted that Worley’s $\log k_{forward}$ had units of mol/m²s, this was converted to kg/m²s by multiplying through the the molar mass of SiO₂ ($60.0843 \times 10^{-3} [\frac{kg}{mol}]$). The units of Worley’s data rather than this study were adjusted because his experiments used pure quartz with a known molar mass rather than heterogeneous Barrie Granite which may introduce error, because its molar mass is based on an empirical average.

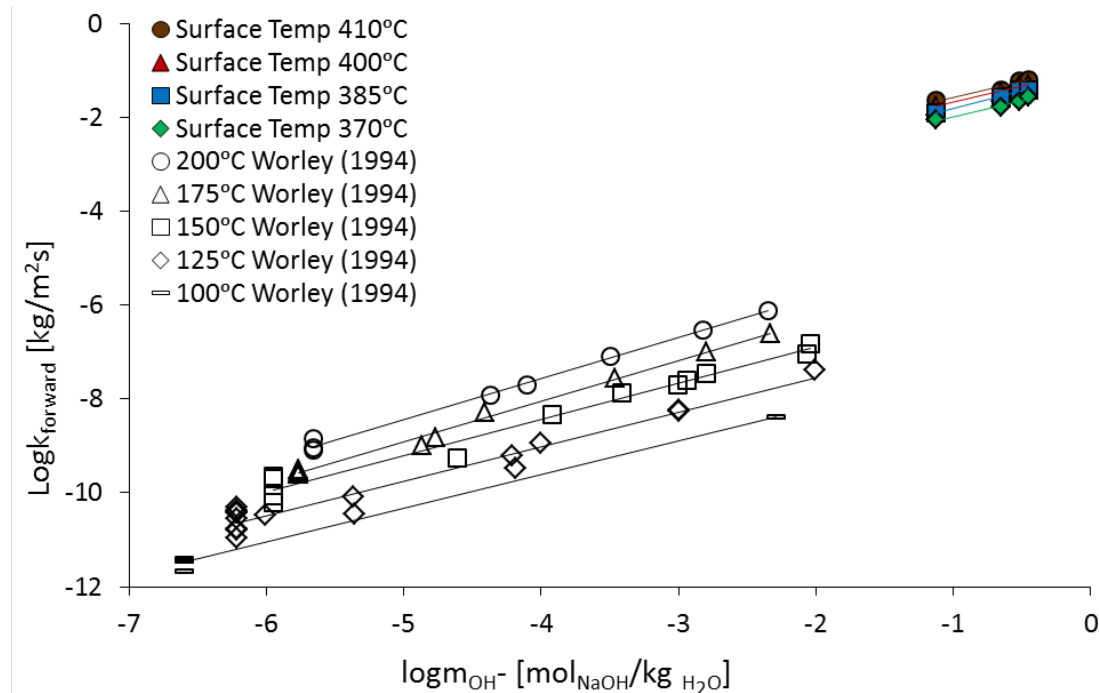


Figure 50. Regression analysis of this study and Worley’s NaOH dissolution of quartz data. The yellow data points are corrected data due to failed O-ring seals during the experiment. Data in Table 10, see Appendix B-2.

The comparison of CEHS to Worley’s data was extended to the $k(T)_{OH^-}$ temperature dependence term. The result was completely consistent with the Worley, et al (1996)

correlation of quartz dissolution in OH⁻ solution at lower temperatures, even though Worley used pure quartz and this study dissolved Barre Granite. Figure 51 shows that the linear slopes of the regression analysis for both this study and Worley's work were coincident with the overall slope of the regression analysis on the combined data. Indicating that even though the percentage of SiO₂ dissolved by NaOH solution differed between quartz and Barre Granite, the temperature dependence of the process was consistent over six orders of magnitude.

Adding CEHS into the overall comparison of spallation methods in Figure 52 indicates that the heat flux and surface temperature values were not significantly higher for CEHS than PWHS. Therefore, thermal spallation itself was not solely responsible for rock removal since the empirically determined minimums for the onset of continuous thermal spallation in low density gas jets were not reached. Figure 51 provides a direct comparison between previous lower temperature NaOH dissolution of quartz and this study, indicating that chemical dissolution due to excess hydroxides is the dominant mechanism of rock removal. Thermal stress induced by the high thermal gradient in the rock should not be ignored as a significant mechanism for weakening the rock matrix, but its effect is likely to be secondary in comparison to the rapid dissolution kinetics at the hydrothermal temperatures we are using.

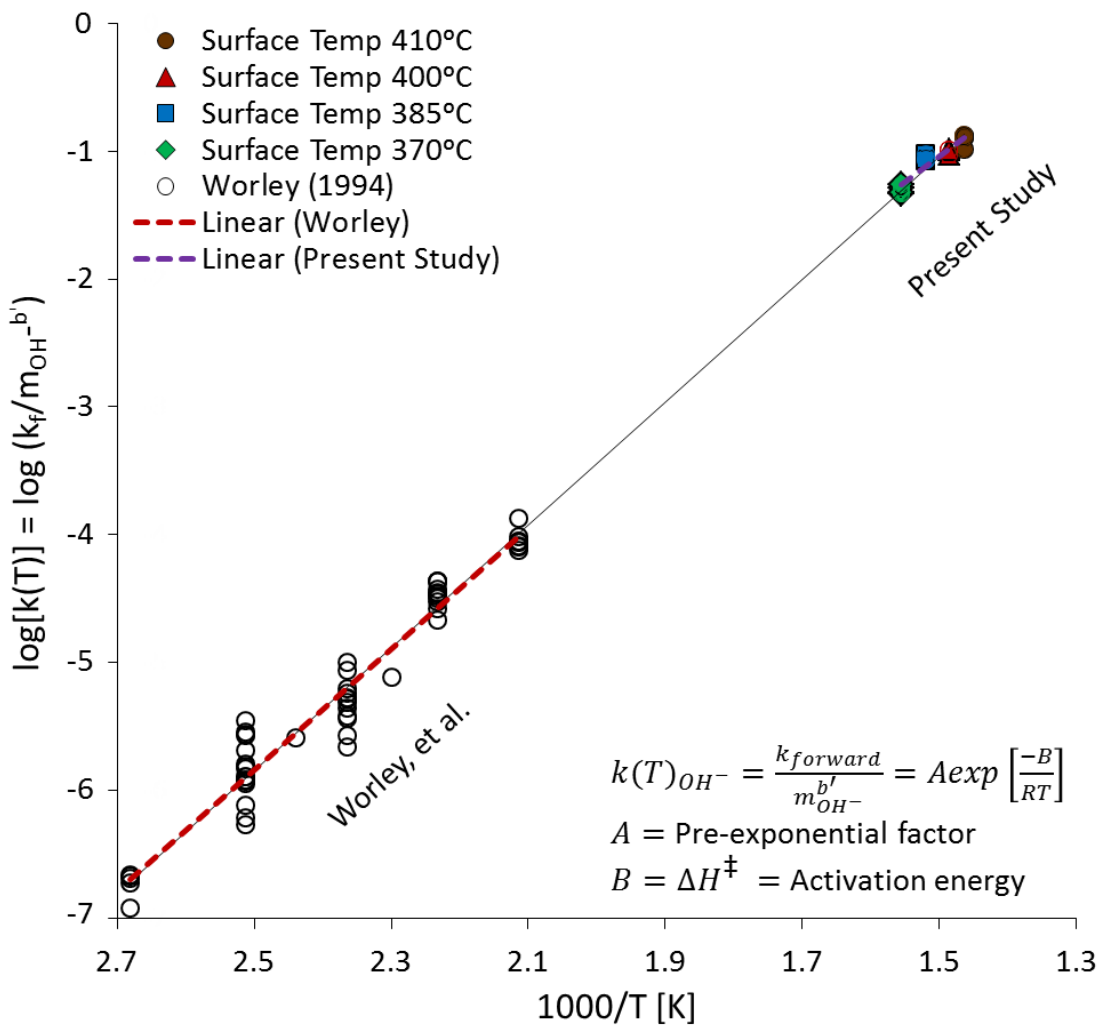


Figure 51. $k(T)_{OH^-}$ on an Arrhenius plot. Linearity of the trendline illustrates temperature dependence of chemical dissolution over six orders of magnitude.

Data in Table 10, see Appendix B-2.

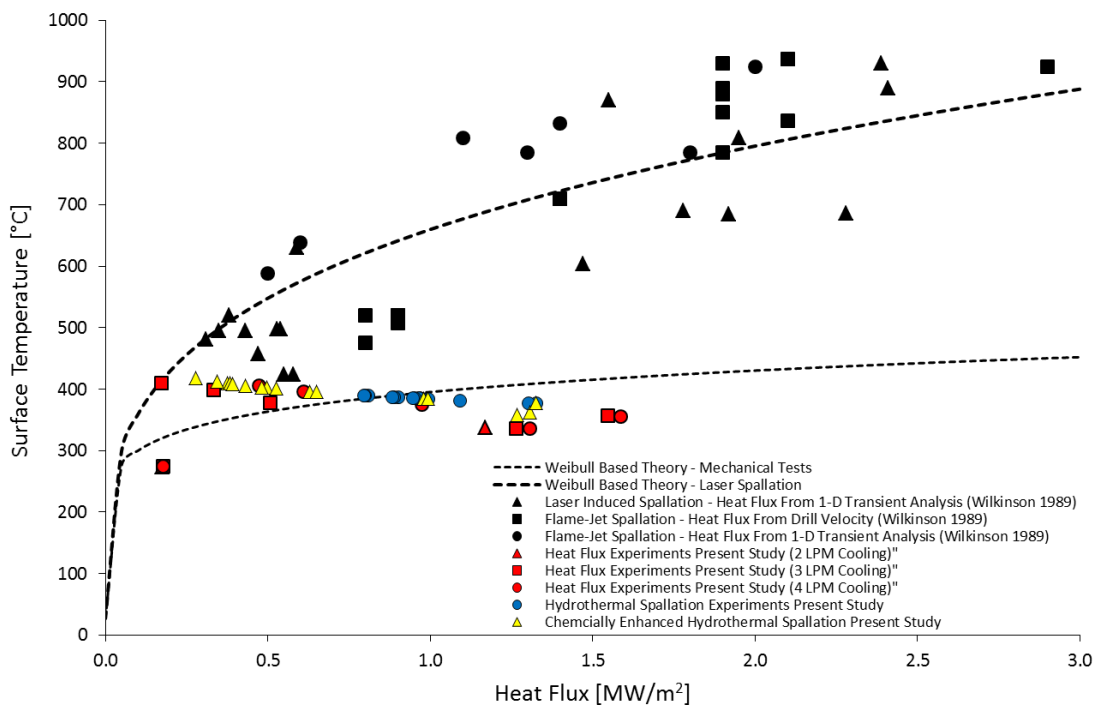


Figure 52. Comparison of CEHS to flame, laser, and PWHS drilling.

Although spallation clearly occurred given the quartz and mica spalls recovered, see Figure 41, it was not due to thermal effects alone. As the mass of spalls compared to the overall mass of rock removed implies that the spalls were either crystals dislodged from the rock matrix, due to the complete dissolution of the surrounding supporting grains or, as their rounded shape suggests, caused by the weakening of the rock matrix due to the partial dissolution of quartz in the inter-granular regions. It seems likely that the chemically enhanced spallation we observed is some combination of both processes.

Chapter 8. CONCLUSIONS AND RECOMMENDATIONS

8.1. Conclusion

Hydrothermal jet spallation experiments were conducted at Cornell University's Energy Institute. An electrically heated pure water jet was impinged at supercritical temperatures (535-575°C) and pressures (22.5-28MPa) on Barre Granite samples to simulate deep wellbore drilling conditions in basement rock. The hydrothermal jet preferentially removed quartz crystals from the granite samples. At the range of temperatures examined the amount of quartz removed was an order of magnitude greater than could be explained by quartz dissolution alone. Rock surface temperature measurements indicated that the Barre Branite sample was always cooler than the jet (410°C surface temperature, which is ~150°C less than the 560 °C jet temperature), and that the temperature difference between the rock surface and hydrothermal jet increased non-linearly as the system temperature increased. The maximum heat flux occurred near the critical point of pure water. Comparison of the hydrothermal spallation data to spallation using low density gas flames and laser heating indicated that rock temperatures and heat flux were just below the empirically determined minimums required for continuous thermal spallation. Therefore, the amount of quartz removed was either due to increased rates of quartz dissolution in an unsaturated pure water stream (unlikely due to SiO₂ kinetics), or preferential micro-spallation (non-continuous) of the quartz due to intra/inter-granular weakening by partial dissolution and differences in thermal expansion properties of the constituent minerals.

Sodium hydroxide was introduced into the hydrothermal jet to determine if increased rates of chemical dissolution would accelerate weakening of the rock matrix and induce higher rock removal rates. The NaOH solution significantly increased the rates of rock removal for concentrations ranging from 0.29-1.38% w/w (0.0725-0.345 molality), drilling roughly circular holes in the Barre Granite core samples. The mass of rock removed and the depth of hole was directly correlated to the molality of the solvent, resulting in an empirical expression consistent with measurement of enhanced quartz dissolution caused by increased OH⁻ concentrations. Quartz and mica spalls were recovered, and preferential grain boundary weakening due to the absence of feldspar was observed. Small amounts of localized mineral redeposition were found inside the drilled holes, preliminary scanning electron microscopy testing indicated that the mineral composition corresponds to zeolites. A model of the theoretical drilling rate implies that the rate of rock removal primarily relies on the chemical dissolution rate constant, which contained an Arrhenius dependence on jet temperature and power law dependence on sodium hydroxide molality. Accumulated rates for chemically enhanced hydrothermal spallation corresponded closely to previous chemical dissolution measurements made by Worley (1996). In addition, high rates of rock removal were observed below the empirically determined minimums for continuous thermal spallation obtained with low density flames and laser heating. In summary, the rate of CEHS rock removal is proportional to the temperature and concentration of NaOH solution impinging on the Barre Granite.

8.2. Future Work

Further experimental work to estimate hydrothermal spallation's convective heat transfer coefficient is needed to quantify the mechanisms controlling the surface heat flux needed to induce spallation. These estimates could be achieved by combining both the surface temperature and heat flux measurements into one experiment in which a thermocouple is placed in a small chamber bored out beneath the heat flux experiment set up as shown in Figure 53. The experimental data could be further described and validated using finite element modelling of heat transfer at the sample's surface where the hydrothermal jet impinges on the rock surface in conjunction with modelling heat transfer throughout the sample. This work would provide a more robust analytical model for estimating the temperature difference between the impinging jet and rock surface.

Achieving continuous PWHS may be possible by adding external radial and axial stress and strain to the current sample during testing. This could be achieved by sleeving the 1" diameter Barre Granite core sample and then applying, either uniform or differential, triaxial mechanical or hydrostatic pressure. Another way to increase the confining stress would be enlarging the experimental rock sample size from a 1" diameter cylinder to 3-4" diameter sample. Adding external confining stress (axial and radial) to the larger rock sample would increase the probability of spallation, and would most accurately replicate downhole conditions.

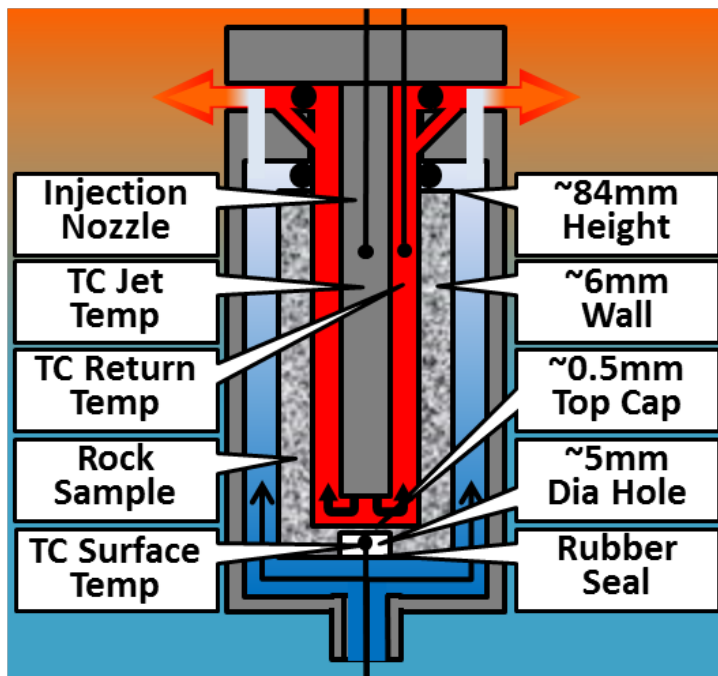


Figure 53. Combined heat flux and surface temperature experimental configuration, designed to directly compare heat flux to rock surface temperature and estimate the average heat transfer coefficient.

Further CEHS experimental work could investigate other chemicals to induce spallation such as Na_2CO_3 , $\text{Ca}(\text{OH})_2$, and KOH . Additional work in understanding the thermal/chemical dissolution process of granite through analysis and experimentation could provide unique insights into previously unexplored aspects of chemical drilling. A complete investigation of the paragenesis of the spallation reaction products may lead to a greater understanding of the chemical dissolution process of Barre Granite, providing the information needed to improve and optimize the CEHS drilling process.

APPENDIX A

Appendix A-1 Instrument Error Analysis

A summary of the uncertainty associated with the data from the hydrothermal spallation tests can be seen in Figure 15. The Moffat method was used for calculating uncertainty (Moffat, 1985). Inputs to the energy calculation relied on both temperature and pressure data so the uncertainty was checked against both values. Plotting temperature on the independent axis resulted in slightly higher uncertainly values than pressure, so temperature was used in the final comparison.

The system considered in this analysis was the pressure vessel and internal reactor unit. The base equation used was the first law of thermodynamics

$$\dot{Q}_{in} - \dot{Q}_{out} + \dot{W}_{in} - \dot{W}_{out} + \sum \dot{m}(h + ke + pe)_{in} - \sum \dot{m}(h + ke + pe)_{out} = 0 \quad (\text{A.1})$$

The assumptions made in this uncertainty analysis were:

1. Steady flow, quasi-equilibrium
2. Adiabatic $\dot{Q}_{in} = \dot{Q}_{out} \approx 0$
3. Kinetic and Potential energy neglected $ke = pe \approx 0$
4. No heat generation in the reactor $\dot{W}_{in} = \dot{W}_{out} \approx 0$
5. Pressure is constant throughout the system. Therefore the properties of state are calculated for an isobaric system.

6. Enthalpy (h) is a function of temperature and pressure $h = f(T, P) \rightarrow C_p \Delta T$ since pressure is approximately constant.
7. Density (ρ) is a function of temperature and pressure $\rho = f(T, P)$. The overall functions for finding ρ are most likely not linear, but in between the empirical data points (used to create the function) linearity is assumed.
8. Temperature is in units of Kelvin, pressure in bar, and flow rate m^3/sec

With these assumptions Equation (A.1) becomes

$$\begin{aligned} \sum \dot{m}(h)_{in} - \sum \dot{m}(h)_{out} &= 0 \\ \rightarrow (\dot{m}h)_{hot\ in} + (\dot{m}h)_{cold\ in} - (\dot{m}h)_{out} &= 0 \end{aligned} \quad (\text{A.2})$$

Additionally

$$\dot{m}_{hot\ in} + \dot{m}_{cold\ in} = \dot{m}_{out} \quad (\text{A.3})$$

Which implies

$$(\dot{m}h)_{hot\ in} + (\dot{m}h)_{cold\ in} - (\dot{m}_{hot\ in} + \dot{m}_{cold\ in})h_{out} = 0 \quad (\text{A.4})$$

Enthalpy is a function of temperature and pressure

$$h = f(T, P) \quad (\text{A.5})$$

However, due to the isobaric assumption specific heat capacity, C_p , can be used. C_p is also a function of temperature and pressure, but its error is quantified by NIST. Since

the enthalpy is simply integration of the area under the C_p curve the error associated with h and C_p can be considered the same.

$$h = C_p(T) = f_{C_p}(T, P)T \quad (\text{A.6})$$

\dot{m} is flow rate, Q , multiplied by density; therefore

$$\dot{m} = f_\rho(T, P)Q \quad (\text{A.7})$$

Combining Equations (A.3) - (A.7)

$$\begin{aligned} & \left[f_\rho(T, P)Q f_{C_p}(T, P)T \right]_{\text{hot in}} + \left[f_\rho(T, P)Q f_{C_p}(T, P)T \right]_{\text{cold in}} \\ & - \left[(f_\rho(T, P)Q_{\text{hot in}} \right. \\ & \left. + f_\rho(T, P)Q_{\text{cold in}}) f_{C_p}(T, P)T \right]_{\text{out}} = 0 \end{aligned} \quad (\text{A.8})$$

Equation (A.8) highlights that the uncertainty associated with h and \dot{m} is based on temperature, pressure, and flow rate. However, since h , \dot{m} , T , P and *rate* are knowns we can write Equation (A.8) in terms of some constant D, where D represents the uncertainty of the calculation.

$$\begin{aligned} D = & [Q \rho h]_{\text{hot in}} + [Q \rho h]_{\text{cold in}} \\ & - [(Q \rho)_{\text{hot in}} + (Q \rho)_{\text{cold in}}]h_{\text{out}} \end{aligned} \quad (\text{A.9})$$

Calculating the propagation of uncertainty D associated with the measurements

$$D = \sqrt{\left[\left(\frac{\partial D}{\partial \rho} \delta \rho \right)^2 + \left(\frac{\partial D}{\partial Q} \delta Q \right)^2 + \left(\frac{\partial D}{\partial h} \delta h \right)^2 \right]_{hot\ in} + \left[\left(\frac{\partial D}{\partial \rho} \delta \rho \right)^2 + \left(\frac{\partial D}{\partial Q} \delta Q \right)^2 + \left(\frac{\partial D}{\partial h} \delta h \right)^2 \right]_{cold\ in} + \left[\left(\frac{\partial D}{\partial \rho} \delta \rho \right)_{cold\ in}^2 + \left(\frac{\partial D}{\partial Q} \delta Q \right)_{cold\ in}^2 + \left(\frac{\partial D}{\partial h} \delta h \right)^2 \right]_{+ \left[\left(\frac{\partial D}{\partial \rho} \delta \rho \right)_{hot\ in}^2 + \left(\frac{\partial D}{\partial Q} \delta Q \right)_{hot\ in}^2 + \left(\frac{\partial D}{\partial h} \delta h \right)^2 \right]_{out} + 2(\delta P)^2} } \quad (A.10)$$

Finding the partial derivatives

$$\frac{\partial D}{\partial \rho} = \left(\frac{\partial}{\partial \rho} (\rho Q h) \right) = Q h \quad (A.11)$$

$$\frac{\partial D}{\partial Q} = \left(\frac{\partial}{\partial Q} (\rho Q h) \right) = \rho h \quad (A.12)$$

$$\frac{\partial D}{\partial h} = \left(\frac{\partial}{\partial h} (\rho Q h) \right) = \rho Q \quad (A.13)$$

Inserting Equations (A.11), (A.12), & (A.13) into Equation (A.10)

$$D = \sqrt{\left[(Q h \delta \rho)^2 + (\rho h \delta Q)^2 + (\rho Q \delta h)^2 \right]_{hot\ in} + \left[(Q h \delta \rho)^2 + (\rho h \delta Q)^2 + (\rho Q \delta h)^2 \right]_{cold\ in} + \left[([Q \delta \rho]_{cold\ in} h)^2 + ([\rho \delta Q]_{cold\ in} h)^2 + ([\rho Q]_{cold\ in} \delta h)^2 \right]_{+ \left[([Q \delta \rho]_{hot\ in} h)^2 + ([\rho \delta Q]_{hot\ in} h)^2 + ([\rho Q]_{hot\ in} \delta h)^2 \right]_{out} + (\delta P)^2 + (\delta T)^2} } \quad (A.14)$$

Yields the overall uncertainty associated with the experimental measurements. Where the uncertainly δ associated with the primary parameters can be found in Table 2:

Table 2. Uncertainty, δ , associated with the measurements and equation of state properties.

δC_p	NIST states: “ <i>The uncertainty in isobaric heat capacity is 0.2% in the vapor and 0.1% in the liquid, with increasing values in the critical region and at high pressures.</i> ”
δh	$\pm 0.2\%$
δP	$\pm 0.11\% FS$
$\delta Q_{cold\ in}$	$\pm 0.5\%$
$\delta Q_{hot\ in}$	$\pm 2.0\%$
δT	$\pm 0.75\% \text{ or } 2.2K$
$\delta \rho$	NIST states: “ <i>The uncertainties (in density) rise at higher temperatures and/or pressures, but are generally less than 0.1% in density except at extreme conditions.</i> ”

Full quote from NIST regarding the known errors associated with the properties of state is:

“*The uncertainty in density of the equation of state is 0.0001% at 1 atm in the liquid phase, and 0.001% at other liquid states at pressures up to 10 MPa and temperatures to 423 K. In the vapor phase, the uncertainty is 0.05% or less. The uncertainties rise at higher temperatures and/or pressures, but are generally less than 0.1% in density except at extreme conditions. The uncertainty in pressure in the critical region is 0.1%. The uncertainty of the speed of sound is 0.15% in the vapor and 0.1% or less in the liquid, and increases near the critical region and at high temperatures and pressures. The uncertainty in isobaric heat capacity is 0.2% in the vapor and 0.1% in the liquid, with increasing values in the critical region and at high pressures. The uncertainties of saturation conditions are 0.025% in vapor pressure, 0.0025% in saturated liquid density, and 0.1% in saturated vapor density. The uncertainties in the saturated densities increase substantially as the critical region is approached.*” (NIST, 2017).

Appendix A-2 External Jet Temperature Correlation

The thermocouple mounted on the outside of the hydrothermal jet nozzle measured lower temperatures than the internally mounted thermocouple, necessitating a correlation between the externally mounted thermocouple jet temperature and the rock surface temperature. A full description of this change in thermocouple location can be found in Chapter 7.1, and the correlation is below in Figure 54.

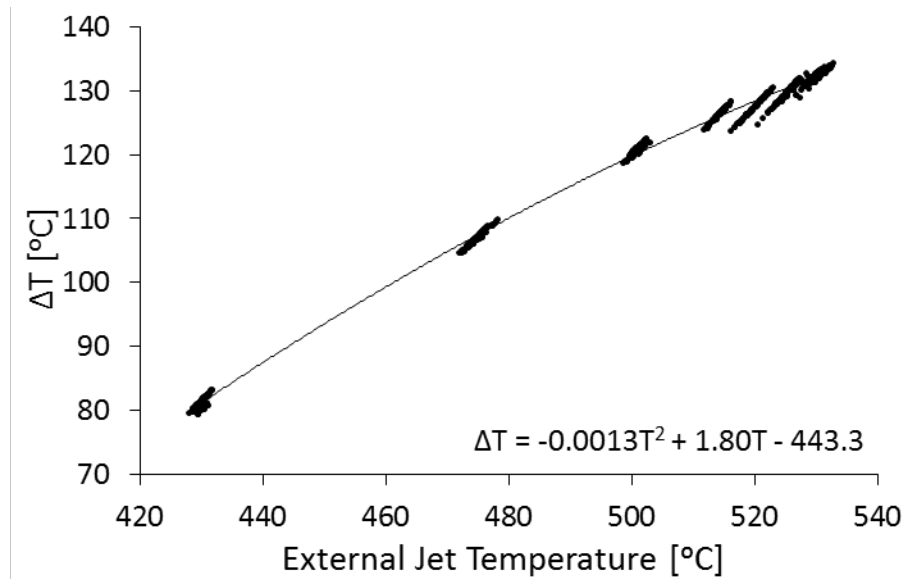


Figure 54. Temperature difference correlation between the externally mounted thermocouple and rock surface temperature.

APPENDIX B

Appendix B-1 Pure Water Spallation Test Data

Table 3. Pure water hydrothermal spallation data from Figure 17.

Jet Temperature [°C]	Surface Temperature* [°C]	Pressure [Mpa]	Time [min]
535.0	377.6	23.0	10 min
536.0	378.1	22.7	30 min
545.0	382.4	23.0	24 min
550.0	384.7	25.5	10 min
551.0	385.2	23.0	17 min
551.3	385.3	26.5	10 sec
551.5	385.4	25.6	10 min
552.3	385.8	26.6	1 min
552.5	385.9	26.8	3 min
555.2	387.2	25.6	30 min
555.9	387.5	25.1	30 min
556.3	387.7	25.3	10 min
561.0	389.8	25.4	3 min
561.7	390.2	24.9	10 sec
562.0	390.3	25.7	1 min

*Calculated using empirical ΔT correlation from Chapter 5.2.3.1.

Table 4. Chemical dissolution of quartz in pure water data from Figure 24.

Jet Temperature [°C]	Dissolution Rate Constant [mol/m ² s]	Researcher/s
23	4.07E-14	Worley
23	4.27E-14	
50	6.17E-13	
50	6.31E-13	
50	6.61E-13	
70	4.68E-12	
100	6.46E-11	
100	6.03E-11	
100	6.31E-11	
100	3.55E-11	
125	4.79E-10	
125	6.31E-10	
125	8.32E-10	
125	6.76E-10	
125	6.46E-10	
125	2.82E-10	
125	1.78E-10	
125	2.63E-10	
125	1.51E-10	
125	2.57E-10	
150	3.31E-09	
150	3.80E-09	
150	1.02E-09	
150	1.45E-09	
150	1.00E-09	
175	4.17E-09	
175	4.57E-09	
175	4.17E-09	
175	5.25E-09	
175	4.79E-09	
200	1.32E-08	

Table 4 continued.

Jet Temperature	Dissolution Rate Constant	Researcher/s
[°C]	[mol/m ² s]	
400	3.55E-05	Kitahara
400	4.47E-05	
440	6.92E-05	
440	4.47E-05	
440	3.09E-05	
480	3.89E-05	
480	6.46E-05	
70	6.92E-13	van Lier et al.
80	3.47E-12	
90	6.92E-12	
248	8.32E-07	Siebert et al.
250	1.05E-06	
269	1.45E-06	
291	2.82E-06	
315	6.03E-06	
332	9.55E-06	
400	1.12E-04	Weill & Fyfe
625	1.07E-03	
105	5.37E-11	Rimstidt & Barnes
145	4.37E-09	
170	3.72E-09	
265	2.75E-07	
305	7.24E-07	
200	8.91E-08	Robinson
200	6.17E-08	
200	5.01E-08	
250	2.14E-07	
184	1.10E-08	
184	7.94E-09	
184.5	4.79E-09	
202	4.90E-08	
202.5	3.24E-08	
203	5.13E-08	
215	8.91E-08	
221	1.29E-07	
221	1.10E-07	

Table 4 continued.

Jet Temperature [°C]	Dissolution Rate Constant [mol/m ² s]	Researcher/s
221	7.59E-08	Robinson cont'd
253	4.17E-07	
255	3.16E-07	
80	1.78E-11	
80	1.29E-11	Blum et al.
80	1.02E-11	
200	2.34E-08	
200	4.47E-08	Dove & Crerar
200	5.25E-08	
200	4.17E-08	
200	5.50E-08	
201	3.72E-08	
250	1.82E-07	
300	1.07E-06	
300	9.77E-07	
300	7.08E-07	
40	7.41E-13	Bennett
50	1.86E-12	
60	4.68E-12	
70	1.48E-11	
70	1.17E-11	
200	1.45E-07	Berger et al.
300	4.17E-06	
300	2.34E-06	
550	2.29E-03	Present Study
536	2.33E-03	
550	6.62E-03	
550	2.08E-02	

Table 5. Pure water hydrothermal spallation rock surface and jet temperature data from Figure 26.

Jet Temperature [°C]	Surface Temperature [°C]	ΔT [°C]
88.8	68.8	20.0
237.3	178.5	58.8
266.2	211.9	54.3
302.0	233.3	68.7
302.0	239.3	62.7
357.8	283.8	74.0
381.2	301.6	79.7
468.0	342.2	125.9
521.8	367.4	154.4
559.1	388.6	170.5

Table 6. Pure water heat flux data from Figure 29.

1.8 LPM Cooling Water Flow Rate ($15 \pm 5^{\circ}\text{C}$)			
Jet Temperature [°C]	Surface Temperature [°C]	Surface Temperature +20°C [°C]	Heat flux [MW/m ²]
298.7	273	293	0.169
396.8	337	357	1.133
2.8 LPM Cooling Water Flow Rate ($15 \pm 5^{\circ}\text{C}$)			
300.0	274	294	0.173
395.4	336	356	1.226
431.2	357	377	1.499
469.2	377	397	0.491
510.5	398	418	0.323
535.5	410	430	0.167
3.8 LPM Cooling Water Flow Rate ($15 \pm 5^{\circ}\text{C}$)			
301.2	275	295	0.172
395.4	336	356	1.267
428.0	355	375	1.538
464.3	375	395	0.944
504.6	395	415	0.591
525.7	405	425	0.459

Table 7. Mechanical, flame, laser, pure water hydrothermal spallation data comparison from Figure 32.

Surface Temperature [°C]	Heat Flux [MW/m ²]	Researcher/s
481	0.31	Wilkinson (1989) Laser Spallation
495	0.35	
520	0.38	
495	0.43	
457	0.47	
497	0.53	
497	0.54	
423	0.55	
423	0.58	
630	0.59	
604	1.47	
870	1.55	
690	1.78	
685	1.92	
808	1.95	
686	2.28	
930	2.39	
890	2.41	
785	1.80	Wilkinson (1989) Flame Spallation Transient Analysis
925	2.00	
785	1.30	
808	1.10	
832	1.40	
638	0.60	
588	0.50	
925	2.90	Wilkinson (1989) Flame Spallation Drill Velocity
937	2.10	
937	2.10	
837	2.10	
879	1.90	
850	1.90	
890	1.90	
785	1.90	

Table 7 continued.

Surface Temperature [°C]	Heat Flux [MW/m ²]	Researcher/s
710	1.40	Wilkinson (1989) Flame Spallation Drill Velocity
710	1.40	
520	0.90	
520	0.90	
508	0.90	
520	0.90	
475	0.80	
520	0.80	
273	0.17	Present Study 1.8 LPM Cooling,
337	1.13	
274	0.17	Present Study 2.8 LPM Cooling
336	1.23	
357	1.50	
377	0.49	
398	0.32	
410	0.17	
275	0.17	Present Study 3.8 LPM Cooling,
336	1.27	
355	1.54	
375	0.94	
395	0.59	
405	0.46	
378	1.33	Present Study Hydrothermal Spallation Experiments
378	1.30	
382	1.09	
385	0.99	
385	0.97	
385	0.97	
386	0.95	
386	0.95	
387	0.90	
387	0.89	
388	0.88	
390	0.81	
390	0.80	
390	0.79	

Appendix B-2 Chemical Enhanced Hydrothermal Spallation Test Data

Table 8. Rock removal and time dependence data from Figure 45.

NaOH	Time	Mass Removed
[% w/w]	[min]	[g]
0.29	10	1.84
0.87	2.5	0.40
0.87	5	1.33
0.87	10	3.06
1.19	2	0.80
1.19	5	2.61
1.19	10	4.85
1.38	10	5.16

Table 9. CEHS rock removal, penetration depth, and pH data for 10 minute tests from Figure 40, and Figure 48.

Surface Temperature [°C]	Mass NaOH/ Mass Solution [% w/w]	NaOH Injection Rate [g/min]	Granite Dissolved [g]	Depth Drilled [mm]	pH [20 °C] [pH]
410	0.074	0.35	0.00697	0.0	6.22
410	0.29	1.4	1.836	6.9	9.75
410	0.87	4.1	3.056	10.2	11.51
410	1.19	5.7	4.849	15.5	13.09
410	1.38	6.6	5.162	22.0	13.32
400	0.29	1.4	1.421 *	-	-
400	0.87	4.1	2.717	-	-
400	1.19	5.7	3.701 *	-	-
400	1.38	6.6	4.050 *	-	-
385	0.29	1.4	1.001	-	-
385	0.87	4.1	2.174	-	-
385	1.19	5.7	3.114	-	-
385	1.38	6.6	3.115	-	-
370	0.29	1.4	0.697	-	-
370	0.87	4.1	1.323	-	-
370	1.19	5.7	1.694	-	-
370	1.38	6.6	2.155	-	-

* Value has been adjusted using Equation (7.1)

Table 10. Complete chemical dissolution data table from Figure 50, and Figure 51.

$\log m_{OH^-}$ [mol _{NaOH} /kg _{H2O}]	$\log k_f$ [kg/m ² s]	$\log k(T)_{OH^-}$	Researcher/s
-6.60	-11.41	-6.66	100°C Worley
-6.60	-11.44	-6.69	
-6.60	-11.42	-6.67	
-6.60	-11.67	-6.92	
-2.29	-8.37	-6.72	
-6.22	-10.54	-5.69	
-6.22	-10.42	-5.57	
-6.22	-10.30	-5.45	
-6.22	-10.39	-5.54	
-6.22	-10.41	-5.56	
-6.22	-10.77	-5.92	125°C Worley
-6.22	-10.97	-6.12	
-6.22	-10.80	-5.95	
-4.00	-8.95	-5.83	
-6.01	-10.48	-5.79	
-4.21	-9.21	-5.93	
-5.37	-10.08	-5.89	
-4.19	-9.48	-6.21	
-5.36	-10.45	-6.27	
-3.00	-8.23	-5.89	
-3.00	-8.26	-5.92	137°C Worley
-2.01	-7.38	-5.81	
-2.27	-7.36	-5.59	
-5.95	-9.70	-5.06	
-5.95	-9.64	-5.00	
-5.95	-10.21	-5.57	
-5.95	-10.06	-5.42	
-4.61	-9.25	-5.66	
-3.92	-8.34	-5.28	
-2.94	-7.60	-5.31	
-2.80	-7.46	-5.28	150°C Worley
-2.04	-6.83	-5.24	
-3.41	-7.86	-5.20	
-3.01	-7.70	-5.35	
-2.07	-7.05	-5.44	

Table 10 continued.

$\log m_{\text{OH}^-}$	$\log k_f$	$\log k(T)_{\text{OH}^-}$	Researcher/s
[mol _{NaOH} /kg _{H2O}]	[kg/m ² s]		
-2.29	-6.90	-5.12	162°C Worley
-5.77	-9.60	-4.47	
-5.77	-9.56	-4.43	
-5.77	-9.60	-4.47	
-5.77	-9.50	-4.37	
-5.77	-9.50	-4.37	
-5.77	-9.59	-4.46	
-4.87	-9.00	-4.67	
-3.46	-7.56	-4.48	
-2.80	-6.99	-4.50	
-4.77	-8.82	-4.58	175°C Worley
-4.41	-8.29	-4.37	
-2.33	-6.60	-4.53	
-5.66	-9.10	-4.12	
-5.66	-9.04	-4.06	
-5.66	-8.85	-3.87	
-3.50	-7.09	-4.01	200°C Worley
-4.10	-7.70	-4.09	
-2.82	-6.53	-4.05	
-4.37	-7.93	-4.09	
-2.35	-6.12	-4.05	
-1.13	-2.06	-1.29	
-0.66	-1.78	-1.33	
-0.52	-1.67	-1.32	370°C
-0.45	-1.57	-1.26	
-1.13	-1.90	-1.05	
-0.66	-1.56	-1.07	
-0.52	-1.41	-1.02	385°C
-0.45	-1.41	-1.07	
-1.13	-1.75	-0.99	
-0.66	-1.47	-1.03	
-0.52	-1.33	-0.99	400°C
-0.45	-1.29	-0.99	
-1.13	-1.64	-0.89	
-0.66	-1.42	-0.98	
-0.52	-1.22	-0.87	410°C
-0.45	-1.19	-0.89	

REFERENCES

Augustine, C. R., 2009. *Hydrothermal Spallation Drilling and Advanced Energy Conversion Technologies for Engineered Geothermal Systems. Doctoral Thesis.* Massachusetts: Massachusetts Institute of Technology.

Benett, P. C., 1991. Quartz dissolution in organic-rich aqueous systems. *Geochimica et Cosmochimica Acta*, Volume 55, pp. 1781-1797.

Berger, G., Cadore, E., Schott, J. & Dove, P. M., 1994. Dissolution rate of quartz in lead and sodium electrolyte solutions between 25 and 300°C: Effect of the nature of surface complexes and reaction affinity. *Geochimica et Cosmochimica Acta*, 58(2), pp. 541-551.

Blackwell, D. et al., 2011. *Temperature-At-Depth Maps For the Conterminous US and Geothermal Resource Estimates.* Davis, Geothermal Resources Council, p. Vol 35 (GRC 1029452).

Blum, A. E., Yund, A. R. & Lasaga, A. C., 1990. The effect of dislocation density on the dissolution rate of quartz. *Geochimica et Cosmochimica Acta*, Volume 54, pp. 283-297.

Browning, J., 1981. *Flame-Jet Drilling in Conway, N.H. Granite*, Work Order #4-L10-2889R-1: University of California.

Calaman, J. J., Higginbotham, B. M., Mitchell, W. J. & Smith, G. H., 1954. *Thermal mineral piercing method and apparatus.* United States of America, Patent No. US 2675994 A.

Chang, C. T., Kojasoy, T. G. & Landis, F., 1995. Confined single- and multiple-jet impingement heat transfer I. Turbulent submerged liquid jets. *International Journal Heat Mass Transfer*, 38(5), pp. 833-842.

Chayes, F., 1950. *On a distinction between late-magmatic and post-magmatic replacement reactions*, Montpelier: Vermont Agency of Natural Resources.

Dickens, C. J. H., 1850. *The Personal History, Adventures, Experience and Observation of David Copperfield the Younger of Blunderstone Rookery.* First ed. London: Bradbury and Evans.

DOE, 2018. *U.S. Department of Energy Geothermal Heat Pumps.* [Online] Available at: <http://energy.gov/energysaver/geothermal-heat-pumps> [Accessed 27 Mar 2018].

References

- Dove, P. M. & Crerar, D. A., 1990. Kinetics of quartz dissolution in electrolyte solutions using a hydrothermal mixed flow reactor. *Geochimica et Cosmochimica Acta*, Volume 54, pp. 955-969.
- EPA, 2017. *Emissions & Generation Resource Integrated Database (eGRID) 2014*. [Online] Available at: <https://www.epa.gov/energy/emissions-generation-resource-integrated-database-egrid>
- Finger, J. & Blankenship, D., 2010. *Handbook of Best Drilling Practices for Geothermal Drilling*, Albuquerque: Sandia National Laboratories.
- Freudenrich, C. C. & Strickland, J., 2001. *How Oil Drilling Works*. [Online] Available at: <https://science.howstuffworks.com/environmental/energy/oil-drilling4.htm> [Accessed 2 April 2018].
- Fridleifsson, I. et al., 2008. *The possible role and contribution of geothermal energy to the mitigation of climate change*. Luebeck, Germany, IPCC, pp. 59-80.
- Garimella, S. V. & Rice, R. A., 1995. Confined and Submerged Liquid Jet Impingement Heat Transfer. *Journal of Heat Transfer*, Volume 117, pp. 871-877.
- Harmon, K., 2009. *Scientific American, How Does Geothermal Drilling Trigger Earthquakes?*. [Online] Available at: <http://www.scientificamerican.com/article/geothermal-drilling-earthquakes/> [Accessed 27 March 2018].
- Hawkins, A. J., Fox, D., Becker, M. & Tester, J. W., 2016. *Meso-Scale Field Testing of Reactive Tracers in a Model Geothermal Reservoir*. Stanford, 41st Stanford Geothermal Workshop.
- Hibbler, R. C., 2016. *Mechanics of Materials*. ISBN-13: 978-0134319650 Tenth ed. Singapore:Pearson.
- Hillson, S. D. & Tester, J. W., 2015. *Heat Transfer Properties and Dissolution Behavior of Barre Granite as Applied to Hydrothermal Drilling with Chemical Enhancement*. Stanford, 40th Stanford Geothermal Workshop.
- Holm, A., Jennejohn, D. & Blodgett, L., 2012. *Geothermal Energy and Greenhouse Gas Emissions*. [Online] Available at: http://geo-energy.org/reports/GeothermalGreenhouseEmissionsNov2012GEA_web.pdf [Accessed 27 March 2018].

References

- Hueze, F., 1983. High-Temperature Mechanical, Physical and Thermal Properties of Granitic Rocks --A Review. *International Journal of Rock Mechanics and Mining Sciences & Geomechanics Abstracts*, 20(1), pp. 3-10.
- Iceland's National Energy Authority, 2018. *Direct use of geothermal resources*. [Online] Available at: <http://www.nea.is/geothermal/direct-utilization/> [Accessed 1 March 2018].
- Kant, M. A. & Rudolf von Rohr, P., 2016. Minimal required boundary conditions for the thermal spallation process of granitic rocks. *International Journal of Rock Mechanics & Mining Sciences*, Volume 84, pp. 177-186.
- Keranen, K. M. et al., 2014. Sharp increase in central Oklahoma seismicity since 2008 induced by massive wastewater injection. *Science*, 345(6195), pp. 448-451.
- Kithara, S., 1960. The solubility equilibrium and the rate of solution of quarts in water at high temperatures and high pressures. *The Review of Physical Chemistry of Japan*, 30(2), pp. 122-130.
- Lazenby, J. R., 1978. *Hannibal's War, A Military History of the Second Punic War*. Paperback ed. Warminster:University of Oklahoma Press.
- Ledgerwood, L. W. J., 1960. Efforts to Develop Improved Oilwell Drilling Methods. *Journal of Petroleum Technology*, 219(April 1), pp. 61-74.
- Livy, T. L., ~27 BC. The History of Rome, Book 21. In: *English Translation 1912.2 . Rev. Canon Roberts*. New York: New York. E. P. Dutton and Co, p. Section 37.
- Lukawski, M. Z. et al., 2014. Cost analysis of oil, gas, and geothermal well drilling. *Journal of Petroleum Science and Engineering*, Volume 118, pp. 1-14.
- Lytle, D. & Webb, B. W., 1994. Air Jet Impingement Heat Transfer at Low Nozzle-Plate Spacings. *International Journal Heat Mass Transfer*, Volume 37, pp. 1687-1697.
- Macini, P. & Mesini, E., 1994. *Rock-Bit wear in ultra-hot holes*. delft, Proc. Int. Conf. "Eurock'94", pp. 223-230.
- Martin, H., 1977. Heat and Mass Transfer between Impinging Gas Jets and Solid Surfaces. *Advances In Heat Transfer*, Volume 13, pp. 1-60.

References

- Maurer, W. C., 1968. *Novel Drilling Techniques*. Houston: Pergamon Press.
- Maurer, W. C., 1980. *Advanced Drilling Techniques*. Tulsa: The Petroleum Publishing Company.
- Moffat, R. J., 1985. Using Uncertainty Analysis in the Planning of and Experiment. *Journal of Fluids Engineering*, June, Volume 107, pp. 173-178.
- Mohanty, A. K. & Tawfek, A. A., 1993. Heat Transfer Due to a Round Jet Impinging Normal to a Flat Surface. *International Journal Heat Mass Transfer*, Volume 36, pp. 1639-1647.
- Morrow, A. & Keenan, G., 2017. *Ontario to spend 7 billion in sweeping climate change plan*. [Online] Available at: <https://www.theglobeandmail.com/news/national/ontario-to-spend-7-billion-in-sweeping-climate-change-plan/article30029081/> [Accessed 27 March 2018].
- NIST REFPROP, 2013. *NIST Standard Reference Database 23, Version 9.1*. s.l.:NIST for the U.S. Secretary of Commerce on the behalf of the United States of America.
- NIST, 2017. *Isothermal Properties for Water*. [Online] Available at: http://webbook.nist.gov/cgi/fluid.cgi?T=800&PLow=&PHigh=&PInc=&Applet=on&Digits=5&ID=C7732185&Action=Load&Type=IsoTherm&TUnit=K&PUnit=MPa&DUnit=mol%2F1&HUnit=kJ%2Fmol&WUnit=m%2Fs&VisUnit=uPa*s&STUnit=N%2Fm&RefState=DEF#Important [Accessed 3 March 2018].
- North, J., Knibb, S. & Farouq Ali, S. M., 2001. The Hydratherm Hybrid Drilling Systems for Cheaper Heavy Oil Recovery. *Journal of Canadian Petroleum Technology*, 40(5), pp. 67-74.
- Norton, F. H., 1925. A General Theory of Spalling. *Journal of American Ceramic Society*, pp. Vol. 8, PP.29-39.
- NRC, 2017. *Heating Energy Cost Comparison: Heat Pump and Electric Heating Systems*. [Online] Available at: <http://www.nrcan.gc.ca/energy/publications/efficiency/heating-heat-pump/6835#table2> [Accessed 27 Mar 2018].
- Polizzotti, R. S., 2004. United States, Patent No. 6742603 B2.
- Potter Drilling, 2008. *Stage I Report. Laboratory testing and modeling of hydrothermal spallation drilling*, San Francisco: Potter Drilling.

References

- Potter, J. M., Potter, R. M. & Wideman, T. W., 2010. *Laboratory Study and Field Demonstration of Hydrothermal Spallation Drilling*. Davis, Geothermal Research Council Transactions, Vol. 34, pp 228-231.
- Potter, R. M. & Tester, J. W., 1998. *Continuous drilling of vertical boreholes by thermal processes: including rock spallation and fusion*. United States of America, Patent No. US 5771984 A.
- Preston, F., 1932. Theory of Spalling. *Journal of American Ceramic Society*, pp. 131-133.
- Rae, P., Di Lullo Arias, G. F. & Portman, L. N., 2004. *Chemically Enhanced Drilling Methods*. United States, Patent No. 6,772,847 B2.
- Rauenzahn, R. M. & Tester, J. W., 1985. *FlameJet Induced Thermal Spallation as a Method of Rapid Drilling and Cavity Formation*. Las Vegas, Society of Petroleum Engineers.
- Rauenzahn, R. M. & Tester, J. W., 1989. Rock Failure Mechanisms of flame-jet thermal spallation drilling - theory and experimental testing. *International Journal of Rock Mechanics and Mining Sciences & Geomechanics Abstracts*, 26(No. 5), pp. 381-399.
- Rauenzhan, R. M., 1986. *Analysis of Rock Mechanics and Gas Dynamics of Flame-Jet Thermal Spallation Drilling. Doctoral Thesis*. Cambridge: Massachusetts Institute of Technology.
- Rea, W. C., 1938. *Method of and apparatus for quarrying and shaping rock and stone*. United States of America, Patent No. US 2111872 A.
- Rice, R. A. & Garimella, S. V., 1994. *Heat Transfer From Discrete Heat Sources Using an Axisymmetric, Submerged and Confined Liquid Jet*. Brighton, United Kingdom, 10th International Heat Transfer Conference, Vol. 3, pp. 89-94.
- Rimstidt, J. D. & Barnes, H. L., 1980. The kinetics of silica-water reactions. *Geochimica et Cosmochimica Acta*, 44(11), pp. 1683-1699.
- Robertson, E. C., 1988. *Thermal properties of rocks*, Reston: United States Department Of The Interior Geological Survey.
- Robinson, B. A., 1982. *Quartz Dissolution and Silica Deposition in Hot Dry Rock Geothermal Systems, M.S. Thesis*. Cambridge: Massachusetts Institute of Technology.

References

- Roche, H. L., 1996. *Wandegkühlter Hydrothermal-Brenner (WHB) für die überkritische Nassoxidation*. Doctoral Thesis. Zurich: ETH Zurich.
- Rothenfluh, T., 2013. *Heat transfer phenomena of supercritical water jets in hydrothermal spallation drilling*, Doctoral Thesis. Zurich: ETH Zurich.
- Rothenfluh, T., Schuler, M. J. & Rudolf von Rohr, P., 2013. Experimental heat transfer study on impinging, turbulent, near-critical water jets confined by an annular wall. *The Journal of Supercritical Fluids*, Volume 77, pp. 79-90.
- Schilling, W. & Franck, E. U., 1988. Combustion and Diffusion Flames at High-Pressures to 2000 Bar. *Berichte Der Bunsen-Gesellschaft-Physical Chemistry Chemical Physics*, 92(5), pp. 631-636.
- Seibert, H., Youdelis, W. V., Leja, J. & Lilge, E. O., 1963. The kinetics of the dissolution of crystalline quartz in water at high temperatures and pressures. *Unit Processes in Hydrometallurgy*, Volume 24, pp. 284-299.
- Smith, G. H. & Mitchell, W. J., 1954. *Method and apparatus for thermally working minerals and mineral-like materials*. United States of America, Patent No. US 2675993 A.
- Stoces, B., 1927. Anwendung der Feuermethode im Modernen Bergbau (The Application of the Firing Method in Modern Mining). *Akademisch-Polytechnische Buchhandlung*, p. 350.
- Summers, D. A., 1972. *Water jet cutting related to jet and rock properties*. University Park, Pennsylvania, American Rock Mechanics Association.
- Superior Drilling Products, 2014. *U.S. Securities and Exchange Commission*. [Online] Available at: https://www.sec.gov/Archives/edgar/data/1600422/000114420414029260/v377937_s1a.htm [Accessed 27 March 2018].
- Sydney, P. C., 1966. *Handbook of Physical Constants*. Revised Edition ed. New York: The Geological Society of America, Inc..
- Tester, J. W. et al., 2006. *The Future of Geothermal Energy: Impact of enhanced geothermal systems (EGS) on the United States in the 21st century*, Cambridge: Massachusetts Institute of Technology and Department of Energy Report, Idaho National Laboratory, INL/EXT-06-11746.

References

- Tester, J. W. et al., 2012. *Sustainable Energy, Choosing Among Options*. Second ed. Cambridge: The MIT Press.
- Turcotte, D. L. & Schubert, G., 2002. *Geodynamics*. Second Edition ed. Cambridge: Cambridge University Press.
- Urusova, M., 1974. Phase Equilibria in the Sodium Hydroxide-Water and Sodium Chloride-Water Systems at 350-550°C. *Russian Journal of Inorganic Chemistry*, Volume 19, pp. 826-833.
- VAN Lier, J. A., DE Bruyn, P. L. & Overbeek, J. T. G., 1960. The solubility of quartz. *The Journal of Physical Chemistry*, Volume 64, pp. 1675-1682.
- Weill, D. F. & Fyfe, W. S., 1964. The solubility of quartz in H₂O in the range of 1000-4000 bars and 400-550°C. *Geochimica et Cosmochimica Acta*, Volume 28, pp. 1243-1255.
- White, F. M., 2011. *Fluid Mechanics, 7th Edition*. New York, NY: McGraw-Hill Companies Inc..
- Wilkinson, M. A., 1989. *Computational Modeling of the gas-phase transport phenomena and experimental investigation of surface temperature during flame-jet thermal spallation drilling, Doctoral Thesis*. Cambridge: Massachusetts Institute of Technology.
- Wilkinson, M. A. & Tester, J. W., 1993. Experimental Measurement of Surface Temperatures During Flame-Jet Induced Thermal Spallation. *Rock Mechanics and Rock Engineering*, 26(1), pp. 29-62.
- Williams, R. E., 1986. The thermal spallation drilling process. *Geothermics*, 15(No.1), pp. 17-22.
- Williams, R. E. et al., 1988. *Advancements in Thermal Spallation Drilling Technology*, Los Alamos: Los Alamos National Laboratory.
- Worley, W. G., 1994. *Dissolution kinetics and mechanisms in quartz and granite water systems, Doctoral Thesis*. Cambridge: Massachusetts Institute of Technology.
- Worley, W. G., Tester, J. W. & Grigsby, C. O., 1996. Quartz Dissolution Kinetics from 100-200°C as a Function of pH and Ionic Strength. *AIChE Journal*, 42(12), pp. 3442-3457.